ANALYSIS AND DESIGN OF A TEST APPARATUS FOR RESOLVING NEAR-FIELD EFFECTS ASSOCIATED WITH USING A COARSE SUN SENSOR AS PART OF A 6-DOF SOLUTION

A Thesis

by

DEVIN ALDIN STANCLIFFE

Submitted to the Office of Graduate Studies of
Texas A&M University
in partial fulfillment of the requirements for the degree of

MASTER OF SCIENCE

August 2010

Major Subject: Aerospace Engineering

Analysis and Design of a Test Apparatus for Resolving Near-field Effects Associated With Using a Coarse Sun Sensor as Part of a 6-DOF Solution

ANALYSIS AND DESIGN OF A TEST APPARATUS FOR RESOLVING NEAR-FIELD EFFECTS ASSOCIATED WITH USING A COARSE SUN SENSOR AS PART OF A 6-DOF SOLUTION

A Thesis

by

DEVIN ALDIN STANCLIFFE

Submitted to the Office of Graduate Studies of
Texas A&M University
in partial fulfillment of the requirements for the degree of

MASTER OF SCIENCE

Approved by:

Chair of Committee,	Helen L. Reed
Committee Members,	John E. Hurtado
	Alan Palazzolo
Head of Department,	Dimitris Lagoudas

August 2010

Major Subject: Aerospace Engineering

ABSTRACT

Analysis and Design of a Test Apparatus for Resolving Near-field Effects Associated With Using a Coarse Sun Sensor as Part of a 6-DOF Solution. (August 2010)

Devin Aldin Stancliffe, B.S., Texas A&M University;

B.S., Brigham Young University

Chair of Advisory Committee: Dr. Helen L. Reed

Though the Aerospace industry is moving towards small satellites and smaller sensor technologies, sensors used for close-proximity operations are generally cost (and often size and power) prohibitive for University-class satellites. Given the need for low-cost, low-mass solutions for close-proximity relative navigation sensors, this research analyzed the expected errors due to near-field effects using a coarse sun sensor as part of a 6-degree-of-freedom (6-dof) solution. To characterize these near-field effects, a test bed (Characterization Test Apparatus or CTA) was proposed, its design presented, and the design stage uncertainty analysis of the CTA performed. A candidate coarse sun sensor (NorthStar$_{TM}$) was chosen for testing, and a mathematical model of the sensor's functionality was derived. Using a Gaussian Least Squares Differential Correction (GLSDC) algorithm, the model parameters were estimated and a comparison between simulated NorthStar$_{TM}$ measurements and model estimates was performed. Results indicate the CTA is capable of resolving the near-field errors. Additionally, this research found no apparent show stoppers for using coarse sun sensors for 6-dof solutions.

DEDICATION

This thesis is dedicated to my wife Megan and my children Cali, Ethan, Sydney, and Ella. It has been a long row to hoe, but we've done it together.

ACKNOWLEDGEMENTS

I would like to thank my committee chair and advisor, Dr. Helen Reed, for her continued support not only through the course of this research, but also over the last five years as I have entered the world of spacecraft design, fabrication, and operation. I would also like to thank my committee members, Drs. John Hurtado and Alan Palazzolo, for their time in support of this research.

A great deal of thanks go to Lasse Maeland, without whose counsel this research may never have come to fruition. Thanks also go to Joe Perez, John Graves, Paul Lucas, Becky Sewell, and the rest of AggieSat Lab for making the past five years (and especially the last year and a half) the learning experience of a lifetime.

I would like to thank Colleen Leatherman for her help and support; she always seems to have the answer. Thanks also to Karen Knabe and Julie Wilson for their help and support when I failed to read the fine print.

My thanks go to my parents, my family, and my in-laws for their support and prayers during my tenure at Texas A&M University. Finally, thanks to my wife and children, who walked with me every step of the way.

TABLE OF CONTENTS

CHAPTER Page

Page

LIST OF FIGURES

Page

Page

Page

Page

LIST OF TABLES

NOMENCLATURE

θ	Angle between the sensor boresight vector and the light source
$\hat{\boldsymbol{n}}, \hat{\boldsymbol{b}}$	Unit vectors indicated by the carat symbol (^)
α	Angle between the sensor X-Y plane and the photovoltaic cells
V_i	Voltage on the i^{th} photovoltaic cell
H	Scale height from the sensor X-Y plane to the plane containing the light source
PV	Photovoltaic
$\boldsymbol{d_i}$	Distance from the sensor origin to the i^{th} PV cell
I_i	Intensity on the i^{th} PV cell
c_i	Relative radiant intensity on the i^{th} PV cell
γ	angle off LED boresight
$NSSH$	NorthStar$_{TM}$ sensor head
NS	NorthStar$_{TM}$
$\boldsymbol{u_i}$	Uncertainty in the i^{th} variable
$\mathcal{N}$	User-defined coordinate system attached to the NS sensor board
$\mathcal{O}$	Coordinate system of NSSH with unknown origin

CHAPTER I

INTRODUCTION AND MOTIVATION

As advancements in miniaturization in recent decades have decreased the size of electronics and sensor systems, there has been a push in the Aerospace industry to move towards smaller satellites capable of meeting a wide range of mission requirements and objectives for a lower cost than larger satellite systems. Sadin and Davis noted in 1994 that "exponential advances in performance per kilogram ("capability density") for spacecraft systems" helped generate renewed interest in small satellites [1]. While there is no formal definition of what constitutes a "small satellite," for the purposes of this thesis, a small satellite is defined as having a dry mass of less than 1000 kilograms. Rendleman, in a conference paper presented at the AIAA Space 2009 conference, argued that large satellites are difficult to resource, to baseline, and the programmatic risks are difficult if not impossible to control. Large satellite systems are complex and take a relatively long time to build. Often times requirements and additional payloads are added to the program late in the game, which increase the costs of the mission. As cost increases, so does the amount of testing required to assure the customer that the satellite will succeed, increasing the cost further [2]. Small satellites, however, have shorter development times and cost less to build and launch, reducing the budgetary risks associated with the satellite.

This thesis follows the style of *Journal of Spacecraft and Rockets*.

Small satellites are also capable of performing valuable risk reduction missions for key sensors and technology demonstrations. The Engineering Test Satellite-VII (ETS-VII) satellites were Japanese satellites built to demonstrate autonomous rendezvous and docking (ARD) technologies in anticipation of the development of the H-II transfer vehicle (HTV) [3]. The ETS-VII mission consisted of two satellites, a chaser and a target. While the chaser satellite was not a small satellite (mass of 2900 kg), the target satellite had a mass of only 400 kg. The mission was a success and demonstrated three different ARD technologies [4].

Orbital Express was a small satellite pair which successfully demonstrated autonomous rendezvous and capture technologies and the ability to perform on-orbit servicing of another spacecraft. The two satellites in the Orbital Express pair (ASTRO and NextSat) had dry masses of ~950 kg and ~230 kg, respectively[1].

Another small satellite mission, XSS-11, was required to safely rendezvous a micro-satellite (satellite on the order of 100 kg) with multiple derelict space objects [3]. XSS-11 proved to be hugely successful, and the satellite won the AIAA technical achievement award in 2007[2].

A subclass of small satellites is the University-class satellite, defined as a self-contained satellite on-orbit which has an independent means of communications, utilizes untrained personnel to perform a significant fraction of the design, fabrication, testing, and flight operations, and in which the training of the personnel is at least as important

[1] See DARPA's "Fact Sheet: Orbital Express," http://www.darpa.mil/orbitalexpress/pdf/oe_fact_sheet_final.pdf, March 2007 [retrieved June 2010].
[2] See "AIAA Honors Air Force Research Laboratory/Lockheed Martin Team With 2007 Technical Achievement Award," http://www.lockheedmartin.com/news/press_releases/2007/0919ss_xss11.html, September 2007 [retrieved June 2010].

as the nominal spacecraft mission [5]. Small satellites in this class are generally under 50 kg, and quite often are on the order of 1-3 kg (cubesats). Due to tight budgetary constraints, University-class satellites typically attack current industry challenges in innovative ways. Out of necessity, these satellites often incorporate Commercial-Off-The-Shelf (COTS) components which have no spaceflight heritage in mission critical subsystems, accepting the associated risks in order to push the envelope on small satellite performance.

One current technological challenge in the Aerospace industry is close-proximity operations, including ARD. Technologies utilized in missions such as ETS-VII, Orbtital Express, and XSS-11 are cost prohibitive and often too large for University-class satellites. The Laser mapper (LAMP) proposed for XSS-11 had a mass of approximately 6 kg and a power consumption of 35 Watts [6], while the Advanced Video Guidance System (AVGS) used on Orbital Express had a mass of 9 kg, consumed 20 Watts of power, and had external dimensions of 30.5 x 25.4 x 17.8 centimeters [7].

Several University-class satellites have been designed to tackle portions of the close-proximity problem. FASTRAC, a University of Texas at Austin satellite scheduled to launch in summer 2010[3], consists of a pair of satellites which intend to use Global Positioning System (GPS), magnetometers, inertial measurement units (IMUs), and a radio crosslink to perform sub-meter level accuracy relative navigation [8]. Another satellite, named CUSat and built by Cornell University, intends to perform autonomous relative navigation using carrier-phase differential GPS with centimeter

[3] See "Our Project: Overview," http://fastrac.ae.utexas.edu/our_project/overview.php, [retrieved June 2010].

accuracy[4]. While both of these satellites intend to perform relative navigation demonstrations, neither addresses sensors required to perform an ARD mission.

In order to perform close-proximity operations, and specifically an ARD mission, a satellite must be equipped with a sensor/sensor suite which allows the satellite to obtain a 6-degree-of-freedom (6-dof) solution for the target satellite. As mentioned previously, current technologies extant in the Aerospace industry are cost (and often mass and power) prohibitive for University-class spacecraft. University-class spacecraft often require sensors to be on the order of hundreds or thousands of dollars instead of hundreds of thousands of dollars. Additionally, University-class spacecraft have little surface area for solar panels, so sensors which need to be on for long periods of time will need to consume very little power.

Given the need for low-cost, low-mass, low-power solutions for University-class 6-dof relative attitude solutions, it is desirable to determine if a coarse sun sensor, a sensor many spacecraft already employ, can be used as the cornerstone for a 6-dof close-proximity operations solution. Coarse sun sensors have been in use for decades for attitude determination. However, a literature search turned up no information on whether coarse sun sensors had ever been tested and/or used for determining the position and pose of another spacecraft. If they can be used as the cornerstone for a 6-dof close-proximity operations solution, however, they would provide a readily available, low-cost, low-mass, low-power solution for 6-dof relative attitude determination.

---

[4] See "About CUSAT," http://cusat.cornell.edu/, [retrieved June 2010].

Due to the geometry of coarse sun sensors and assumptions made in their design, it is expected that error magnitudes in the 6-dof solution will increase as the sensor moves closer to the light source. In support of determining the viability of using a coarse sun sensor for 6-dof relative attitude determination, this research will focus on analyzing those errors (termed near-field errors) by modeling a coarse sun sensor/light source system. After determining the magnitudes of the expected near-field errors, a Characterization Test Apparatus will be proposed and designed which can be used to test a coarse sun sensor in order to characterize its near-field errors. The Characterization Test Apparatus will also be designed to accommodate future testing of the sensor. Finally, simulations will be run to determine the expected apparatus performance.

CHAPTER II

COARSE SUN SENSOR

In order to point sensors and other equipment correctly, a spacecraft must be able to determine its orientation with respect to some known inertial frame and then have the ability to reorient itself to the desired attitude. Of the many different sensor types available, one of the most widely used attitude determination sensor types is the sun sensor [9]. Several of the factors driving the popularity of sun sensors are outlined in reference [9], including the angular radius of the Sun being nearly orbit independent and small enough to allow it to be modeled as a point source (simplifying the sensor design and attitude determination algorithms). Additionally, many missions need to be able to either point solar panels to the Sun or keep other sensors pointed away from the Sun (e.g. star trackers) or a combination of both. In these cases, the spacecraft is already required to know the location of the Sun to some specified accuracy in order to determine the proper orientation of the spacecraft to meet pointing requirements.

While the many different applications have led to various types of Sun sensors, each different sensor can be grouped into one of three categories: analog sensors, Sun presence sensors, and digital sensors [9]. Analog sensors are those whose output signals are continuous and are functions of the Sun angle. Sun presence sensors, as their name suggests, provide a signal whenever the Sun is within their field of view (FOV), but no signal otherwise. Digital sensors have outputs which are functions of the Sun angle, but

in contrast to the analog sensors, digital sensors provide discrete outputs. This thesis will focus on analog sensors, and specifically cosine-type analog sensors.

Cosine-type Analog Sensor Functionality

One common type of analog sensor is the cosine-type, which derives its name from its method of operation. Analog sensors of this type generate vectors to the Sun based on the "sinusoidal variation of the output current of a silicon solar cell" due to Sun angle (see Figure 1) [9]. The energy flux through the solar cell (photovoltaic cell or PV cell) is only dependent on the component of the incident light which is normal to the PV cell. The energy per area (which generates a voltage and current) on the PV cell is therefore proportional to the cosine of the angle of incidence of the incoming light.

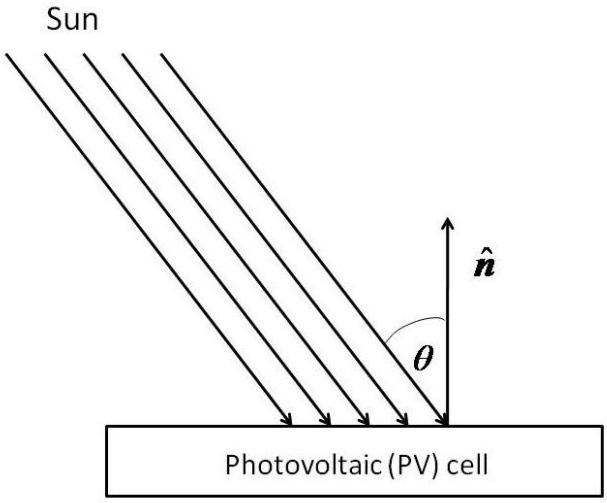

Figure 1 Cosine-type analog sensor.

The analog sensor shown in Figure 1 is only able to give one angle to the Sun. If the PV cell were rotated around its unit normal ($\hat{n}$) by any angle, the angle θ will not

change and therefore the voltage and current generated by the incoming light will not change. Additionally, the field of view of the sensor is limited to only that light which is in front of the PV cell (i.e. $\theta < 90°$). This simple analog sensor can be improved upon, however, by using it in conjunction with one or more additional PV cells.

Figure 2 depicts two cosine-type analog sensors with unit normals $\hat{\boldsymbol{n}}_1$ and $\hat{\boldsymbol{n}}_2$ each rotated from a generic axis X by an angle α as shown. This two cell system has a boresight vector as shown, and the Sun is at some angle off of boresight.

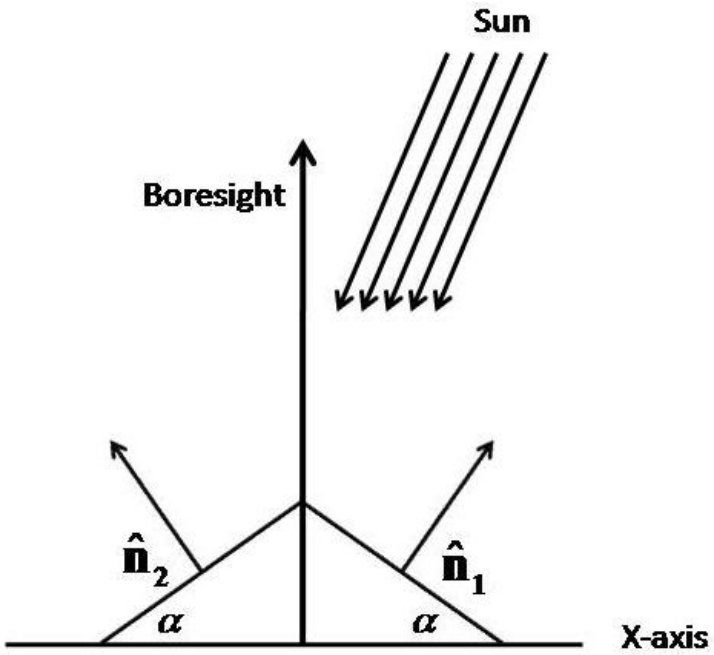

Figure 2 Two simple analog sensors used in conjunction.

The incoming sunlight will generate voltages and currents on the two PV cells proportional to the angle of incidence of the light with respect to the unit normals of the PV cells. By differencing the two voltages (or currents), and because the geometry of the two cell system is known, it is possible to determine where the Sun lies along the X-

axis. Notice that as the Sun moves toward the boresight, the angle of incidence of incoming light becomes the same for the two cells and the voltage generated on each PV cell becomes the same. When the Sun is at the system boresight, the voltages will cancel when differenced, and the result will be a zero value for the Sun along the X-axis. As the Sun moves to the "right," the voltage on the first panel will increase (as the light becomes more parallel with $\hat{\boldsymbol{n}}_1$) even as the voltage on the second panel decreases (the light becomes more orthogonal with $\hat{\boldsymbol{n}}_2$).

Conceptually extending the two PV cell system to a four PV cell system becomes trivial, though the implementation of such a system is not. Imagine the X-axis and the boresight vector in Figure 2 are part of a triad whose third member, the Y-axis, is generated by the right-hand rule (i.e. into the page). Imagine that the Y-axis also has a two PV cell system oriented such that the four cells create a pyramid of PV cells. Light from the Sun illuminates the PV cells located on of each of the four sides of the pyramid at some angle of incidence, causing a signal (e.g. voltage or current) to be generated at each cell based on the angle of incidence. By simply differencing the signals from the PV cells on opposite faces of the pyramid, a coarse direction to the sun is obtained. For pyramidal Sun sensors, however, simply differencing the voltages (i.e. $X = V_1 - V_2$) only works well when the Sun is near the boresight of the sensor. This is because the voltages on the X-axis pair of PV cells depend on where the Sun is located along the Y-axis (and vice versa).

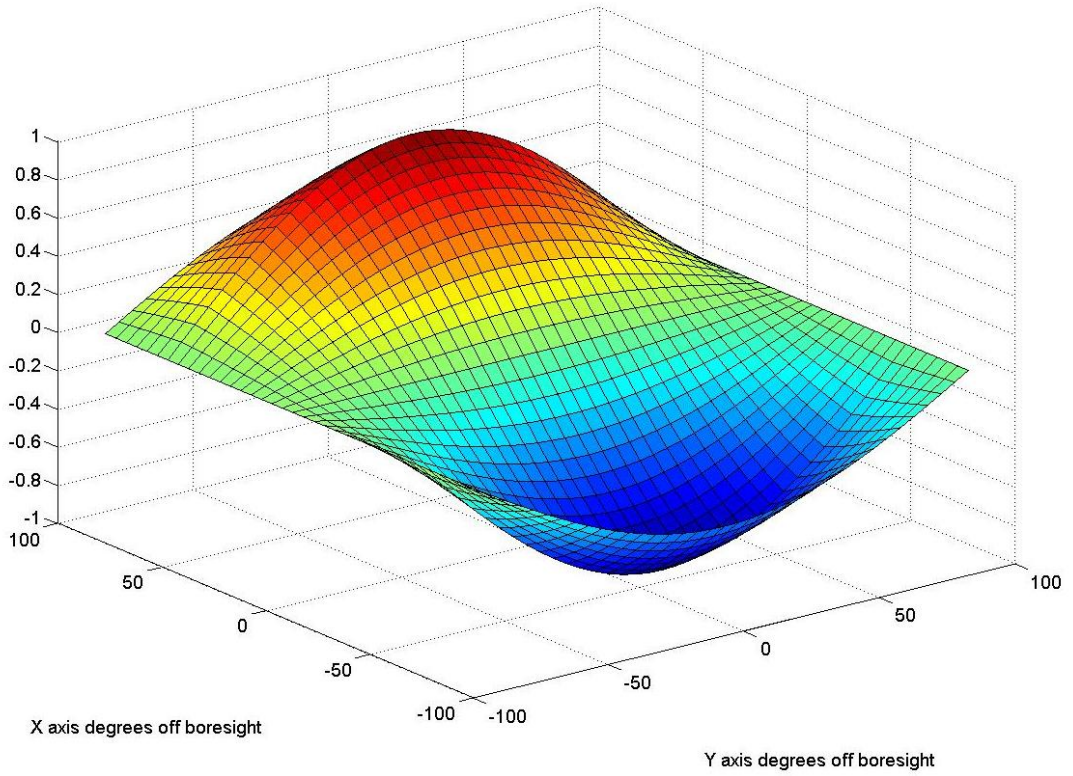

Figure 3 Plot of voltage output of cells on X-axis with respect to Sun angle boresight in the X and Y directions ($X = V_1 - V_2$ case).

Figure 3 shows the how the X-axis PV cell voltages depend on where the Sun is located on the Y-axis. Close to the sensor boresight, the graph is flat and there is very little dependence on Y. For a CSS, which is only trying to hold the Sun on its boresight, performing this simple differencing appears to work well. Outside of the narrow region around the boresight, however, the X output definitely depends on the location of the Sun in the Y-direction.

If the X distance is scaled by the sum of V_1 and V_2, however, the Y-location dependence is removed.

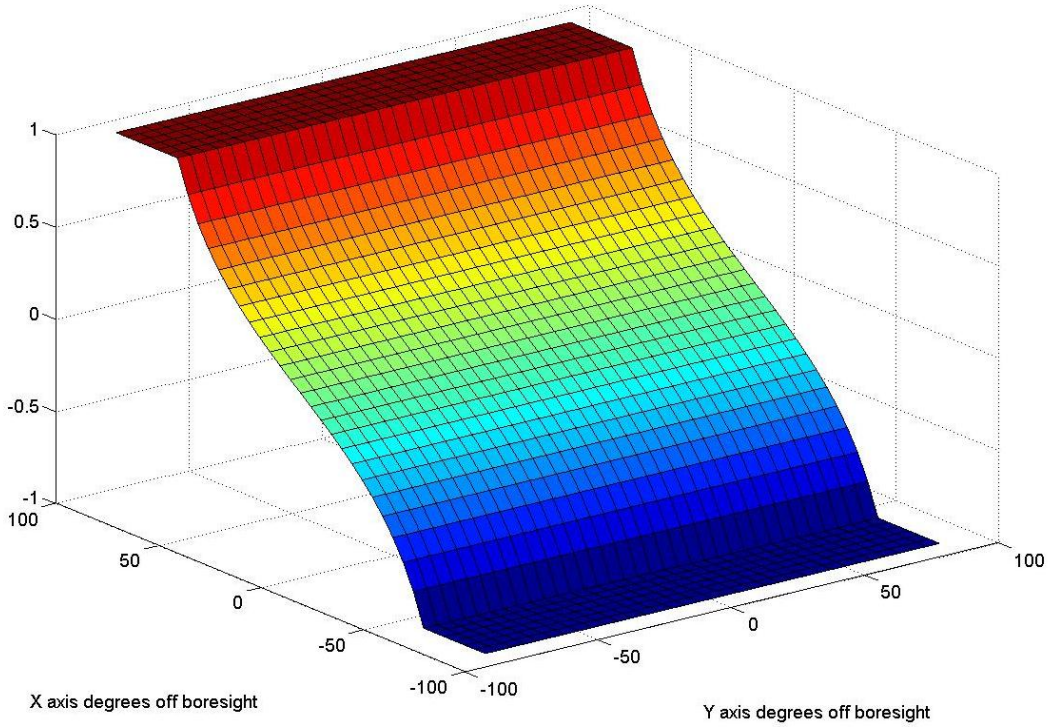

Figure 4 Plot of voltage output of cells on X-axis with respect to Sun angle off boresight in the X and Y directions ($X = (V_1-V_2)/(V_1+V_2)$ case).

From Figure 4, it can be seen that by scaling the X output by the sum of the two voltages, the dependence on the Y location of the light source has been removed.

These pyramidal-type Sun sensors can be categorized as Coarse Sun Sensors (CSS) because the resolution of these sensors tends to be on the order of degrees [9].

Near-field Error Sources for Sun Sensors

As mentioned previously, Sun sensors are designed specifically to take advantage of the fact that the Sun is a bright object far away from the Earth which can be modeled as a point-source. Under these assumptions, light rays from the Sun are parallel when they reach the Sun sensor as it orbits the Earth attached to a spacecraft. Additionally, the

light from the Sun has the same intensity when it reaches the four PV cells on a pyramidal CSS, so the voltage and/or current the light is capable of generating is the same for each PV cell.

However, if a CSS is to be used for close-proximity operations, its light source will not be one astronomical unit away but only feet or meters away. The question then becomes at what distance do the assumptions made for Sun sensors break down when using a CSS for close-proximity operations? As the light source approaches the CSS, errors (due to the physical geometry of the sensor) in determining the direction to the light source begin to accumulate and at some point become larger than the errors due to the sensor noise. To work as a close-proximity sensor, the CSS must be able to provide a vector pointing from the CSS to the light source with some uncertainty bound on the accuracy of the vector. Without any knowledge of how the errors in the vector from the CSS to the target change with respect to distance, it is impossible to attach a meaningful covariance to the measurements taken by the CSS.

This thesis defines the near-field as the region in which the errors due to physical geometry are greater than errors due to sensor noise. In the near-field, the assumptions which hold for Sun sensing are no longer valid, and the cost of breaking those assumptions (far-field assumptions) needs to be determined in order to use CSSs for close-proximity operations.

To begin determining the cost associated with breaking the far-field assumptions, a literature search was conducted to see what has already been done. The literature search turned up very little information on cosine-type CSSs in the public domain, and

nothing about any near-field effects. There are a number of companies that manufacture coarse sun sensors of this type[5,6], but their designs are proprietary and they have not published on possible near-field errors. One general description of how a specific CSS works can be found at the European Space Agency's website[7], but again, not any information about errors occurring in the near-field. As Sun sensors are a well-established technology, perhaps the information on near-field errors is included in reports from the mid-20th century which the author is unable to obtain. With no previous research available, mathematical models based on the geometry of the sensor were developed to obtain estimates for the magnitudes of the various near-field errors.

The baseline for comparing the near-field errors is the nominal model which assumes the light source is a point-source located at infinity. Additionally, the model is developed in two dimensions. The geometry for the baseline model is shown in Figure 5.

---

[5] See "Coarse Sun Sensor," http://www.aeroastro.com/pdfs/Coarse%20Sun%20Sensor%20Apr2010%20WEB.pdf, [retrieved June 2010].
[6] See "Coarse Sun Sensor (cosine-type)," http://adcole.com/css-pyramid.html, [retrieved June 2010].
[7] See "TNO Coarse Sun Sensor using European cells," http://telecom.esa.int/telecom/www/object/index.cfm?fobjectid=28404, 16 Dec. 2009 [retrieved June 2010].

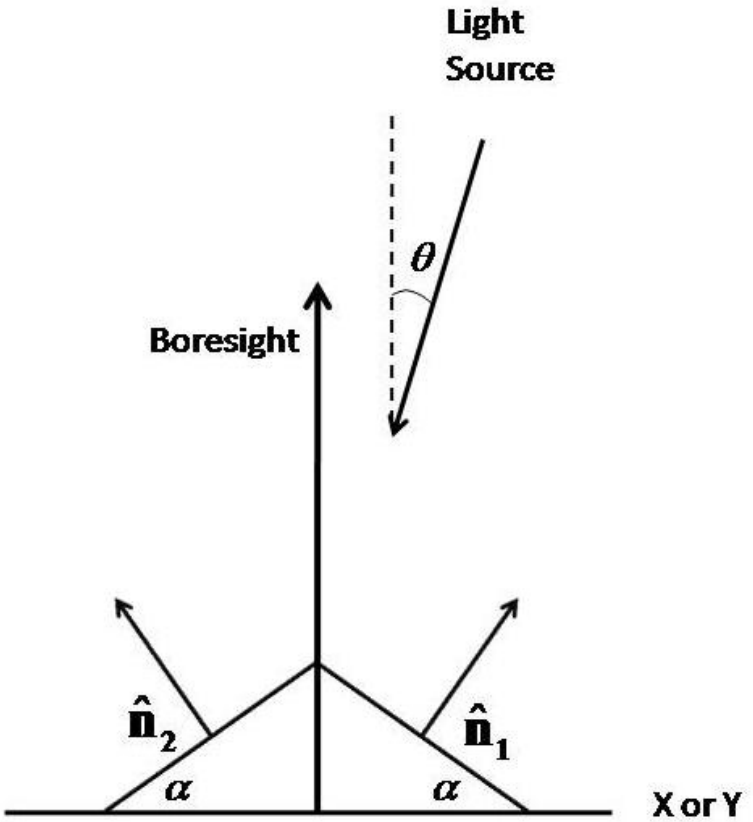

Figure 5 Baseline 2-D pyramid CSS model geometry

The incoming light makes an angle θ with respect to the boresight vector, and the voltage on each of the two PV cells can be described as a dot product of the incoming light vector and the unit normal to the PV cell. Writing the vector from the PV cells to the light source as

$$\hat{\boldsymbol{b}}_{\text{inf}} = \begin{bmatrix} \sin\theta \\ \cos\theta \end{bmatrix} \tag{1}$$

and the unit normal vectors as

$$\hat{\boldsymbol{n}}_1 = \begin{bmatrix} \sin\alpha \\ \cos\alpha \end{bmatrix}$$
$$\hat{\boldsymbol{n}}_2 = \begin{bmatrix} -\sin\alpha \\ \cos\alpha \end{bmatrix} \tag{2}$$

the "voltage" on the two PV cells can be expressed as

$$V_1 = \hat{\boldsymbol{n}}_1 \bullet \hat{\boldsymbol{b}}_{\text{inf}} = \sin\alpha\sin\theta + \cos\alpha\cos\theta$$
$$V_2 = \hat{\boldsymbol{n}}_2 \bullet \hat{\boldsymbol{b}}_{\text{inf}} = -\sin\alpha\sin\theta + \cos\alpha\cos\theta \tag{3}$$

Note that V_1 and V_2 are not actual voltages. However, since the actual PV cell voltage is proportional to the dot product of the incoming light vector and the PV cell normal vector, this thesis uses the term "voltage" as referring to V_1 and V_2.

The light source's orthogonal distance from boresight (X_{inf}, see Figure 6) is obtained by differencing the voltages V_1 and V_2 and then scaling that value by the sum of V_1 and V_2 in order to non-dimensionalize the X distance. Additionally, scaling the differenced voltages by the sum of V_1 and V_2 removes the Y dependence in the X direction. The equation for X_{inf} is written as

$$X_{\text{inf}} = \frac{V_1 - V_2}{V_1 + V_2} \tag{4}$$

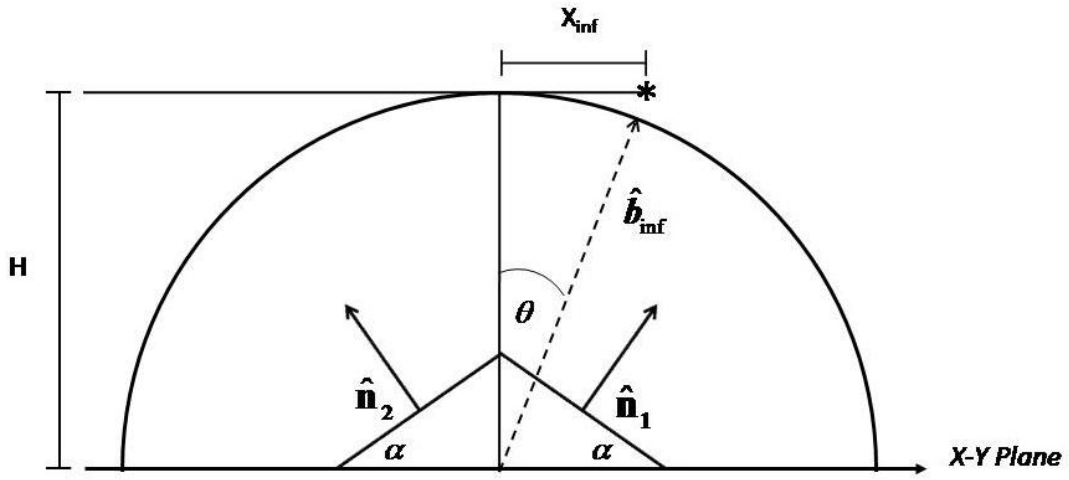

Figure 6 Orthogonal distance to light source from boresight.

The parameter H in Figure 6 represents a scale height between the X-Y plane of the CSS as shown in the figure and the plane in which the light source lies. H is assumed to be a constant parameter for each individual sensor. If X_{inf} is known at a specified angle θ, then the value for H can be determined using

$$H = \frac{X_{\inf}}{\tan(\theta)} \tag{5}$$

For the remainder of this work, an angle of 30° is assumed for the angle α. Note in general that where equation (4) is true and with some given angle α, the maximum angle off boresight is $[-\theta, +\theta]$ which satisfies the relationship $\tan\theta = \cot\alpha$. A plot of X_{inf} which assumes θ is in the range [-60°, 60°] is shown in Figure 7.

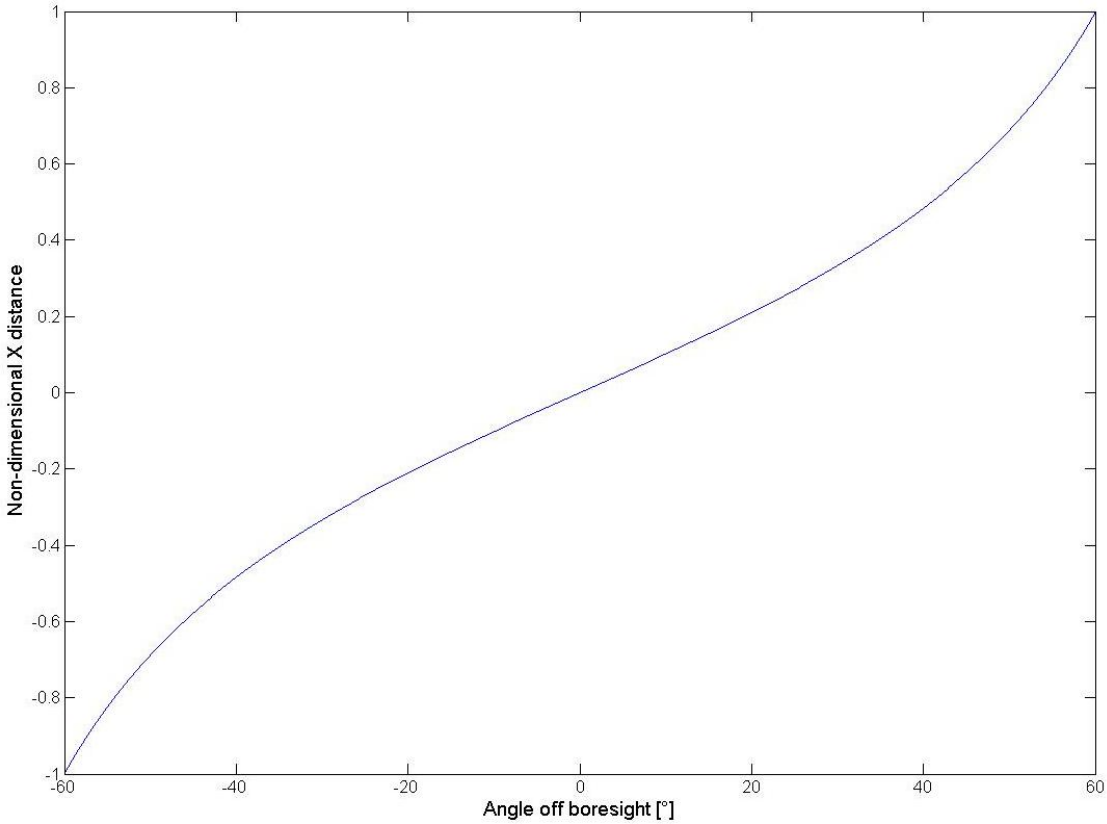

Figure 7 Values of X_{inf} from -60° to 60° for α = 30°

Notice that the model is fairly linear up to approximately 40° off boresight, but then becomes more nonlinear. Also, by non-dimensionalizing the distance X_{inf}, it now lies on the interval [-1, 1]. The value for θ_{inf} can be determined by taking the inverse tangent of the distance (X_{inf}) and the scale height H (assumed to be one in Figure 7).

$$\theta_{\text{inf}} = \tan^{-1}\left(\frac{X_{\text{inf}}}{H}\right) \tag{6}$$

With a nominal expression for θ_{inf}, the angle between the vector to the light source and the boresight vector, it is possible to determine the expected errors in θ_{inf} due to near-field effects.

Light source not infinitely distant

As mentioned previously, the CSS measurements will contain errors due to nonlinear effects which are present in the near-field but negligible in the far-field. The first of these effects discussed herein deals with the assumption that the light source (Sun) is infinitely far away from the sensor, so the incoming light rays are parallel. When using the CSS as a close-proximity sensor, the light source (beacon) is a finite distance from the CSS. As the distance between the beacon and the sensor decreases, the infinitely distant light assumption will break down because the incoming light rays are no longer parallel. As illustrated in Figure 8, the angle between the vectors pointing from the beacon(s) to the PV cells will cease being small as the beacon approaches the sensor. As the angle between the vectors opens up, the incoming light can no longer be assumed parallel.

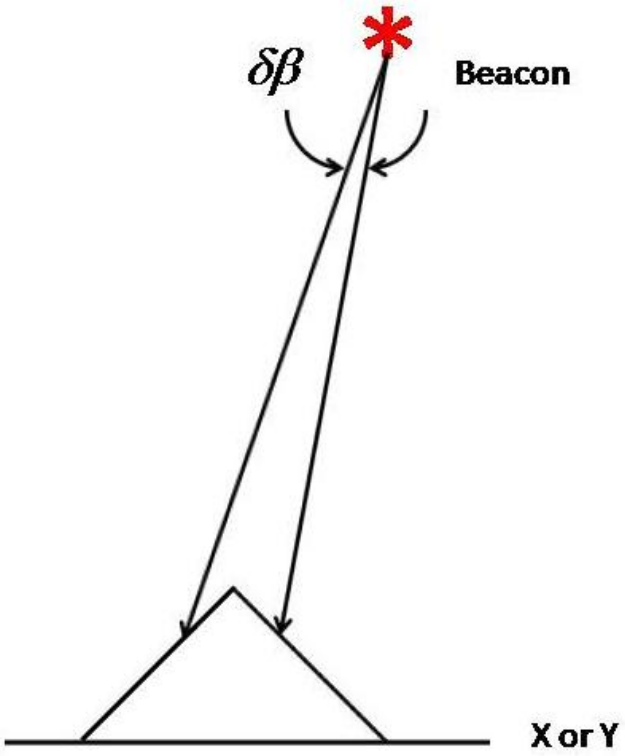

Figure 8 The nominal model assumes that δβ is infinitely small. As the beacon gets closer to the CSS, the angle opens up and the small angle assumption is no longer valid.

Vectors from the two PV cells to the beacon were then calculated in two different ways. The first set of vectors assumed the beacon was infinitely far away (equations (1) – (6)). With this assumption, the incoming light rays are parallel and will make the same angle with the PV cells no matter how the two cells are placed on the X-Y plane as long as they are not rotated. To better illustrate this, review Figure 9.

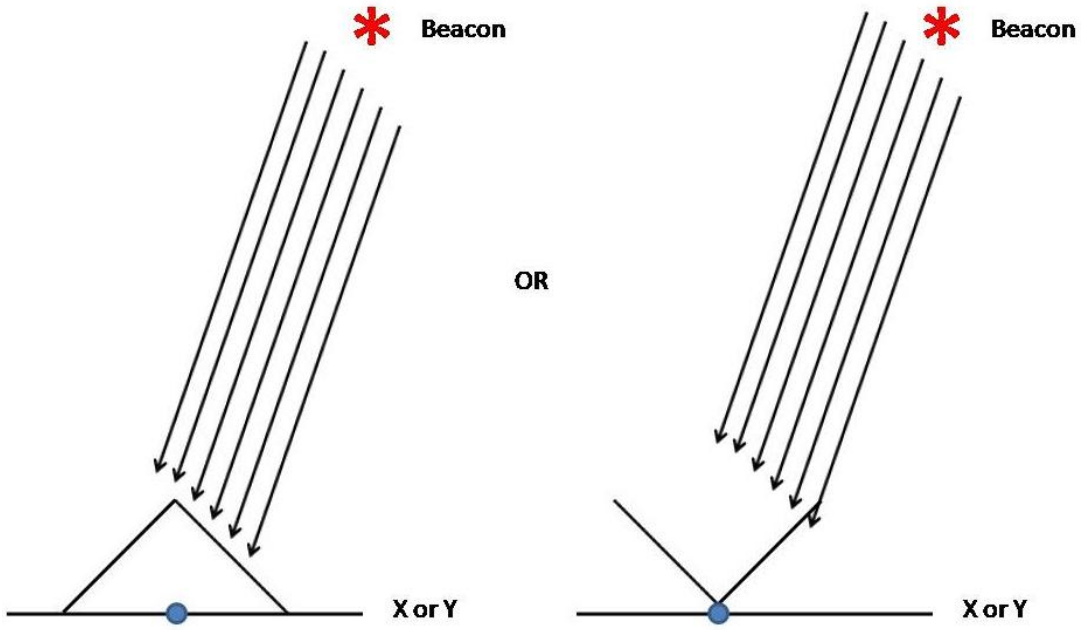

Figure 9 Light rays striking the photovoltaic cells from a source infinitely far away are parallel and therefore make the same angle with the cells whether the cells are fixed in their proper place or virtually moved such that they overlap.

One result of being able to slide the panels containing the PV cells is that when calculating the unit vector from the beacon to the panels, it can be assumed that the two PV cells are in the same location. Making this assumption means a single unit vector can be used to point to both panels. This assumption is valid because in the limit as the beacon moves to infinity, the distance between the two panels is effectively zero.

The second set of vectors from the PV cells to the beacon assumes correctly that the beacon is a finite distance away from the cells. Creating these vectors then includes taking the infinitely distant light source vector ($\boldsymbol{b}_{inf}$) and subtracting the vector from the origin to the PV cells. This is represented in Figure 10.

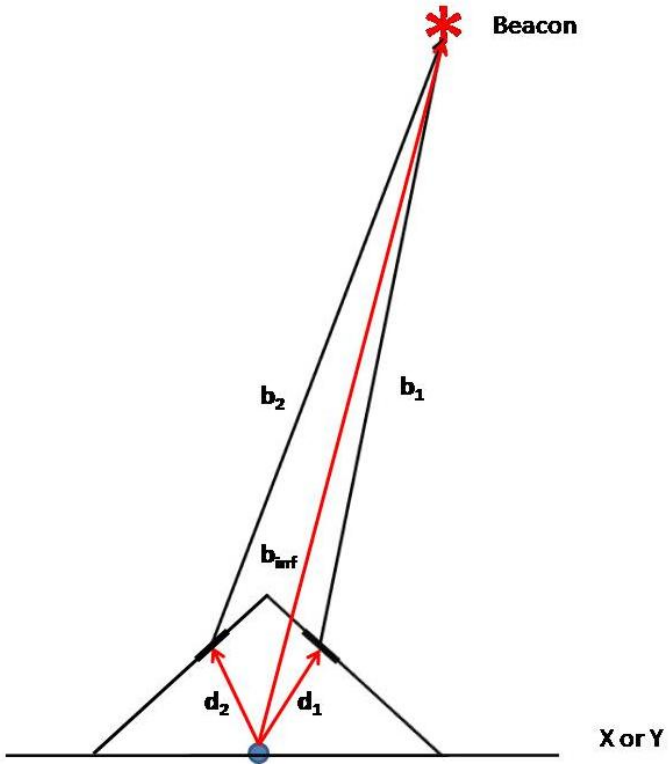

Figure 10 Illustration of the creation of the two vectors b_1 and b_2 required to analyze near-field effects. The short bold lines represent PV cells.

The equations to calculate the required vectors $\boldsymbol{b_1}$ and $\boldsymbol{b_2}$ are given in (7).

$$\begin{aligned} \boldsymbol{b}_1 &= \boldsymbol{b}_{\text{inf}} - \boldsymbol{d}_1 \\ \boldsymbol{b}_2 &= \boldsymbol{b}_{\text{inf}} - \boldsymbol{d}_2 \end{aligned} \tag{7}$$

where $\boldsymbol{d_1}$ and $\boldsymbol{d_2}$ are vectors representing the offset between the origin of the CSS (blue circle on X or Y axis) and the centers of the two PV cells.

The vectors $\boldsymbol{b_1}$ and $\boldsymbol{b_2}$ shown in Figure 10 actually represent "average" vectors to the light source. PV cells have a finite area, and each infinitesimal portion of that area generates voltage based on the angle of incidence of the incoming light with respect to the infinitesimal area. Looking at Figure 10, the voltage generated by the light at each

location down the PV cell will be different because the incidence angles will be slightly different. This is illustrated in Figure 11. The vector from the top of PV cell 1 to the beacon (vector $\boldsymbol{b_{11}}$) is different from the vector from the bottom of PV cell 1 to the beacon (vector $\boldsymbol{b_{1f}}$). As the distance between the PV cell and the beacon becomes large compared to the length (L) of the PV cell, the two vectors ($\boldsymbol{b_{11}}$ and $\boldsymbol{b_{1f}}$) become the same.

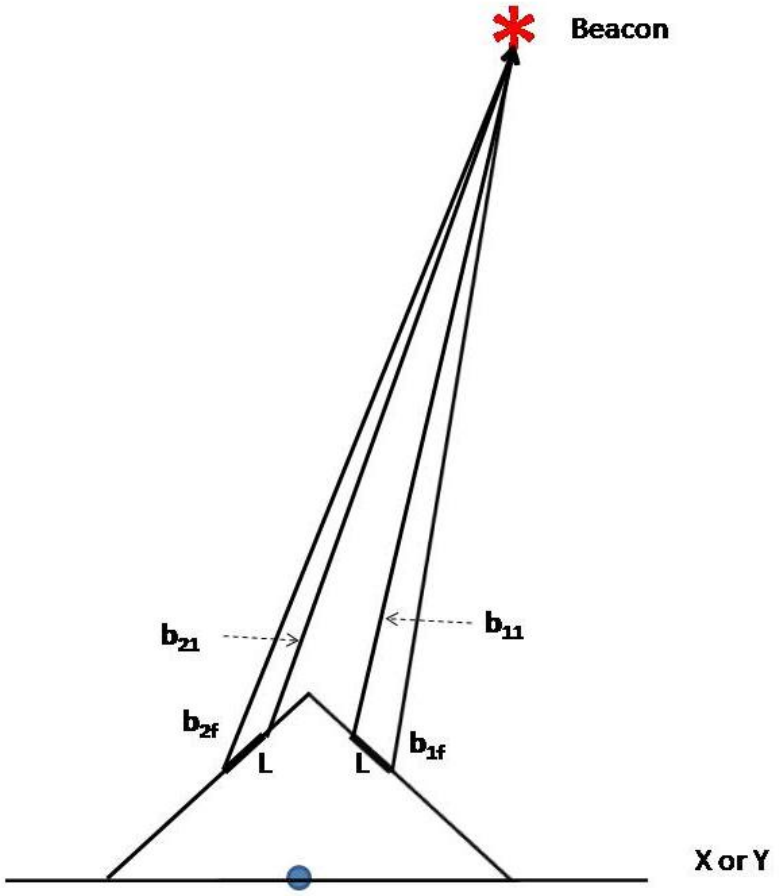

Figure 11 Illustration of how the angle of incidence changes over the length (L) of each PV cell.

The PV cells, however, do not output voltages at each infinitesimal area. Instead, they will only output a voltage which is the average of all the voltages generated at each

infinitesimal area. The vectors $\boldsymbol{b_1}$ and $\boldsymbol{b_2}$ from Figure 10 represent the vectors from the PV cell centers to the beacon which, when dotted with the unit normal of the PV cell, will generate the average voltage. The PV cell centers were chosen based on an analysis shown in Appendix, which indicates that average voltage output is effectively located at the center of the PV cells. For all the near-field errors discussed in this thesis (close-proximity, intensity variations, and non-uniform light sources), the vector from the PV cell to the beacon will originate at the center of the PV cell, and the PV cell will be treated as a point.

Notice that the vectors $\boldsymbol{b_1}$ and $\boldsymbol{b_2}$ (in Figure 10) are not unit vectors, but have some length. The sensor diameter introduced in Figure 12 is a parameter used for non-dimensionalizing the vectors $\boldsymbol{b_1}$ and $\boldsymbol{b_2}$, and it is defined as the distance between the centers of the PV cells on an axis. By non-dimensionalizing the vectors to the beacon by the sensor diameter, the results from this analysis will be able to scale to many different coarse sun sensors. This non-dimensionalization holds for any value of α (see Figure 13). For the remainder of this chapter, all vectors of length are divided by the sensor diameter.

In order to compare the vectors $\boldsymbol{b_1}$ and $\boldsymbol{b_2}$ to the infinite case, equations (7) need to be normalized. Normalizing equations (7) results in

$$\hat{\boldsymbol{b}}_1 = \frac{\boldsymbol{b}_1}{|\boldsymbol{b}_1|} = \frac{\boldsymbol{b}_{\inf} - \boldsymbol{d}_1}{|\boldsymbol{b}_{\inf} - \boldsymbol{d}_1|}$$

$$\hat{\boldsymbol{b}}_2 = \frac{\boldsymbol{b}_2}{|\boldsymbol{b}_2|} = \frac{\boldsymbol{b}_{\inf} - \boldsymbol{d}_2}{|\boldsymbol{b}_{\inf} - \boldsymbol{d}_2|} \tag{8}$$

As with the baseline model, incoming light striking the two PV cells will generate a voltage in each that is dependent on the incidence angle of the light (with respect to the normal to each PV cell).

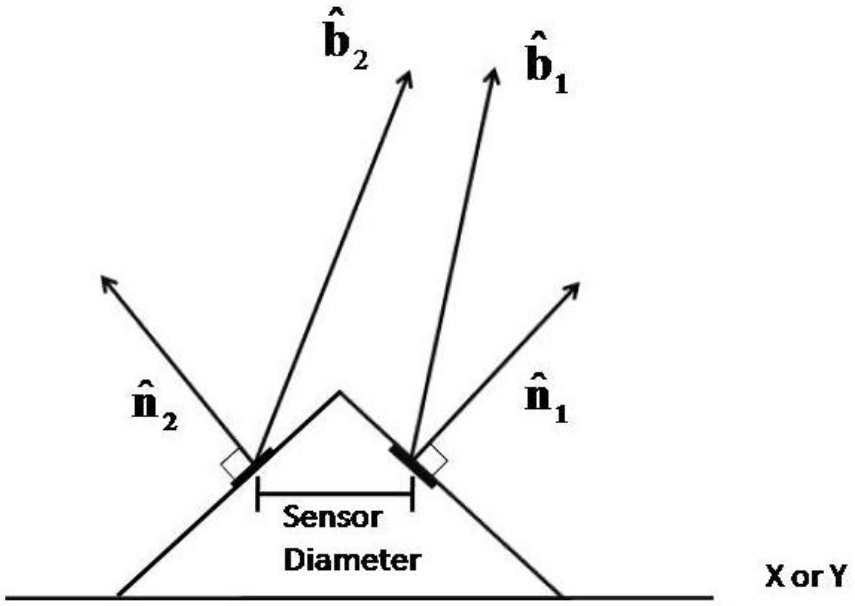

Figure 12 Unit vectors to the light source and PV cell normal vectors. The short, bold lines represent PV cells. The sensor diameter is the distance between the origins of the unit vectors to the light source.

The vectors $\hat{\mathbf{n}}_1$ and $\hat{\mathbf{n}}_2$ again represent the unit normals to PV cell 1 and PV cell 2, respectively. Writing equations for the voltages generated by the incoming light on both PV cells yields equations (9), where the subscript "cp" stands for close-proximity.

$$V_{1,cp} = \hat{\boldsymbol{n}}_1 \bullet \hat{\boldsymbol{b}}_1$$
$$V_{2,cp} = \hat{\boldsymbol{n}}_2 \bullet \hat{\boldsymbol{b}}_2 \tag{9}$$

The voltages generated by the incoming light are then converted into an X distance in the same manner as in the baseline case, namely:

$$X_{cp} = \frac{V_{1,cp} - V_{2,cp}}{V_{1,cp} + V_{2,cp}} \tag{10}$$

As in equation (6), the angle θ_{cp} can be found by taking the inverse tangent of X_{cp} and the scale height H.

$$\theta_{cp} = \tan^{-1}\left(\frac{X_{cp}}{H}\right) \tag{11}$$

The error in the angle due to proximity effects can then be written as

$$\delta\theta = \theta_{\text{inf}} - \theta_{cp} \tag{12}$$

where δθ is as shown in Figure 13.

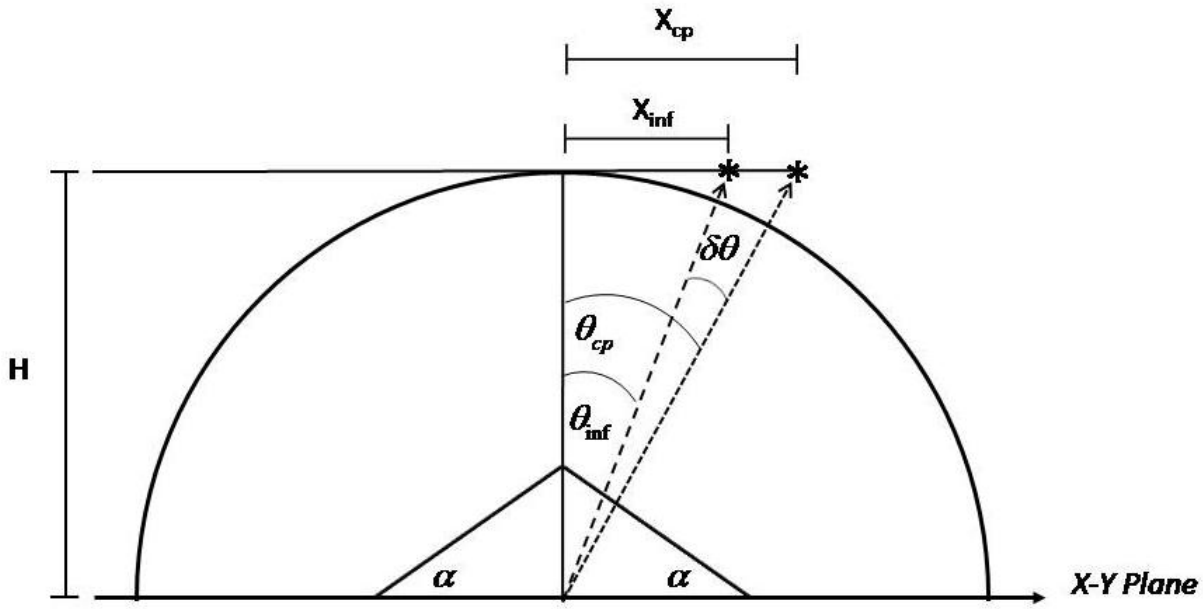

Figure 13 Error in angle due to proximity effects.

In order to quantify the expected errors in angle (δθ) due to proximity effects, the problem was modeled two dimensionally in MATLAB. The model assumed a single beacon placed about three sensor diameters from the CSS, but offset from the boresight

by a specified angle (i.e. fixed θ_{inf}). The beacon was then brought in along the line of constant θ_{inf} and the error in the angle was plotted, with results shown in Figure 14. Using the listed value of the European coarse sun sensor[8] as an order of magnitude check on expected errors due to sensor noise, it is assumed that there will be approximately 0.1° error due to the sensor itself. Note that the approximate error referenced is for a CSS which does not account for near-field effects. How the noise of the sensor changes when the light source is in the near-field is unknown and is only assumed to be constant.

Figure 14 shows the errors in the angle θ due to proximity effects. Around 70 sensor diameters, the errors due to proximity effects (when θ equals six degrees) are of the same order as the expected errors due to noise. These errors are sensitive to changes in the angle α, with the errors increasing with increasing α and decreasing as α decreases. Figure 15 shows a close-up view of Figure 14 with the X-axis being cut at 350 sensor diameters.

[8] See "TNO Coarse Sun Sensor using European cells," http://telecom.esa.int/telecom/www/object/index.cfm?fobjectid=28404, 16 Dec. 2009 [retrieved June 2010].

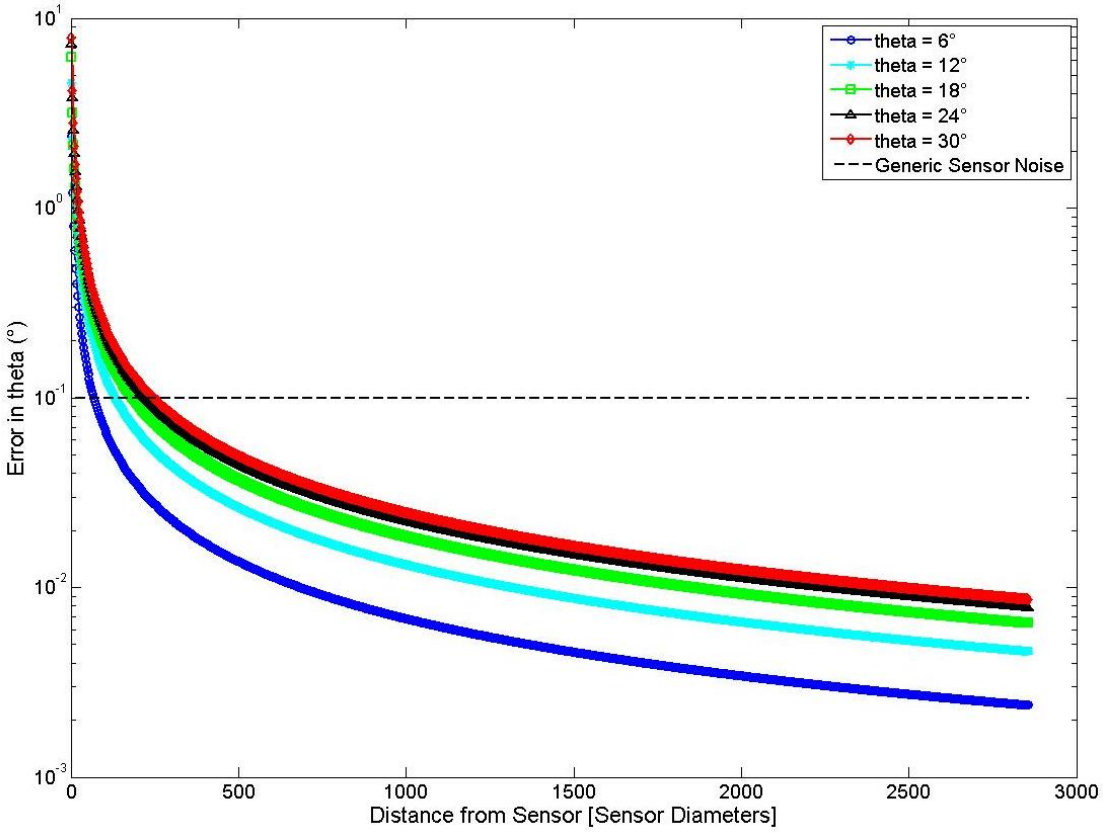

Figure 14 Error in θ (δθ) due to beacon proximity plotted as a function of sensor diameter.

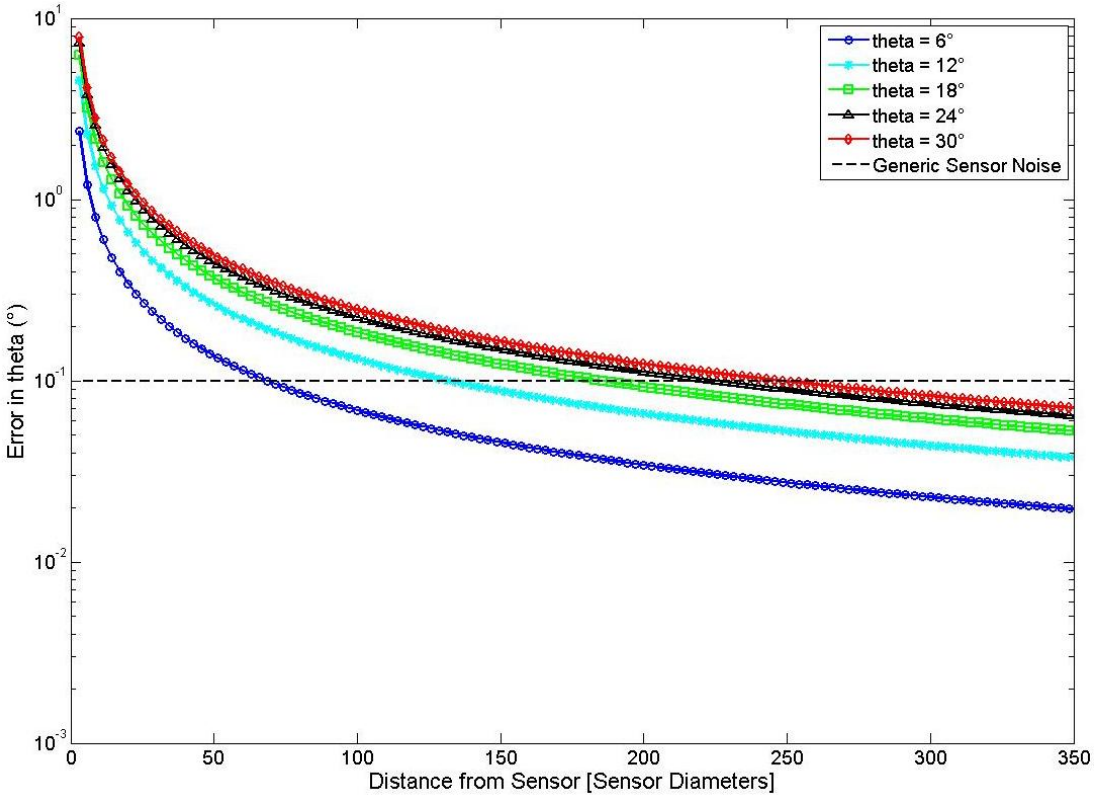

Figure 15 Close-up view of the errors in the angle due to proximity effects at $\alpha = 30°$.

Notice that as the light source moves away from the sensor (towards infinity), the errors asymptotically approach zero. However, as the light approaches the sensor, the errors asymptotically approach infinity. Between fifty and one hundred sensor diameters separation distance, the errors begin to increase rapidly, continuing to accelerate towards infinity with each inward step.

For close-proximity operations in which the two spacecraft maintain a separation of greater than 100 sensor diameters or so (depending on the actual sensor noise), errors in the estimated line of sight vector from the CSS to the beacon may not be affected by the proximity of the beacon to the CSS; those errors may be lost in the noise of the

sensor. However, in an ARD mission for which the goal is a successful docking maneuver, the errors in the estimated line of sight vector become significant as the spacecraft approach each other.

Errors due to intensity variations

Another assumption inherent in a CSS model is the light incident on all the PV cells has the same intensity, meaning it has the same voltage generation potential. Light intensity (with units of energy per area) follows an inverse square law, with the intensity falling off as the inverse of the distance squared. At great distances, the denominator is changed very little when account is taken of the fact the PV cells are located some distance apart. In a CSS, the distance from the light source (Sun) to the CSS is on the order of one astronomical unit, so adding or subtracting the PV cell separation distance is insignificant.

However, as the light source approaches the sensor, the PV cell separation distance becomes more significant. The X distances are computed based on a differencing of voltages on PV cells opposite each other. Differing intensities on each of those PV cells would cause a difference in the voltage generated in each independent of the proximity of the sensor to the beacon. This difference in voltage due to intensity differences would generate an inaccurate X distance and therefore an error in the angle ($\delta\theta$).

Referring to Figure 10, it is possible to write

$$r_1 = |\boldsymbol{b}_1|$$
$$r_2 = |\boldsymbol{b}_2| \tag{13}$$

where r_1 and r_2 are the magnitudes of the distance between the sensor and the beacon. Using (13) and assuming the beacon radiates in a uniform manner, the intensity at each PV cell can be written as

$$I_1 = \frac{P_0}{r_1^2}$$
$$I_2 = \frac{P_0}{r_2^2} \tag{14}$$

where P_0 is the initial power output at the beacon. The voltages on the PV cells are calculated as in equations (3), and the intensity values from (14) are used to scale the result to make X_I.

$$X_I = \frac{I_1 V_1 - I_2 V_2}{I_1 V_1 + I_2 V_2} \tag{15}$$

Notice that because P_0 appears in each term, it can be cancelled so that the X distance does not depend on the initial power output at the beacon, only on the relative intensities at the PV cells. Also notice that when I_1 equals I_2, the intensities will all cancel and equation (15) simplifies to equation (4).

An illustration of the near-field errors in angle ($\delta\theta$) due to intensity is shown in Figure 16. Similar to the near-field errors caused by proximity, the near-field errors in angle due to intensity ($\delta\theta$) can be written as

$$\delta\theta = \theta_{\text{inf}} - \theta_I \tag{16}$$

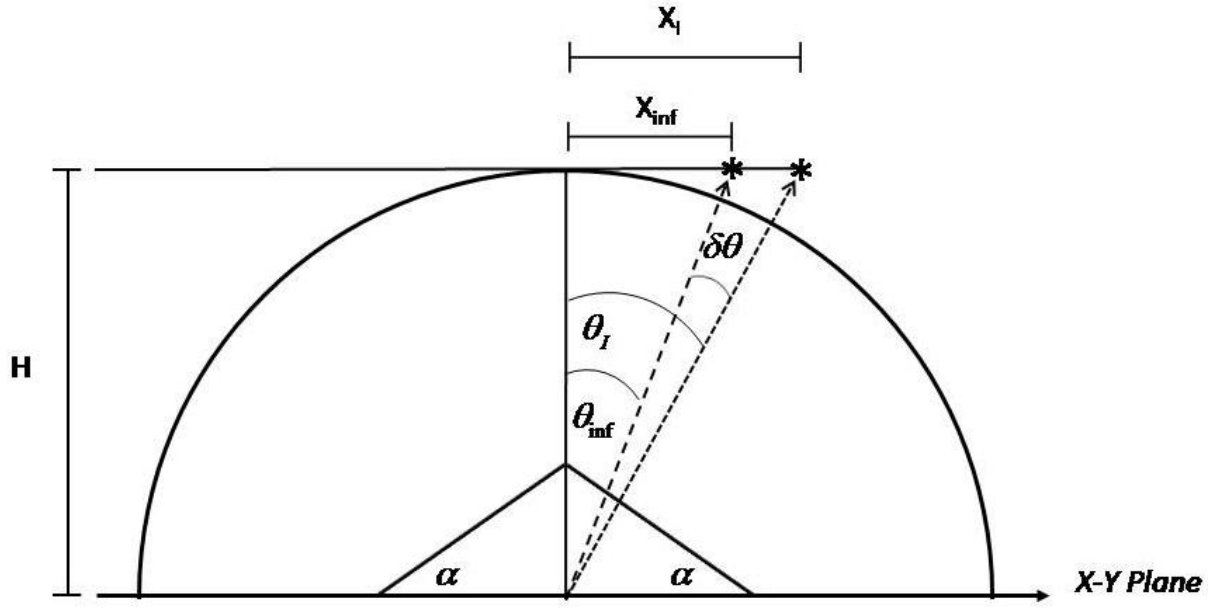

Figure 16 Illustration of errors in angle (δθ) due to differences in intensity.

To quantify the magnitude of the expected errors in angle due to differences in intensity, a model similar to the one created for the proximity effects was generated in Matlab, with a beacon again being placed at three sensor diameters and moved outwards from the sensor. The results of this simulation are shown in Figure 17.

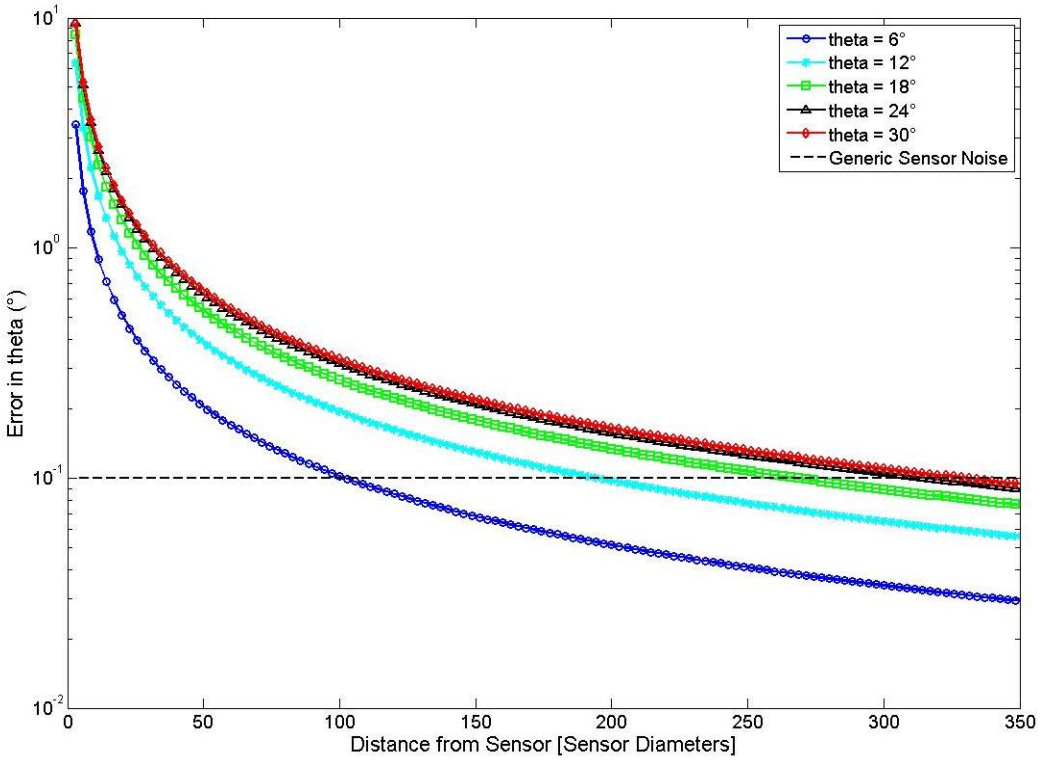

Figure 17 Errors in angle (δθ) due to differences in intensity at the PV cells plotted to 350 sensor diameters.

The results are similar to those for the errors in angle due to proximity. The errors are somewhat larger, with errors greater than the expected noise for all θ at around 100 sensor diameters. The effect becomes more pronounced as the beacon moves in closer to the sensor, with the errors beginning to change rapidly starting between ten and twenty inches and moving inward.

Errors due to a non-uniform light source

Using a CSS for a close-proximity sensor necessitates the selection of a light source to act as a beacon for the sensor to locate. In the previous section, the light source selected was assumed to be a uniform light source, radiating the same in all

directions. In reality, the light source will have some amount of directionality which makes the intensity of the incoming light to the CSS not only a function of distance, but also a function of direction from the boresight of the light source. Figure 18 illustrates the manner in which beacon orientation and radiant intensity profile affect the intensity at the CSS. The dashed lines represent the radiant intensity profile (i.e. the directionality) of the beacon.

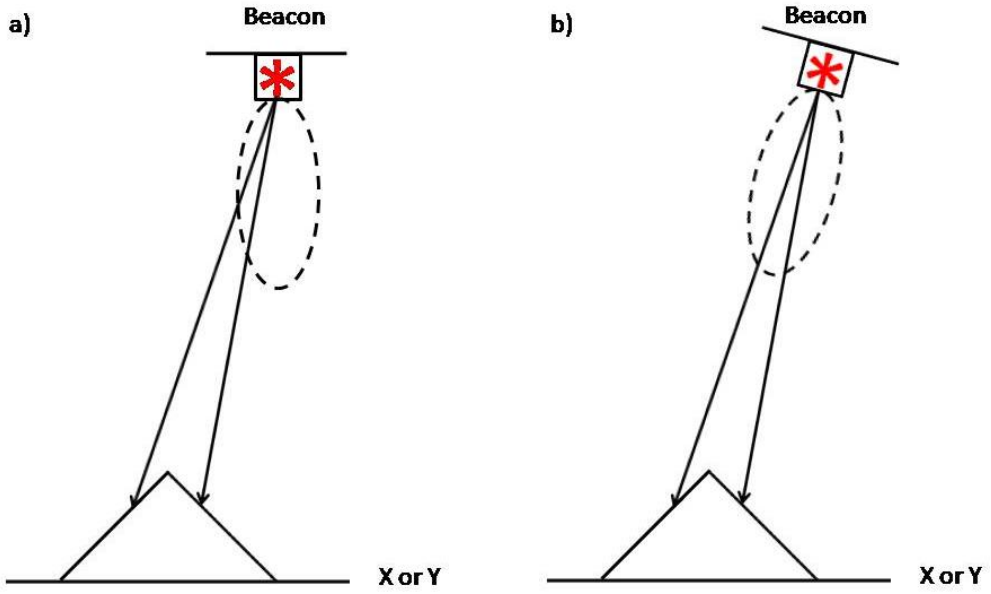

Figure 18 The intensity of the light at the PV cells depends on the beacon's radiant intensity profile and orientation.

Notice that in Figure 18a, the beacon is oriented parallel to the sensor's XY plane. The light vector to the left PV cell begins its journey with less intensity than the vector to the right PV cell due only to the orientation of the beacon. Due to the directionality of the beacon, the PV cell on the left will generate less voltage than it would generate if the beacon had a uniform light distribution. Upon differencing the two

sides of the sensor, the net effect will be the sensor predicting the beacon is farther to the right than it actually is.

Figure 18b shows the beacon in the same location as before, but now it is oriented differently. The vectors to the two PV cells pass through portions of the radiant intensity profile that are approximately equal, so the effect of the beacon light directionality is minimal. Note that if the beacon had been rotated a little farther, the beacon would be oriented such that the sensor would think the beacon was located farther to the left than it actually is.

The effects of these non-uniform errors decrease as the beacon radiant intensity profile becomes more uniform, i.e. when the slope of the profile does not change quickly with angle off boresight. To illustrate this point, replace the beacons in Figure 18 with beacons with a more evenly distributed intensity profile (see Figure 19).

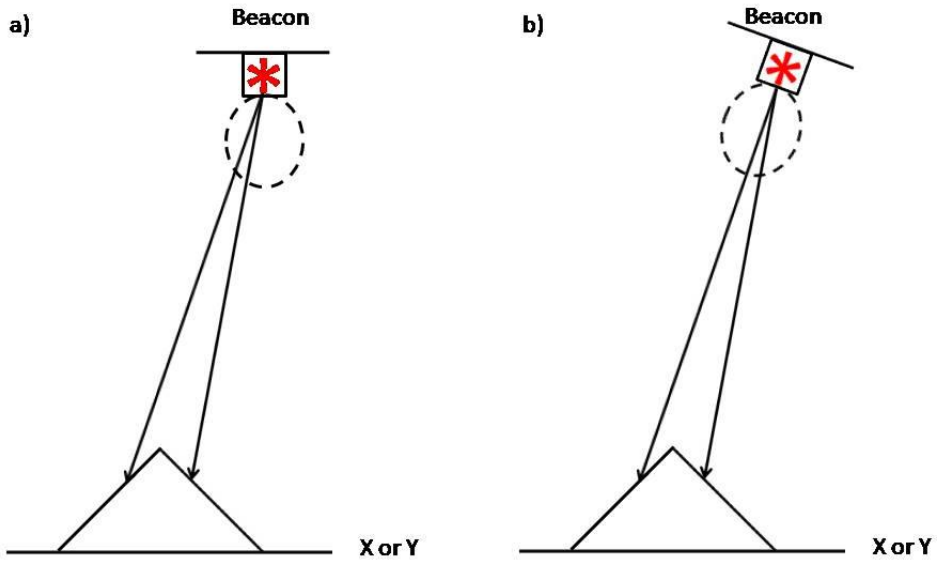

Figure 19 Less directional beacons decrease the magnitude of the errors associated with using a non-uniform light source.

Errors caused by the light source being non-uniform, unlike the other two near-field error sources, depend on the orientation of the beacon and its radiant intensity profile. While these facts make the errors application specific, a specific geometry will be assumed in order to obtain an estimate for the expected magnitude of this effect. The following assumes the use of the Vishay® VSML3710 LED [10] as the light source. This Light Emitting Diode (LED) has a half-intensity angle of 60°.

In order to obtain an expression for the relative radiant intensity of the beacon with respect to the angle off boresight, values for the relative intensity versus angle were obtained from the component datasheet and plotted in Microsoft Excel. The data points were then fit with a quartic polynomial using Excel's built-in trend line tool. The result is shown in Figure 20. The equation for the quartic polynomial which fit the data points is

$$c_i = \left(-4\times10^{-7}\right)\gamma_i^4 - \left(4\times10^{-6}\right)\gamma_i^3 + \left(5\times10^{-5}\right)\gamma_i^2 - \left(1\times10^{-3}\right)\gamma_i + 1 \qquad (17)$$

where c_i is the relative radiant intensity and γ_i is the angle off the LED boresight.

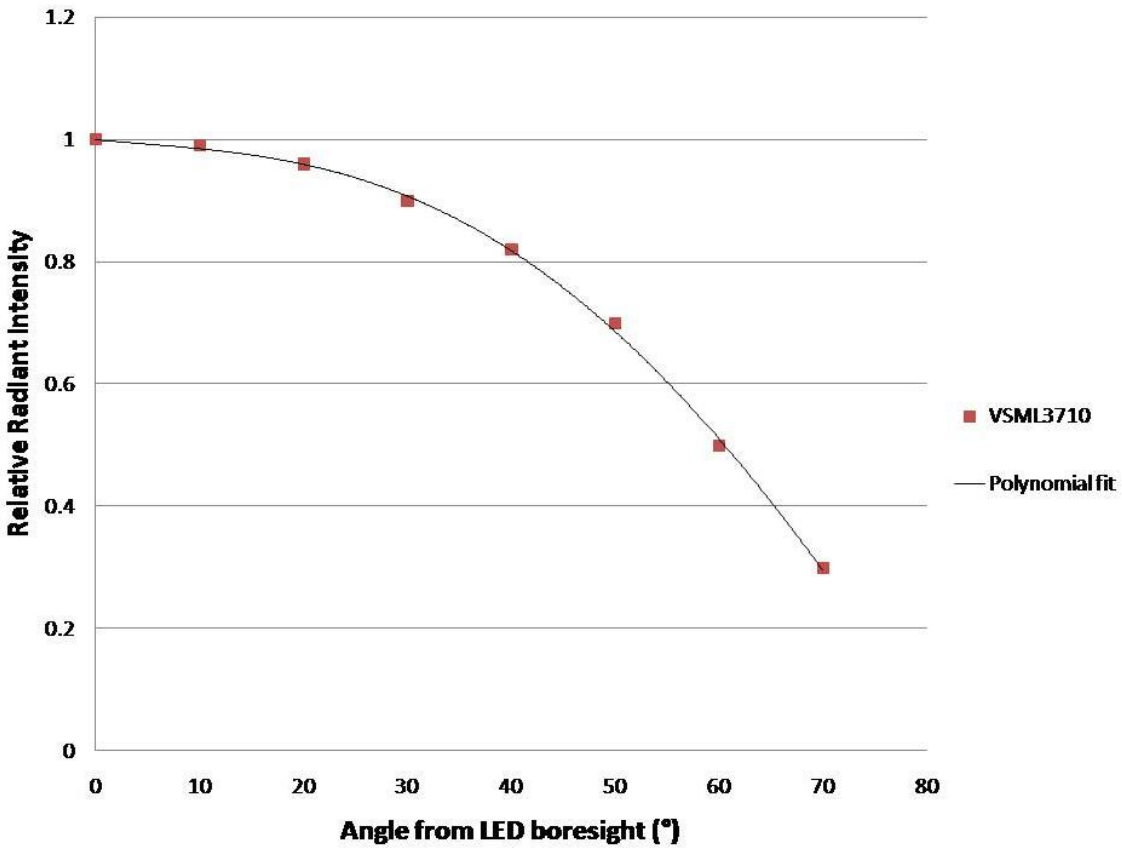

Figure 20 VSML3710 relative radiant intensity profile. The points were taken from the VSML3710 datasheet.

The VSML3710 has a symmetric radiant intensity profile, so only half of the distribution was plotted in Figure 20. Additionally, the plot displays the relative radiant intensity with respect to the angle off the LED's boresight. All of the intensity values, therefore, have been normalized by the maximum intensity (along the boresight of the component).

In order to isolate the errors caused by the non-uniform beacon, effects due to beacon proximity and uniform light source intensity need to be removed. Begin with equation (4)

$$X_{\text{inf}} = \frac{V_1 - V_2}{V_1 + V_2}$$

and introduce an intensity as if the light source was at infinity.

$$I_{\text{inf}} = \frac{P_0}{r_{\text{inf}}^{\ 2}}$$
$$r_{\text{inf}} = \left|\boldsymbol{b}_{\text{inf}}\right| \tag{18}$$

where $\boldsymbol{b}_{\text{inf}}$ is defined in Figure 10. Equation (4) is thus modified as

$$X_{non} = \frac{I_{\text{inf}} V_1 - I_{\text{inf}} V_2}{I_{\text{inf}} V_1 + I_{\text{inf}} V_2} \tag{19}$$

Without any additional manipulation, equation (19) is identical to equation (4). However, there are no terms in equation (19) which depend on the radiant intensity profile of the beacon. In order to determine what these terms are, assume the beacon is parallel with the sensor XY plane as in Figure 19a. The relative intensity of each vector depends on the angle from the beacon boresight to the vector (Figure 21).

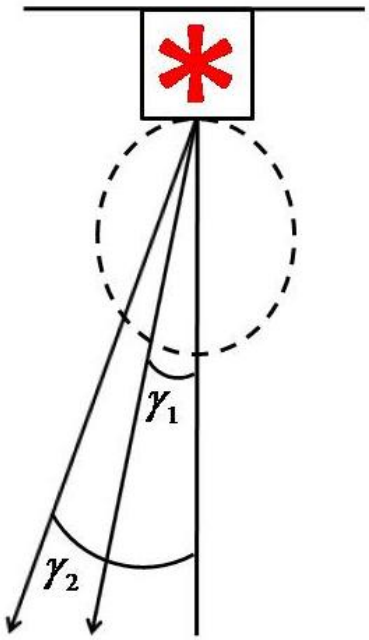

Figure 21 Angle from beacon boresight.

By substituting the angles (γ_1 and γ_2) into the quartic polynomial obtained from fitting the VSML3710 relative radiant intensity profile (see equation (17)), scaling factors (c_1 and c_2) dependent on the angle from boresight are obtained. Augmenting equation (19) with these scaling factors allows the equation to be written as

$$X_{non} = \frac{c_1 I_{\inf} V_1 - c_2 I_{\inf} V_2}{c_1 I_{\inf} V_1 + c_2 I_{\inf} V_2} \tag{20}$$

As with the previous near-field errors, the error in the angle ($\delta\theta$) due to the beacon being a non-uniform source can be found by solving the equation

$$\delta\theta = \theta_{\inf} - \theta_{non} \tag{21}$$

where

$$\theta_{non} = \tan^{-1}\left(\frac{X_{non}}{H}\right) \tag{22}$$

The magnitude of this error is plotted below in Figure 22.

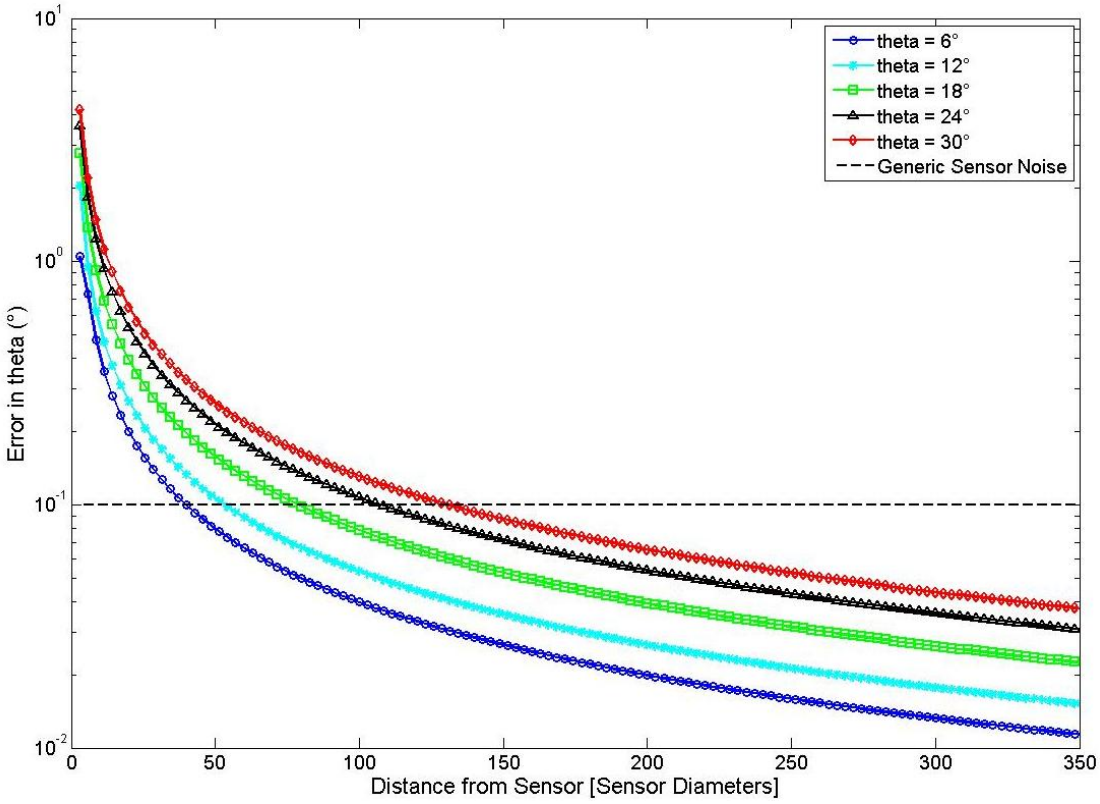

Figure 22 Errors in angle (δθ) due to the light source being a non-uniform emitter with 60° half-intensity angle.

The magnitudes of the errors shown in Figure 22 are on the order of 1.75-2.5 times less than the error in angle (δθ) due to proximity and 2.5-4 times smaller than the error in angle (δθ) due to differences in intensity for a uniform light source.

The three near-field errors discussed in this thesis were formulated in such a way that they are additive. Combining the three near-field errors yields total expected error magnitudes shown in Figure 23.

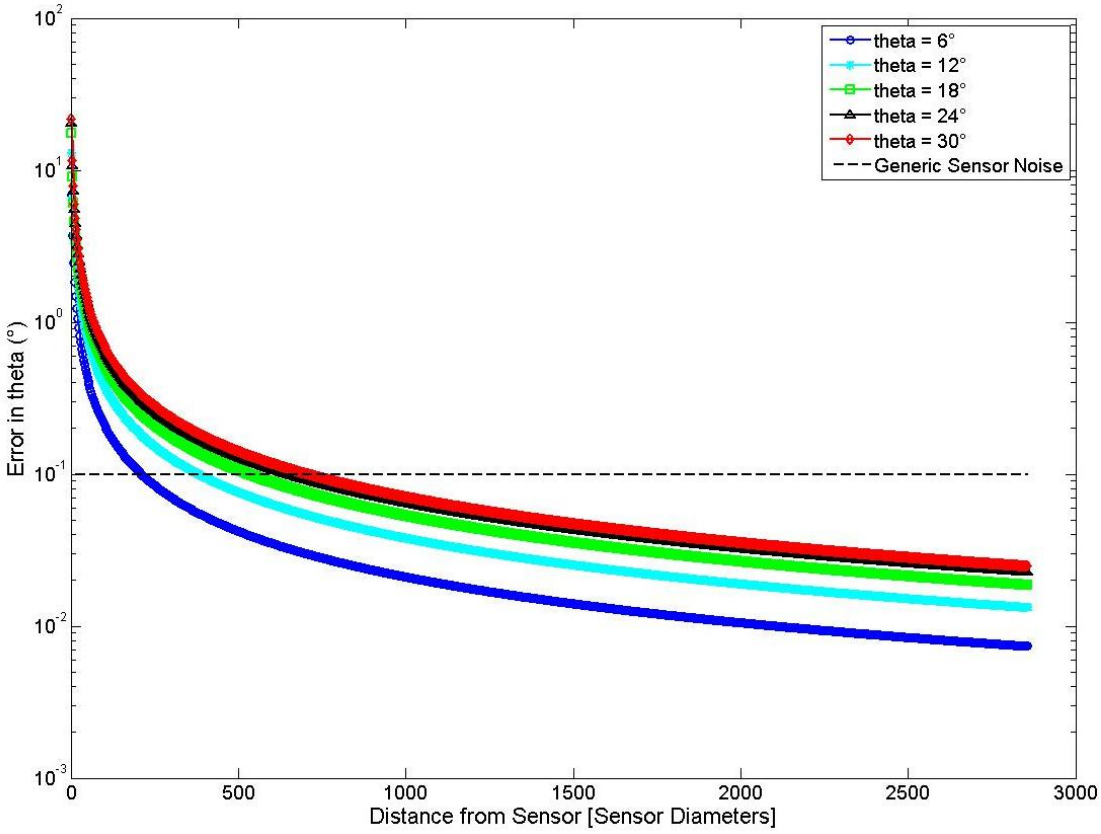

Figure 23 Combined errors in angle ($\delta\theta$) due to all three near-field effects, α = 30°.

When all three near-field effects are added and plotted together, the magnitudes of the errors are greater than the expected noise for all cases by approximately 210 sensor diameters. A close-up of Figure 23 is shown in Figure 24.

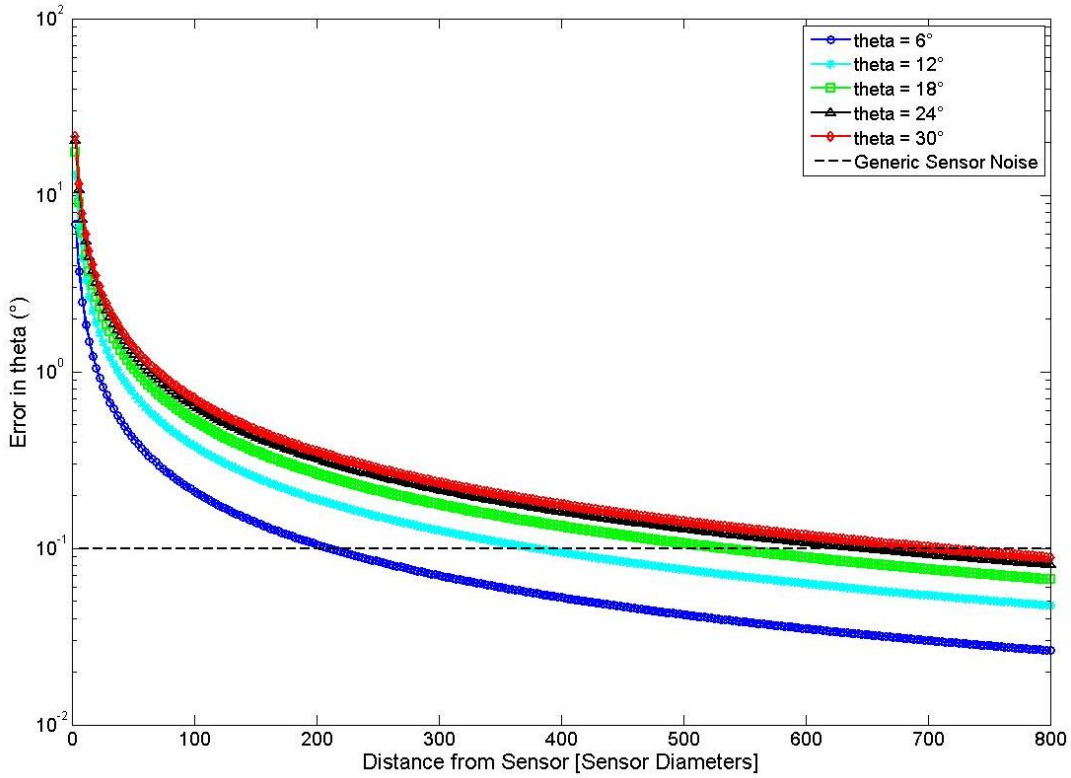

Figure 24 Close-up of the magnitudes of the three near-field effects combined.

Near-field Error Analysis

It is clear from Figure 24 that the expected errors in the near-field are greater than the expected noise level for a CSS by the time the beacon is located approximately 210 sensor diameters from the sensor. Additionally, the errors begin to change in magnitude rapidly by the time the beacon is separated from the sensor by approximately twenty inches. For an ARD mission in which one chaser spacecraft is coming in to dock with a target spacecraft, it will be important to accurately account for the near-field errors, especially in the final approach maneuver when the docking mechanism is being aligned and engaged. A failed relative attitude solution at that short range could have catastrophic effects for mission success.

Fortunately, the proximity and uniform intensity errors are additive and have errors in the angles that lead to the target seeming closer than it really is. The non-uniform light source errors can be additive or not depending on the orientation of the beacon, but they have the smallest magnitudes and will therefore never make the estimate of the target's position farther than it really is. If the algorithm used to estimate the target's position yields a solution, the solution will err on the side of caution.

The errors in the angle ($\delta\theta$) due to near-field effects are not large enough to negate the use of a CSS for proximity operations. For many applications (i.e. inspection missions, formation flying, etc), the chaser and target spacecraft do not have to dock and may never get close enough to each other for near-field errors to matter.

Characterization Test Apparatus (CTA)

In order to utilize a CSS for close-proximity relative navigational solutions during docking operations, the magnitude of the total error as the chaser approaches the target must be determined and accounted for, especially as the errors are changing rapidly. In order to determine what these errors truly are and validate the analysis above, a test bed capable of accurately moving beacons (or conversely a CSS) to known positions over these critical dimensions is required.

This thesis proposes a Characterization Test Apparatus (CTA) composed of two one-quarter inch aluminum plates separated from each other by four threaded steel rods, nuts, and washers (Figure 25). On the bottom aluminum plate is mounted a CSS in a known position. The top aluminum plate has an array of beacons mounted in known positions. The top aluminum plate can be adjusted up and down using four nuts (one on

each steel rod). The CSS and the array will be connected via serial cables to a CPU running Matlab.

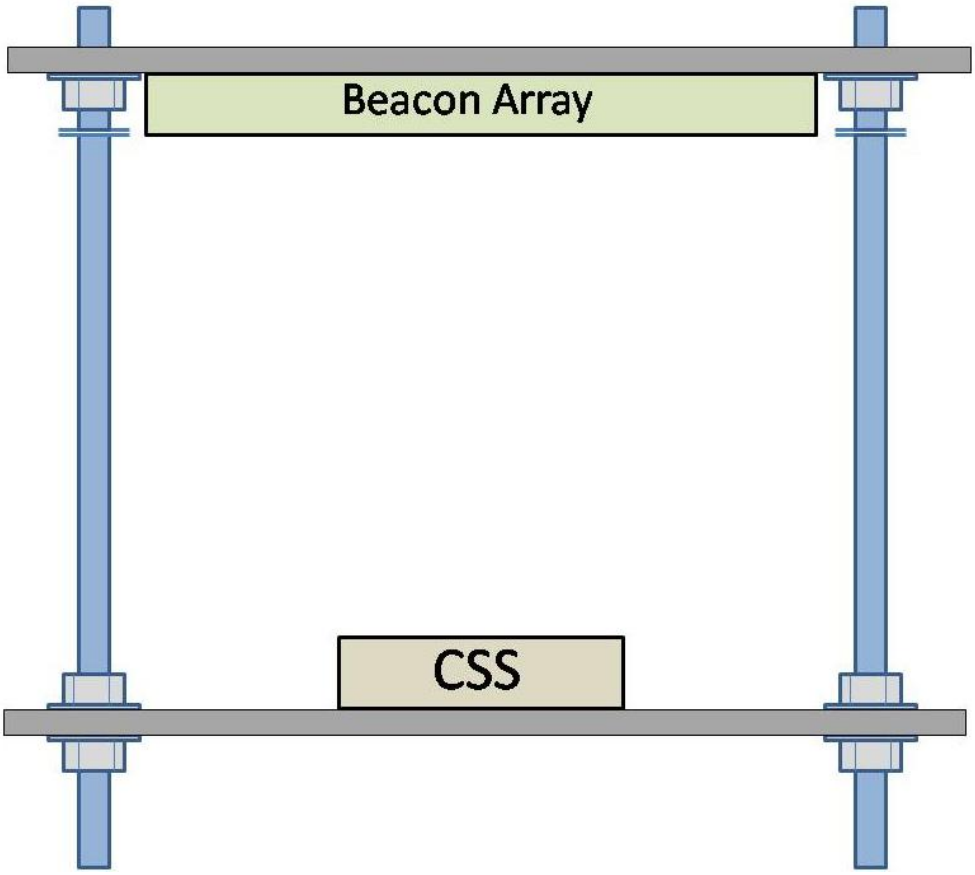

Figure 25 CTA illustration, not to scale.

The maximum separation distance between the two plates depends on the length of the steel rods, but the plate with the beacon array is able to move through the entire range of distances from zero inches out to the maximum allowed by the steel rods. A more detailed description of the CTA design is presented in Chapter IV.

In order to probe the magnitudes of the near-field errors, the location of each beacon with respect to the CSS must have an uncertainty small enough that the error in

the angle ($\delta\theta$) due to this CTA uncertainty is small compared to the error due to the near-field effects. Several uncertainty contours are plotted against the total error due to all near-field effects (Figure 23) in order to get a feel for how accurately the CTA uncertainty must be known. The uncertainty contours were calculated assuming the uncertainties were in the direction causing the maximum possible error in the angle (i.e. orthogonal to the vector, see Figure 26). The result is shown in Figure 27.

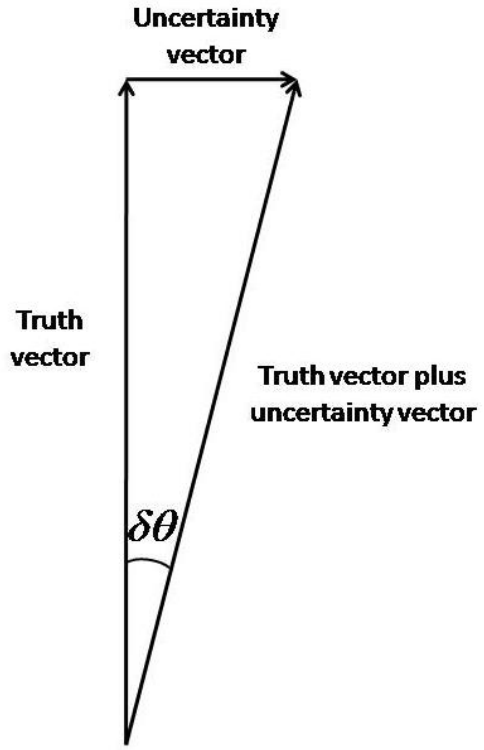

Figure 26 Uncertainty contours calculated assuming all the uncertainty is orthogonal to the true vector.

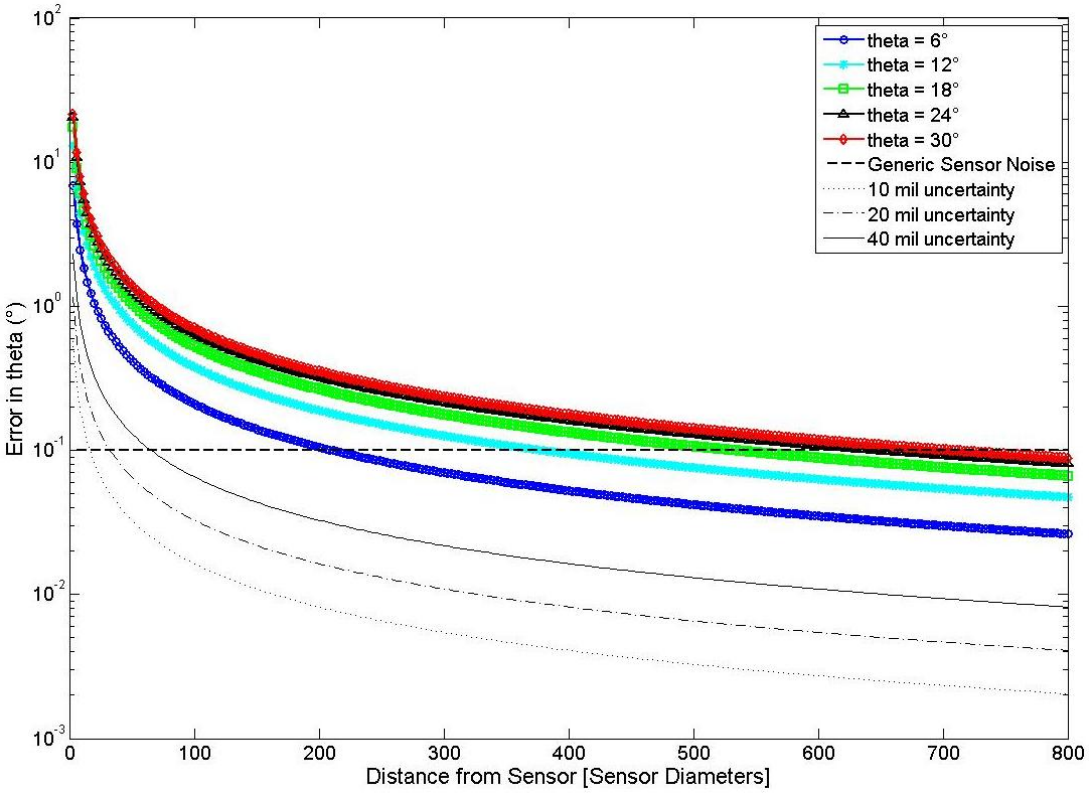

Figure 27 CTA uncertainty contours plotted with near-field effects.

All of the uncertainties in Figure 27 are less than the error due to the near-field effects when the beacon is off boresight by 6°. However, the CTA's ability to resolve the near-field effects increase as the ratio between the magnitude of the near-field effects and the uncertainty due to the CTA increases. This means that the smaller the uncertainty in the angle due to the CTA, the better the near-field effects can be resolved. Obviously, the closer to zero uncertainty the CTA is, the better the resolution. However, at some point it becomes cost prohibitive to reduce the uncertainty any farther. During the design of the CTA, it is desired to keep the uncertainties due to the CTA itself at least one order of magnitude less than the near-field effects.

CHAPTER III

NORTHSTAR$_{TM}$ SENSOR

Having proposed a test bed for use in quantifying the near-field errors associated with using a CSS in close-proximity, it is necessary to select a sensor for testing in the CTA. The NorthStar$_{TM}$ sensor was chosen for the following reasons:

1. *Cost and Availability* – The NorthStar$_{TM}$ sensor is manufactured and distributed by Evolution Robotics, and AggieSat Lab already has access to a NorthStar$_{TM}$ sensor development kit. Additional units are available (at low cost) by purchasing the Rovio robots and then removing the NorthStar$_{TM}$ sensor.
2. *Mass, volume, and power* – Due to strict mass and volume constraints placed on small satellites (which are usually launched as secondary payloads), components must be low mass and low volume in order to maximize the resources remaining on the satellite to perform meaningful science and/or technology demonstrations. Additionally, low volume for a spacecraft typically translates to less surface area available for solar panels, constraining small satellite components to being generally low power devices. The NorthStar$_{TM}$ sensor, with advertised dimensions of 3cm x 4cm x 1cm [1.2" x 1.6" x 0.4"] and a mass of approximately 13 grams [11] is an attractive candidate. Based on measurements performed at AggieSat Lab, a combined NorthStar$_{TM}$ sensor/microprocessor combination (utilizing the STM32F103ZET6 microprocessor) consistently draws approximately 80 milliamps of current at a voltage of 3.3V.

3. *Designed to provide a three-degree-of-freedom (3-dof) solution* – The NorthStar$_{TM}$ sensor is currently used in the Rovio$_{TM}$ and Mint$_{TM}$ robots[9] to provide a 3-dof solution locating the robot's position and angle on the floor. The NorthStar$_{TM}$ sensor hardware has already been engineered and tested for use in a 3-dof localization system. Choosing the NorthStar$_{TM}$ sensor for use in the CTA saves AggieSat Lab time and money in developing its own CSS at the expense of having to model a "black box" and use the NorthStar$_{TM}$ sensor's outputs to generate a 6-dof relative attitude solution.
4. *6-dof localization potential* – Researchers at the Land, Air, and Space Robotics (LASR) Lab at Texas A&M University performed testing on the NorthStar$_{TM}$ sensor to determine its suitability for use as part of a 6-dof localization system [12]. They sampled the NorthStar$_{TM}$ measurement noise versus light intensity at various angles and distances, then created a model for estimating how well the NorthStar$_{TM}$ sensor would perform as a vision-based 6-dof localization system. While they conclude that the NorthStar$_{TM}$ sensor promises to be an effective 6-dof localization system, they note that the NorthStar$_{TM}$ sensor could function as a relative position sensor when performing close-proximity operations.

NorthStar$_{TM}$ Sensor Overview

The NorthStar$_{TM}$ sensor is a localization technology manufactured and distributed by Evolution Robotics$_{®}$. The sensor, shown in Figure 28, is packaged inside a protective plastic cover that includes an infrared (IR) window and provides some

[9] See Evolution Robotics webpage, http://www.evolution.com/, [retrieved June 2010].

protection from electrostatic discharge [11]. The NorthStar$_{TM}$ sensor has four photovoltaic (PV) cells arranged in a pyramid configuration seen just off-center when viewed from above. These four cells are arranged like a pyramidal coarse sun sensor of the cosine-type described in Chapter II.

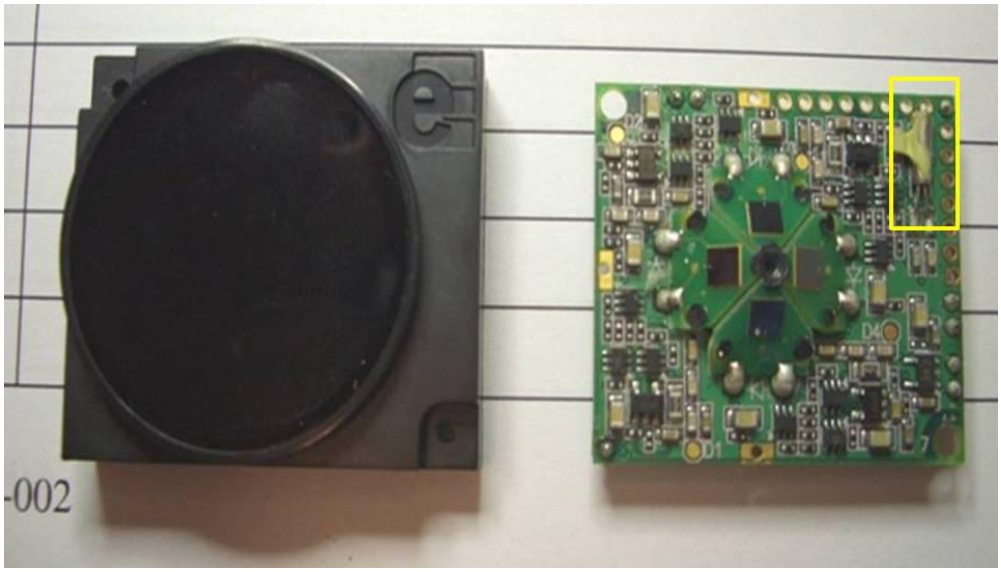

Figure 28 Top view of the NorthStar$_{TM}$ plastic IR cover (left) and the sensor head (right).

The NorthStar$_{TM}$ sensor was designed for terrestrial use, meaning the components used to fabricate the sensor are not required to be proven in a space environment. In order to determine its suitability for use in an ARD demonstration, environmental testing on the NorthStar$_{TM}$ sensor would need to be performed to show the sensor could withstand launch loads and the space environment (including radiation, thermal cycling, vacuum, etc). An inspection of the top (Figure 28) and bottom (Figure 29) of the NorthStar$_{TM}$ sensor reveals components which (excluding the PV cells) could be potted to protect them from outgassing when exposed to the hard vacuum of space.

In the upper right corner on the top side of the sensor is a cylindrical metal canister (covered in a staking compound) which must be identified to determine its suitability for space (see boxed component in Figure 28). Additionally, the materials making up the plastic casing and IR window will need to be identified and either confirmed as low outgassing materials or replaced with some other casing. There appear, however, to be no immediate show-stoppers which negate the NorthStar$_{TM}$ sensor as a potential candidate for a space-based close-proximity relative attitude sensor.

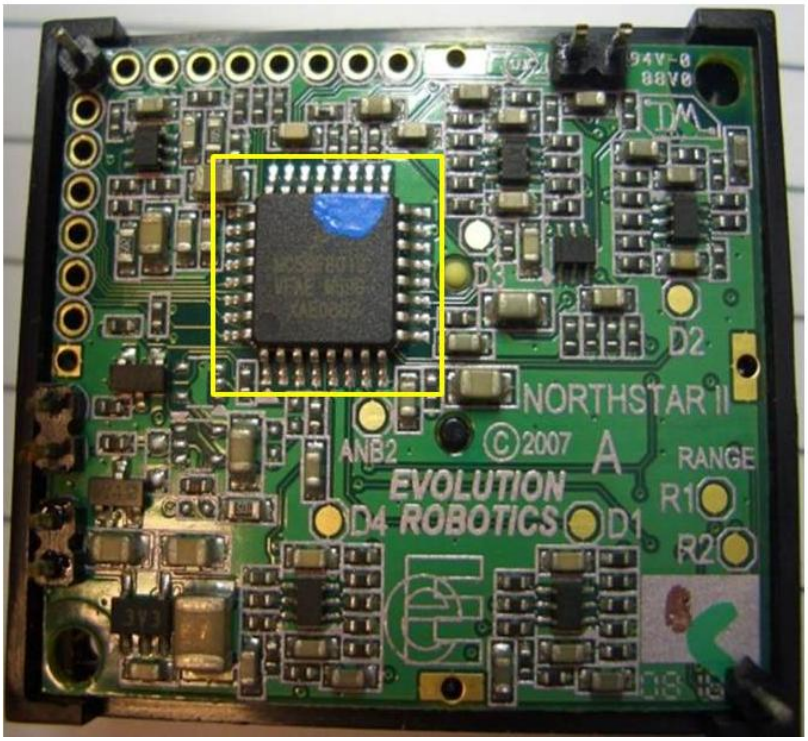

Figure 29 Bottom of NorthStar$_{TM}$ sensor.

A look at the bottom of the NorthStar$_{TM}$ sensor reveals a Freescale Semiconductor 56F8013 digital signal controller as the major component (see boxed component in Figure 29). This part has Digital Signal Processing (DSP) functionality

and two 3-channel 12-bit analog-to-digital converters (ADCs) [13] which together (DSP and ADCs) would allow the NorthStar$_{TM}$ sensor to take analog measurements from the PV cells and convert those to digital signals to be passed from the NorthStar$_{TM}$ sensor.

Designed to be an IR based 3-dof localization system, the NorthStar$_{TM}$ sensor (detector) tracks the position of IR light spots projected onto some surface in the environment or directly tracks the position of light sources [11]. The detector is able to determine the relative positions of each of the light sources projected onto the plane of the detector in the detector coordinate system (a planar coordinate system with the detector at the origin). By assuming that the detector coordinate plane is always oriented parallel to the floor, the detector is able to provide a 3-dof solution (X-Y position and an angle) which can be used to navigate about the floor. The NorthStar$_{TM}$ sensor is already utilized in this manner by the Rovio robot, which uses the output from the NorthStar$_{TM}$ sensor to navigate around a room by viewing light spots on the ceiling.

The NorthStar$_{TM}$ sensor itself contains PV cells which detect incoming IR light modulated at pre-defined frequencies and generate signals which are converted by the sensor into an X-Y position locating the light source in the Detector coordinate system [11]. Modulating the IR light at known frequencies allows the signal to be more easily distinguished from the ambient IR background. The X and Y values are then returned from the NorthStar$_{TM}$ sensor as dimensionless 16-bit signed integers {-32,768 to 32,768}.

CHAPTER IV

CHARACTERIZATION TEST APPARATUS (CTA) DESIGN AND UNCERTAINTY ANALYSIS

As described previously, in order to characterize a CSS (specifically the NorthStar$_{TM}$ sensor) in the near-field, a testing apparatus is required complete with measurement instruments and an uncertainty analysis. The following sections will describe the engineering of the CTA and present the uncertainty analysis associated with the CTA design and choices of measurement instrumentation.

Characterization Test Apparatus Design Requirements

Before designing the CTA, a list of requirements it must satisfy were determined. These requirements were derived based on the results from the expected near-field error models described in Chapter II, physical dimension constraints based on available lab space, and cost constraints. The requirements and constraints were traded with the requirement to obtain meaningful data and the "desirement" that the CTA be re-useable for future testing.

Uncertainty requirements

In order to probe the errors in angle ($\delta\theta$) due to near-field effects, the beacon locations with respect to the NorthStar$_{TM}$ sensor must be known with a relatively small uncertainty. Ideally, the errors due to the uncertainty in the CTA would be in the noise so any observed errors will be near-field errors. Figure 27 showed the uncertainty

contours in the apparatus plotted against the expected magnitude of the combined-near-field errors. The CTA is required to have a small enough uncertainty that the combined near-field effects can be resolved.

Quasi-continuous adjustment from zero to twenty inches

As shown in Figure 23, the errors in angle begin to change rapidly at a separation distance of approximately twenty inches, and the changes continue to accelerate as the beacon gets closer to the sensor. More measurements and smaller step sizes are required to determine the shape of the error plot when the slope begins to change rapidly. The CTA, therefore, is required to have the ability to be adjusted very finely over those distances (0-20 inches).

CTA must fit in the lab

The physical dimensions of the CTA are constrained to reasonably fit within the lab area available for testing. Due to the large fields of view which CSSs have, the size of any array of beacons which tests the entire field of view of such a sensor increases dramatically with separation distance. The NorthStar$_{TM}$ sensor, for example, has a 120° field of view (FOV). An array of beacons would have to cover an approximately nine square foot area in order to cover the entire (FOV) at thirty inches separation distance. Tradeoffs between beacon array size and FOV coverage are required.

Cost-effectiveness

The CTA and any required measurement instruments must be designed, fabricated, and/or acquired for less than the limited budget for this project.

Autonomy in data collection

The CTA design must provide some level of autonomy in data collection. The less the user is required to handle the CTA in any way to obtain the data, the fewer opportunities for introducing systemic errors (in the form of observer biases) into the system. Additionally, if the data can be taken autonomously, the user does not have to be continuously present in order for data collection to continue. A simple script telling the CTA what actions to perform and the order in which to perform those actions may be all that is required.

CTA Design

Aluminum mounting plates and structural members

As a result of the constraint on the size of the CTA, a compromise between the portion of the field of view characterized and the CTA dimensions was required. Recalling that the proposed end use of this sensor is to be the keystone in a close-proximity relative navigation system, two key assumptions were made. The first is that the two spacecraft involved in the close-proximity operations would have some other type of system which will allow the two spacecraft to know where the other is when they are far apart (e.g. GPS and communications). In a chaser/target situation where the target is stationary and contains the beacons, the chaser is able to orient the face containing the NorthStar$_{TM}$ sensor towards the target because the chaser will know where the target is located.

The next assumption is that the chaser spacecraft in the example above will have a control law such that it attempts to keep the target on the boresight of the NorthStar$_{TM}$

sensor. As the chaser approaches the target from far away, there will be a point at which the NorthStar$_{TM}$ sensor itself is able to detect the beacons from the target vehicle and determine the direction to the target. While the initial errors in the light vector may be large because the beacon signal is weak and/or the beacons are well off boresight, the chaser vehicle's controller will reorient the chaser such that the angle to the beacons is close to the boresight of the NorthStar$_{TM}$ sensor, reducing the errors caused by near-field effects. Additionally, as the chaser approaches the target vehicle, the beacon signals will get stronger because the intensity of the light reaching the NorthStar$_{TM}$ sensor is increasing.

With these two assumptions, the CTA was limited to a twenty-four inch square cross-sectional area available for mounting beacons. The majority of this area can be covered by beacons, and the end result is the NorthStar$_{TM}$ sensor can be characterized for up to approximately twenty degrees off of its boresight at thirty inches and its entire FOV at around ten inches.

The mounting plates are aluminum and are one-quarter inch in thickness. The plates include holes for mounting beacon arrays and the NorthStar$_{TM}$ sensor, alignment holes to ensure the two plates are aligned properly, and holes for the stainless steel rods (refer to Figure 25 for an illustration). Since the stainless steel rods are threaded, the aluminum mounting plates are only limited in their ability to move up and down by the length of the rods. For the CTA, the rods are one-half inch in diameter and thirty-six inches long. The rod diameter provides stability for the top plate and the rod length allows the CTA to move the beacons over the required zero to twenty inches.

Beacon array design

The mounting plates have room for a beacon array covering up to four square feet of surface area. Each beacon needs to be located in a known position, however, and must also have access to power, a frequency driver (to modulate the light at one of the NorthStar$_{TM}$ sensor's prescribed frequencies), and the ability to turn on and off when commanded. These needs are most easily met by placing the beacons on a printed circuit board (PCB) designed to accommodate the power, frequency, and duty cycle needs of the beacon.

A 12x12 inch beacon array was designed using the EAGLE software package, a package used for generating electrical schematics and performing PCB layouts. It was decided to create a beacon array which was only one square foot instead of two square feet for a couple of reasons. The first reason was that a two square foot board is larger than any standard size and would therefore need to be custom made, increasing the cost of the part. The second reason was because a two square foot PCB is so large, finding a PCB fabrication company with tools capable of creating such a board would be difficult. However, a one square foot PCB can be handled using standard tools and techniques without any custom pricing.

The decision was made to fabricate multiple one square foot beacon arrays and have the capability to mount them such that as much of the two square foot surface area as possible was utilized. The beacon array consists of a ten inch square grid with one hundred LEDs serving as beacons (see Table 1, Figure 30, and Figure 31). In support of the ten inch square grid of LEDs, the beacon array contains a microprocessor with

enough general input/output pins (GPIO) to control each LED individually. The GPIO pin for each LED is able to toggle a MOSFET connected to the LED in order to turn the LED on or off. Power is supplied to the PCB via an AC adapter which provides 3.3V and up to 1.2 amps. In order to protect the AC adapter from possible shorts, the PCB is fused with a one amp fuse.

Table 1 Beacon array major component list. Part number refers to Figure 30 and Figure 31.

Number	Part	Description
1	DB-9 serial connector	Allows communication between the array and a CPU
2	Fuse	1 Amp rating
3	Power jack connector	Connector for AC adapter
4	RS-232 converter	Transforms TTL level signals to RS-232 signals
5	STM32F103ZET6	ARM microprocessor
6	JTAG header	Allows embedded programming of the microprocessor
7	VSML 3710	IR LED beacon
8	Slide switch	Controls the power output of the LED
9	N-channel MOSFET	Switches the LED on and off

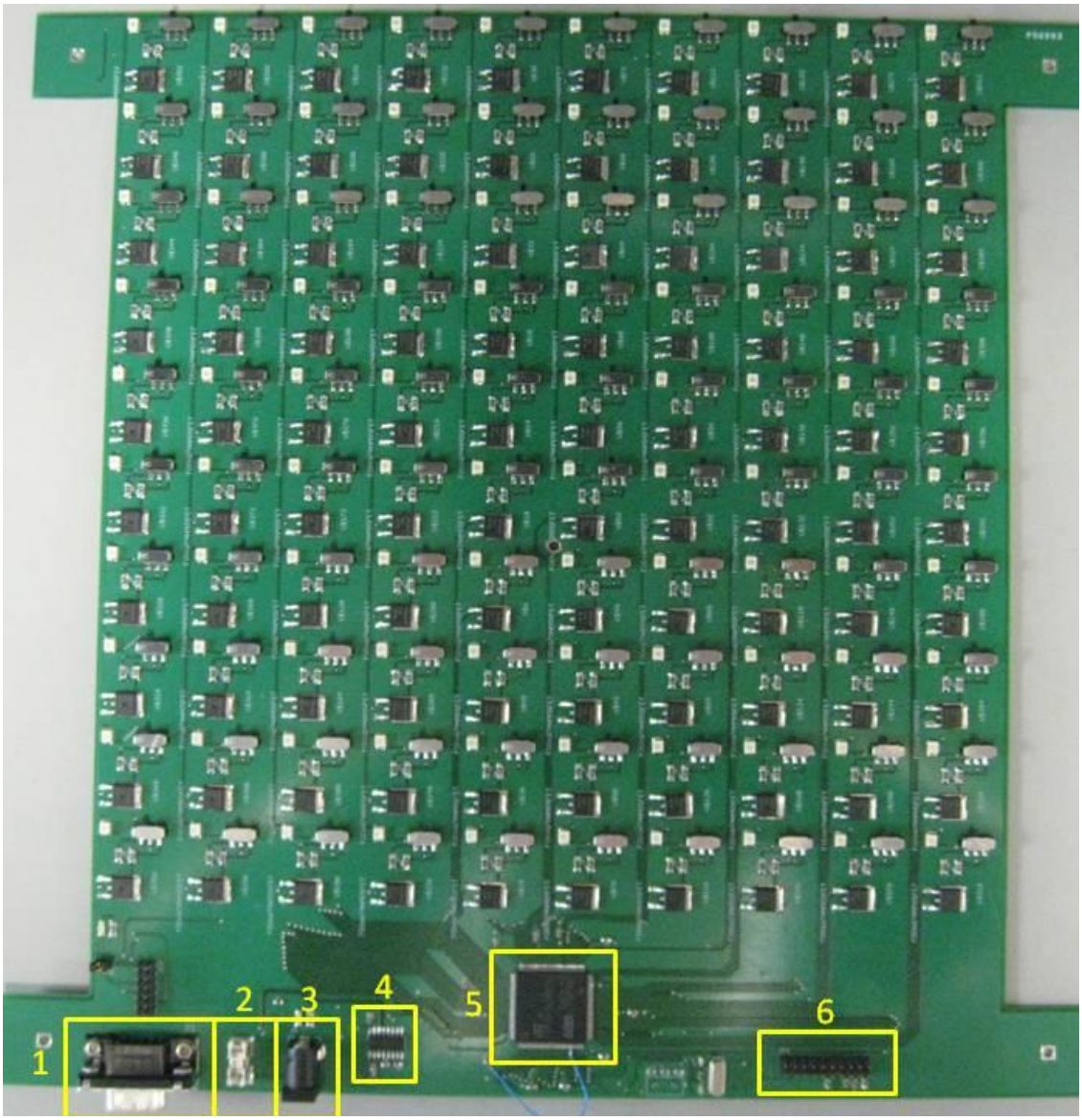

Figure 30 Beacon array with major components highlighted.

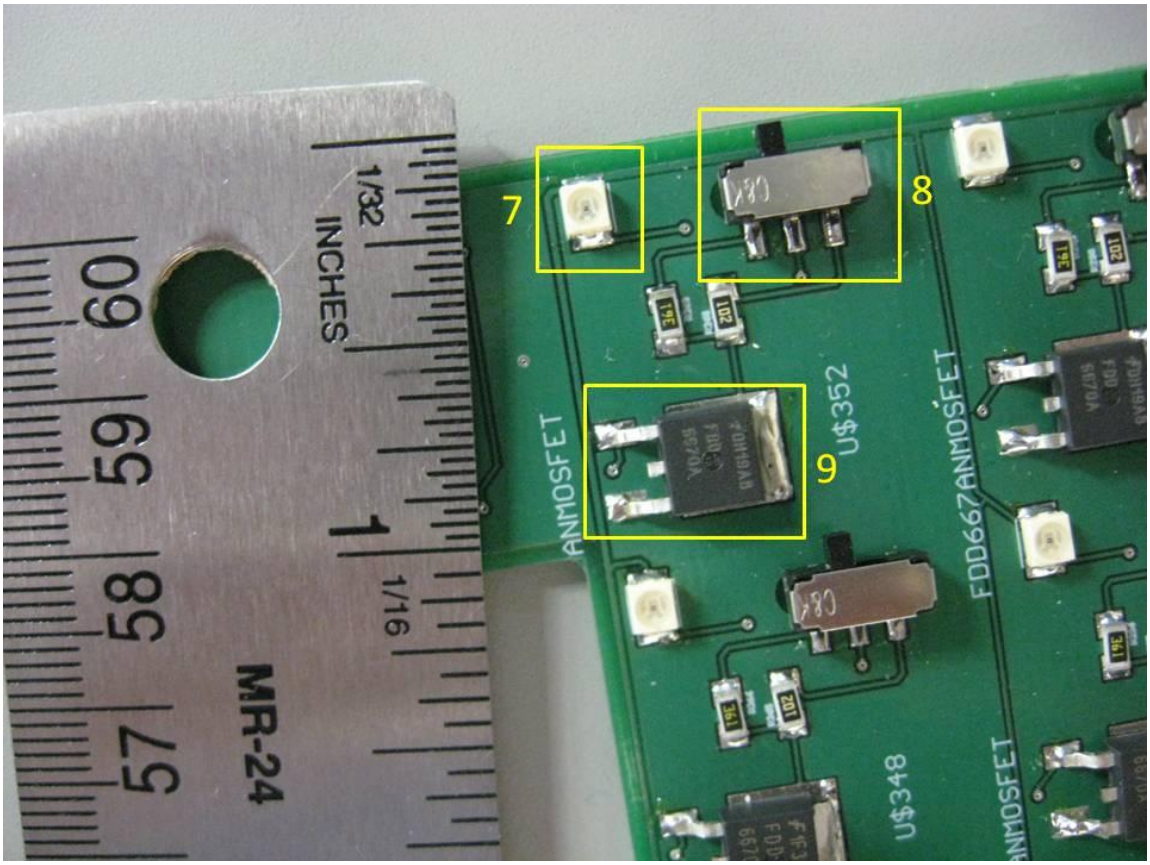

Figure 31 Close-up of one of the one-inch cells which make up the 10 x 10 inch grid.

A serial connector allows the user to communicate with the beacon array via a serial port on a CPU, making it possible to command the microprocessor to toggle any of the beacons on the grid. The array also contains a JTAG connector which allows the microprocessor to be reprogrammed while embedded on the array. The custom embedded software gives the microprocessor the ability to toggle any beacon on the grid at one of ten preset NorthStar$_{TM}$ sensor frequencies, allowing multiple frequencies to be on the PCB at the same time. If desired, the microprocessor can also toggle the same beacon at multiple frequencies at one time.

The beacon array(s) are attached to the mounting plate at five points using #4-40 standoffs and #4-40 fasteners. The mounting plate has a hole pattern which allows one beacon array to be mounted in the center of the plate or four beacon arrays to be mounted in the four quadrants of the plate (see Figure 32 and Figure 33). The beacon arrays are notched on the sides so that when four are mounted on the plate at one time, there is space to pass the steel bars through.

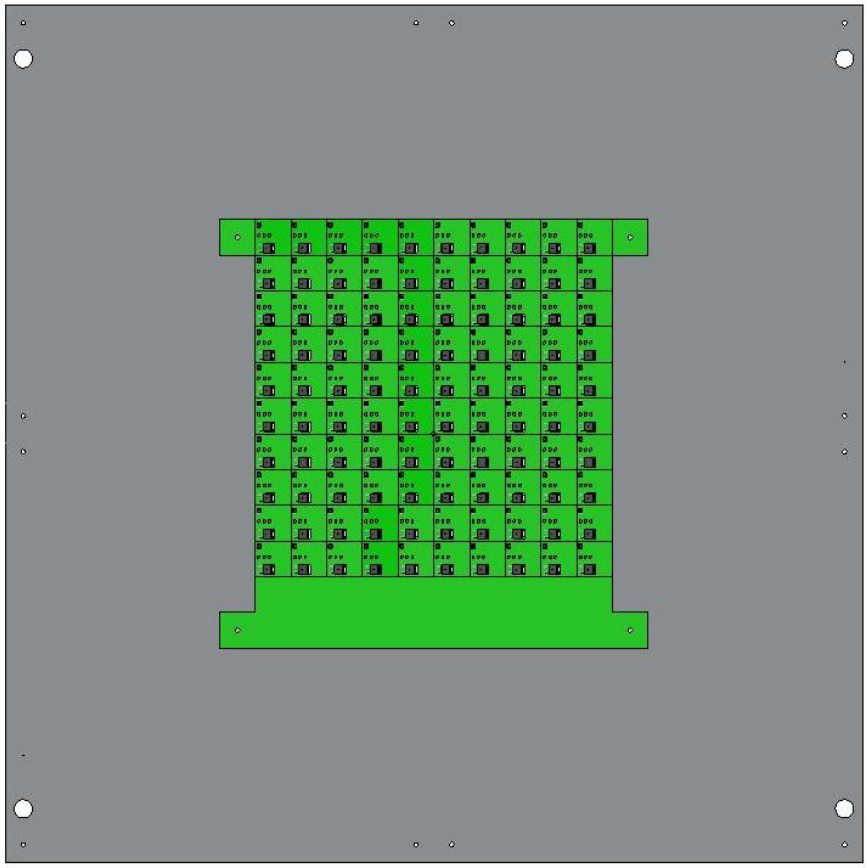

Figure 32 Single beacon array configuration.

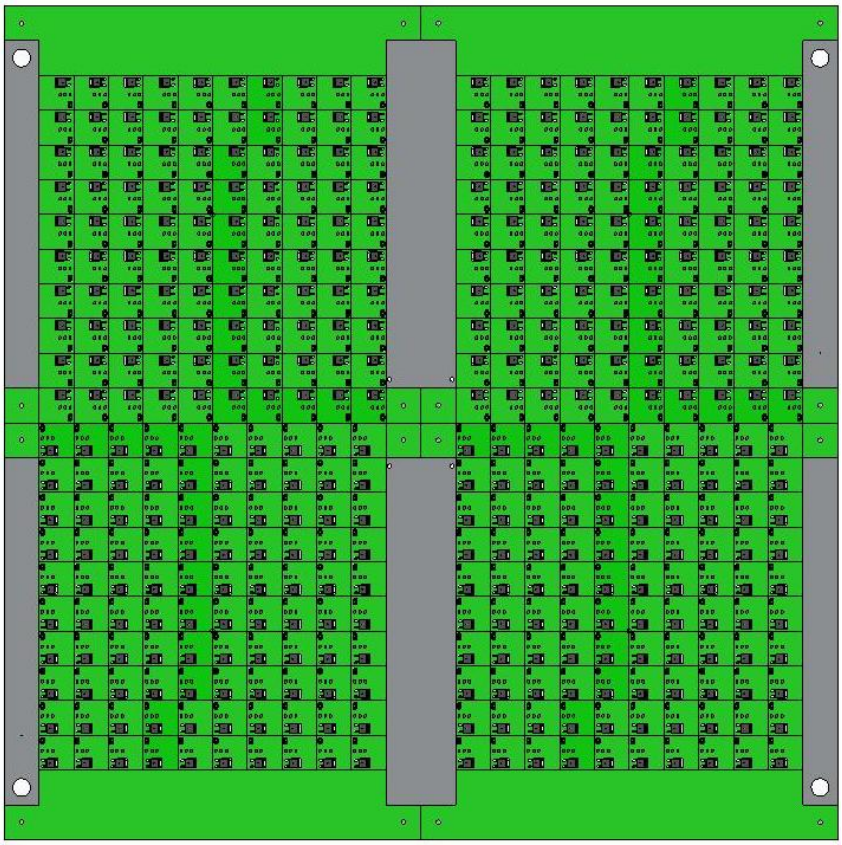

Figure 33 Four beacon array configuration.

NorthStar$_{TM}$ sensor board

The NorthStar$_{TM}$ sensor is not meant to be a stand-alone system [11]. Instead, it is meant to provide a 3-dof solution to whatever system into which it is incorporated. It was necessary, therefore, to design another PCB using the EAGLE software package. This PCB, dubbed the NorthStar$_{TM}$ sensor board, includes mounting holes for integrating a NorthStar$_{TM}$ sensor. It also contains an ARM microprocessor (STM32F103X8) which commands the NorthStar$_{TM}$ sensor, retrieves measurements from the sensor, and is able to pass those measurements to a CPU via a serial communications port. The user is able

to send commands to the microprocessor and/or the NorthStar$_{TM}$ sensor over the serial communications line, as well.

Beacon selection

The NorthStar$_{TM}$ sensor is able to detect IR light modulated at prescribed frequencies and has peak sensitivity to light with a wavelength of 950 nm [11]. Five candidate LEDs were selected which have peak emittance near 950 nm. Each of the LEDs was then supplied with power and a switching signal set at one of the NorthStar$_{TM}$ sensor prescribed frequencies. The LEDs were fixed closely to each other and then set at specified distances from the NorthStar$_{TM}$ sensor, aligned approximately along the NorthStar$_{TM}$ sensor boresight as seen in Figure 34.

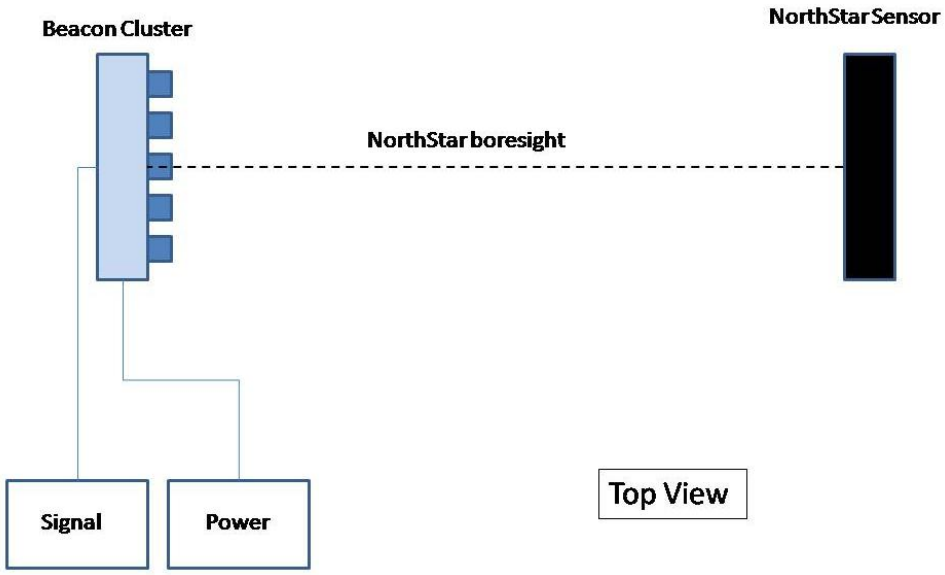

Figure 34 Illustration of LED test setup.

The goal of this test was to select an LED that performed well (i.e. good intensity values) over a wide range of distances from the NorthStar$_{TM}$ sensor. The intensity of the

light output by each LED is a function of the forward current through the LED and the supply voltage. The supply voltage was fixed at 3.3V, the nominal supply voltage for the selected microprocessor. Changing the forward current required the selection of different resistor values. Four separate forward current values were studied: ten milliamps, twenty milliamps, fifty milliamps, and one hundred milliamps.

Note that there was no hard requirement on the distance accuracy as this test was only supposed to yield an order of magnitude comparison of the different LEDs in order to down-select from five LED options to one candidate LED. The distances were measured with a twenty-four inch ruler with one sixteenth inch gradations. Angle off of boresight was determined by eye.

None of the LEDs worked well for the entire range required by the CTA. When the forward current was small, the intensity dropped off too much out at the upper range of the CTA to yield solid measurements. For larger forward currents, the intensity at the outer ranges was good, but the LEDs would saturate the NorthStar$_{TM}$ sensor as they moved in closer. Based on this finding, it was decided to include a switch into the beacon design that allowed the user to switch the resistance values (and therefore the forward current) depending on the location of the LEDs.

The VSML3710 LED from Vishay® was selected as the LED for use in the CTA. It exhibited good performance over the desired range, but is also scalable for use at greater distances if the CTA is ever modified to extend its range. It is also packaged in a PLCC-2 case which is easier to solder than two of the other LEDs in smaller packages. Upon down-selecting to the VSML3710, additional tests (not reported) were performed

to select two appropriate resistors that would allow the VSML3710 to work over the range of interest. The larger resistor, 1 kΩ, was chosen for distances out to ten inches, and the smaller resistor, 360 Ω, was chosen for distances from ten inches out to thirty inches.

Uncertainty Analysis

In order to determine the errors in the angle ($\delta\theta$) due to the CTA, it is required to perform an uncertainty analysis on the CTA to ascertain the uncertainty in the vectors to each of the beacons. Due to the fact that the manufacturing tolerances on the NorthStar$_{TM}$ sensor are unknown, this analysis will determine the uncertainty in the vectors going from the center of the bottom surface of the NorthStar$_{TM}$ sensor board to each of the beacons. The vector from the center of the NorthStar$_{TM}$ sensor board (not the center of the NorthStar$_{TM}$ sensor head) to the detectors of the NorthStar$_{TM}$ sensor will be estimated as described in Chapter V.

Represent the vectors from the NorthStar$_{TM}$ sensor board to the ith beacon as

$$\boldsymbol{n}_i = \boldsymbol{X}_i \pm \boldsymbol{u}_i = \begin{bmatrix} X_{ideal} \\ Y_{ideal} \\ Z_{ideal} \end{bmatrix}_i \pm \begin{bmatrix} u_X \\ u_Y \\ u_Z \end{bmatrix}_i \tag{23}$$

where the vector $\boldsymbol{X_i}$ is the ideal vector from the NorthStar$_{TM}$ sensor board to the ith beacon and $\boldsymbol{u_i}$ is the uncertainty in the ith beacon. The vectors $\boldsymbol{n_i}$ are written in a coordinate frame with its origin at the center of the bottom surface of the NorthStar$_{TM}$ sensor board and oriented as shown in Figure 35.

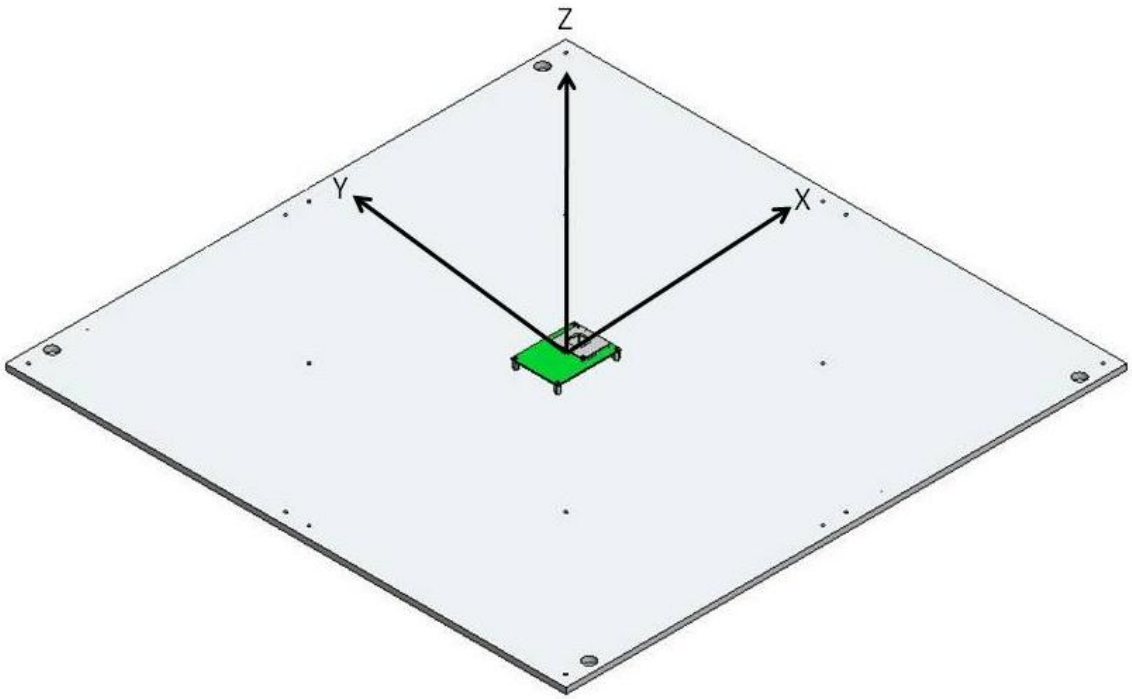

Figure 35 Coordinate system for determining uncertainties.

The uncertainties in the X, Y, and Z directions will be determined by moving from the origin to each beacon and combining the uncertainties along the way.

Hole placement on NorthStar$_{TM}$ sensor board

Beginning from the origin of the coordinate system and moving to the hole in the top left corner of the NorthStar$_{TM}$ sensor board, the first uncertainty is the uncertainty in the location of the mounting hole. The NorthStar$_{TM}$ sensor board was fabricated by Advanced Circuits, who quote a tolerance of ±5 mils for all internal features (including holes). This leads to a maximum uncertainty in the X and Y directions due to NorthStar$_{TM}$ sensor board hole tolerances of ±5 mils.

NorthStar$_{TM}$ sensor board standoffs

The NorthStar$_{TM}$ sensor board is attached to the mounting plate via standoffs whose heights will be measured prior to insertion into the mounting plate. The standoffs will be measured using calipers whose smallest divisions are 0.001 inches. The uncertainty in the standoffs (Z direction) will then be ±0.5 mils.

Hole placement on bottom mounting plate

The holes in the bottom mounting plate in which the standoffs are inserted are drilled in a CNC machine and have a specified tolerance of ±5 mils. The locations of the holes in the bottom plate have an uncertainty in the X and Y directions of ±5 mils.

Standoff mounting holes to beacon array center hole

The two mounting plates (top and bottom) are clamped together and drilled at the same time, so that both plates have the same hole pattern, and the holes are located in exactly the same place relative to each other on both plates. The uncertainty in the distance between the NorthStar$_{TM}$ sensor board standoff mounting holes and the center mounting hole for the beacon array is the same whether measured on the top plate or the bottom plate (see Figure 36).

Since the holes were machined using a CNC, and the part drawing specifies a tolerance of ±5 mils, the uncertainty in the X and Y distances between the standoff mounting holes on the bottom plate and the beacon array center hole on the top plate is ±5 mils. This uncertainty assumes the plates are perfectly mounted. Uncertainties in how the plates are mounted are covered hereafter.

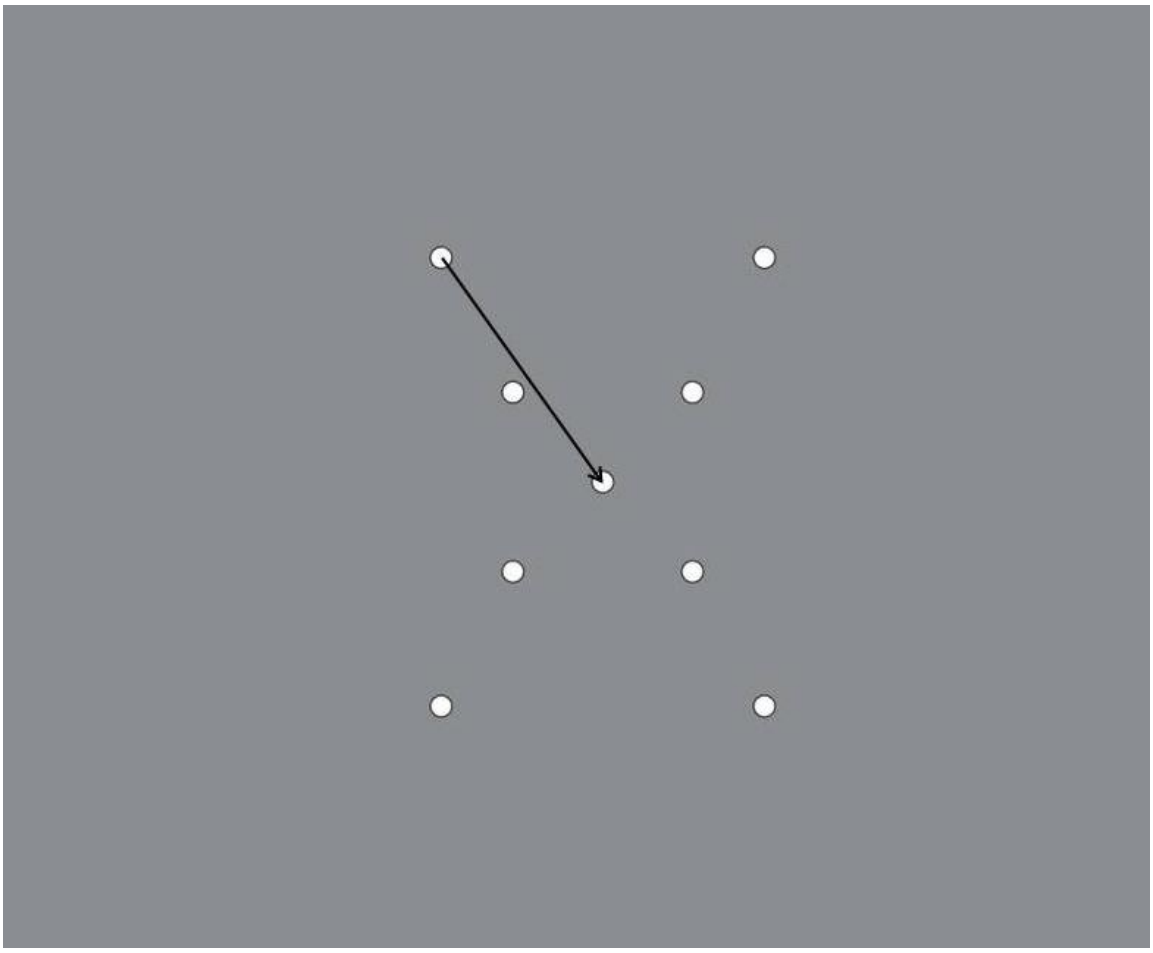

Figure 36 Distance from the NorthStar$_{TM}$ sensor board standoff mounting hole and the center mounting hole for the beacon array.

Plate levelness and separation distance

In order to make sure the plates are parallel, each plate will be leveled in the X and Y directions at the center of the plate with a precision machinist's level which has a resolution of 5 mils per foot. The distance between the two mounting plates will then be measured at four locations around the outer edges of the plates, and the measurements will be averaged to obtain the height at the center of the plate. The uncertainty in the center height will be the difference between the center height and the maximum and

minimum measurements. Since the plates were leveled using the precision machinist's level, the expected uncertainty in the Z direction is bounded by ±5 mils (5 mils/foot over one foot from the center).

Beacon array standoffs

As with the NorthStar$_{TM}$ sensor board, the beacon array will be attached to the mounting plate via standoffs. The standoffs will be measured using calipers, and the Z uncertainty in the standoff height measurement will be ±0.5 mils.

Beacon array thickness

The beacon array PCB thickness will be measured using calipers, and the Z uncertainty in the thickness measurement will be ±0.5 mils.

Location of beacon solder pads on the beacon array PCB

The pads to which the beacons will be soldered are located on the beacon array PCB with an uncertainty in X and Y of ±5 mils as quoted by the PCB manufacturer (Advanced Circuits).

Placement of beacons on solder pads

The beacons and other components on the beacon array board will be hand-soldered to the PCB, so placement of the beacons on the solder pads represents a relatively large possible uncertainty in the X and Y directions.

The beacons radiate light in a 120° cone, so assuming the beacon is placed perfectly and then rotated about its boresight, there will be no change in the light

distribution and no errors in the angle ($\delta\theta$). However, any displacement of the beacon on the pads will cause errors in the angle between the ideal vector and the true vector from the NorthStar$_{TM}$ sensor board to the beacon.

A comparison of the dimensions of the beacon and the dimensions of the solder pads results in a maximum uncertainty in the X direction of ±21 mils and a maximum uncertainty in the Y direction of ±6.5 mils. These uncertainties are the result of the becason being able to slide farther in the X-direction than the Y-direction and still remain on the solder pads (see Figure 37). In order to ensure these maximum uncertainty values, some of the solder pad must be seen on both sides of the beacon after it has been soldered, requiring an inspection by the user.

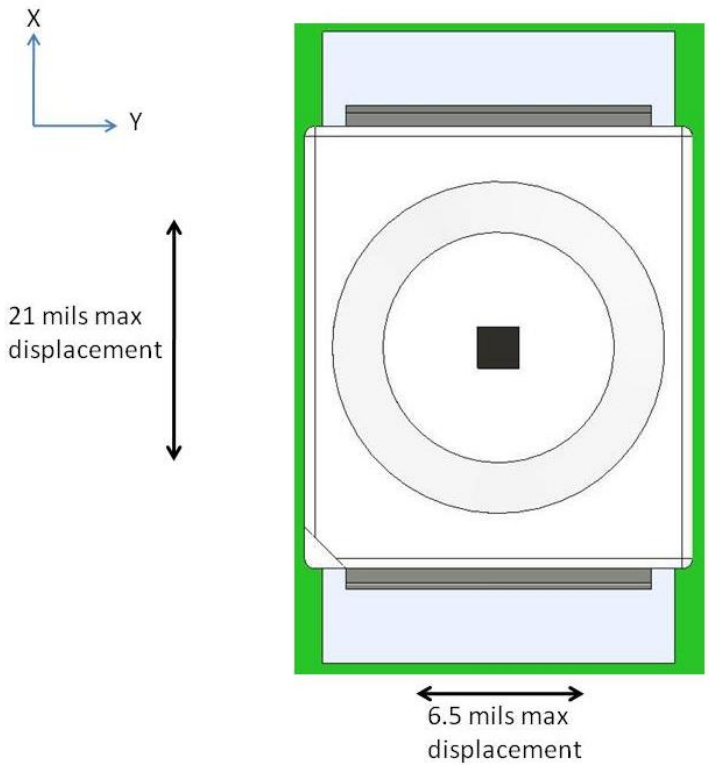

Figure 37 Illustration of a beacon (VSML3710) on its solder pads.

Distance from PCB to emitter in beacon

The distance from the bottom of the LED to the emitter is not given in the datasheet for the VSML3710. The VSML3710 is in a PLCC-2 package, however, which is a standard package type. From comparison to other PLCC-2 parts, and by inspection, the emitter is located close to the centerline (if not on the centerline) of the part. It is assumed, then, the emitter is at the centerline of the part with an uncertainty of ±1/4 of the height of the part. This equates to an uncertainty in the Z direction of ±16 mils.

Plate offset

As mentioned earlier, the two aluminum mounting plates are drilled together so that the holes in the top and bottom plates align perfectly. In addition to the holes needed for mounting the PCBs and for the steel rods, two sets of 1/32" holes are drilled in the plates to serve as alignment holes. To ensure alignment of the two plates, masses are suspended from 30 AWG wires which are threaded through the alignment holes. Several inches of the bottom sections and a small portion of the tops of the wires are stripped of insulation. Digital multimeters which are capable of performing continuity checks are connected to each wire and to one of the mounting plates (see Figure 38).

The mass serves to keep the wire taut and hanging straight down without any kinks. With the multimeter connected to the wire and to the mounting plate, the multimeter will produce an audible beep if the bottom section of the wire (which has been stripped) touches the side of the alignment hole through the mounting plate.

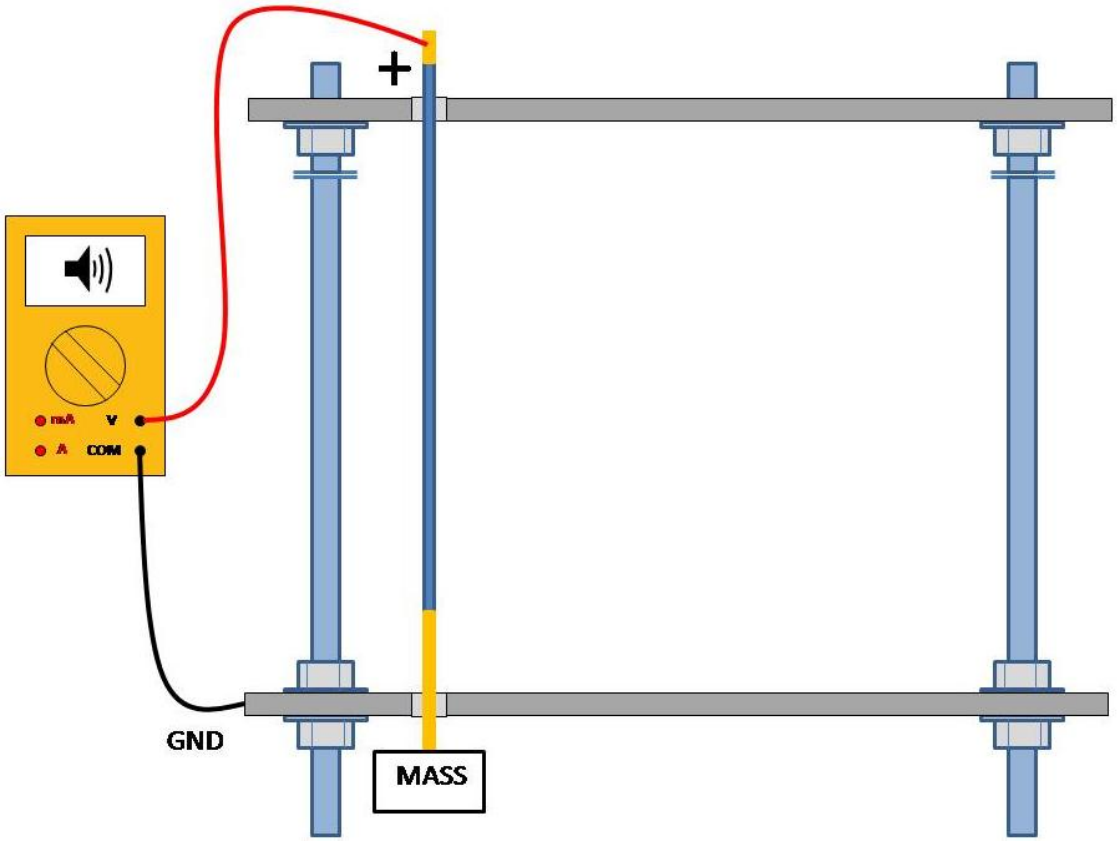

Figure 38 Continuity test setup. Only one alignment wire is shown.

To align the plates, the top plate is adjusted until there are no beeps coming from either multimeter. When the beeping stops, the wire is hanging through both the top and bottom holes without making contact with the bottom hole (the portion of the wire through the top hole is still insulated and may be touching the sides of the hole). The alignment holes are 1/32" (31.25 mils) in diameter, and the 30 AWG wire is 10 mils in diameter, so the most the holes could be offset is 21.25 mils (see Figure 39).

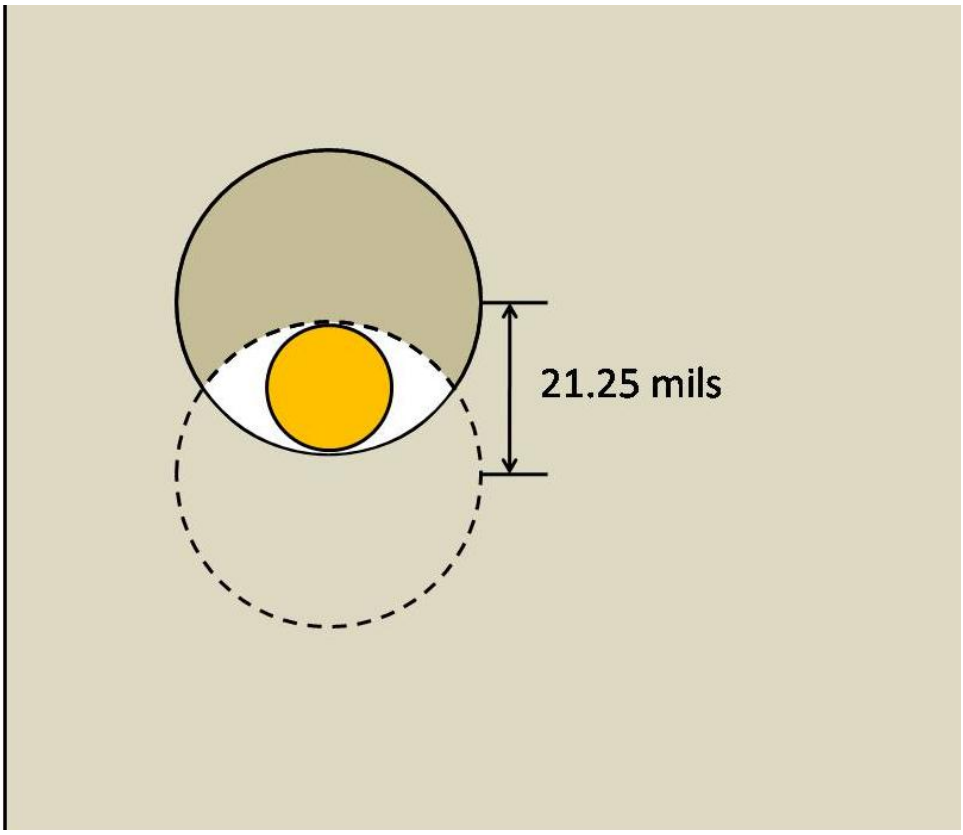

Figure 39 Top view looking down alignment hole. Maximum plate offset is 21.25 mils when the wire is not touching the bottom hole.

The worst-case uncertainty in the X and Y directions for the offset of the two plates is ±21.25 mils.

Thermal expansion of the CTA

The CTA will be set up in a lab in which the temperature is controlled and remains fairly constant. It is unlikely that the temperature will change enough to cause any significant effect in the uncertainty. To find the order of magnitude of the effect of thermal expansion on the CTA, imagine the room temperature changed by five degrees Fahrenheit over the course of a test run. The thermal expansion coefficients for

aluminum and 304 stainless steel are 12.3e-6 [in/in °F] and 9.6 [in/in °F], respectively[10]. The maximum change will be in the steel rods whose utilized length is thirty inches. This translates to a 1.4 mil error when the plate separation is thirty inches and the lab temperature changes by five degrees Fahrenheit. For shorter separation distances, the 1.4 mil error becomes smaller and smaller (a five inch separation yields less than a quarter of a mil change). In general, all the changes in length are less than one mil and are therefore insignificant compared to other uncertainties in the CTA.

Uncertainties in the X, Y, and Z directions

The uncertainties in the X, Y, and Z directions are independent of each other; therefore, the uncertainties in each direction can be calculated separately. Grouping all the X, Y, and Z measurements separately, three equations can be written.

$$\begin{aligned} X\left(x_1, x_2, \ldots, x_n\right) &= x_1 + x_2 + \ldots + x_n \\ Y\left(y_1, y_2, \ldots, y_n\right) &= y_1 + y_2 + \ldots + y_n \\ Z\left(z_1, z_2, \ldots, z_n\right) &= z_1 + z_2 + \ldots + z_n \end{aligned} \tag{24}$$

where x_1 is the first X measurement (e.g. hole placement on NorthStar$_{TM}$ sensor board), x_2 is the second X measurement (e.g. hole placement on bottom mounting plate), etc. The Y and Z terms are defined similarly.

Using the X-direction measurements as an example, the total uncertainty associated with the X-direction can be found by

$$u_X = \sqrt{\left(\frac{\partial X}{\partial x_1}u_1\right)^2 + \left(\frac{\partial X}{\partial x_2}u_2\right)^2 + \ldots + \left(\frac{\partial X}{\partial x_n}u_n\right)^2} \tag{25}$$

[10] See "Coefficients of Linear Expansion," http://www.engineeringtoolbox.com/linear-expansion-coefficients-d_95.html, [retrieved June 2010].

where u_X represents the total uncertainty associated with the X-direction and u_1-u_n are the uncertainties associated with measurements x_1-x_n, respectively. Inspection of the X-equation in (24) shows that the partial derivative of X with respect to all the individual measurements is equal to one. Equation (25) can therefore be reduced to

$$u_X = \sqrt{u_1^{\,2} + u_2^{\,2} + \ldots + u_n^{\,2}} \tag{26}$$

where the u_n's represent each of the individual uncertainties in the X direction. The equations for u_Y and u_Z are similar.

Each of the uncertainties covered in this chapter were combined in a table, and the total uncertainty in each direction was calculated using equation (26). The results are shown in Table 2.

Table 2 Uncertainties in the X, Y, and Z directions

Item	X (mils)		Y (mils)		Z (mils)	
	+	-	+	-	+	-
NS sensor board hole placement	5.0	5.0	5.0	5.0	0.0	0.0
NS standoff height	0.0	0.0	0.0	0.0	0.5	0.5
Plate hole locations	5.0	5.0	5.0	5.0	0.0	0.0
Plate levelness	0.0	0.0	0.0	0.0	5.0	5.0
Plate offset	21.3	21.3	21.3	21.3	0.0	0.0
Plate separation distance	0.0	0.0	0.0	0.0	0.5	0.5
Array stand-off height	0.0	0.0	0.0	0.0	0.5	0.5
Array board thickness	0.0	0.0	0.0	0.0	0.5	0.5
Array pad location uncertainties	5.0	5.0	5.0	5.0	0.0	0.0
Plate to array hole tolerance	5.0	5.0	5.0	5.0	0.0	0.0
Upper plate deflection	0.0	0.0	0.0	0.0	5.0	5.0
LED placement on solder pads	21.0	21.0	6.5	6.5	0.0	0.0
Light emitter placement in LED	0.0	0.0	0.0	0.0	16.0	16.0
Uncertainty	31.5	31.5	24.4	24.4	17.5	17.5

The uncertainties in the locations of the beacons now need to be translated into an uncertainty in the angle of the vector pointing from the NorthStar$_{TM}$ sensor board to each beacon.

Three-dimensional uncertainty in angle

The uncertainty in the angle ($\delta\theta$) of the vector pointing from the NorthStar$_{TM}$ sensor board to each beacon due to the uncertainties in the CTA provides a measure for how well the beacons are known and therefore how well the near-field uncertainties can be resolved. A relationship between the uncertainties in X, Y, and Z and the uncertainty in the angle θ needs to be established.

Writing the angle (θ) between the ideal vector to the beacon and the vector which contains a perturbation yields

$$\theta = \cos^{-1}\left(\left[\frac{\boldsymbol{b}^T\boldsymbol{b}_*}{|\boldsymbol{b}||\boldsymbol{b}_*|}\right]\right)$$
$$\boldsymbol{b} = \begin{bmatrix} x \\ y \\ z \end{bmatrix} \tag{27}$$
$$\boldsymbol{b}_* = \begin{bmatrix} x_* \\ y_* \\ z_* \end{bmatrix}$$

where the starred (*) quantities represent perturbed values. Taking the partial derivative of equation (27) with respect to the variable x_* results in the equation

$$\frac{\partial\theta}{\partial x_*} = \frac{\left(\frac{y_*\left(yx_* - y_*x\right) + z_*\left(zx_* - z_*x\right)}{AB\left(x_*^{\,2} + y_*^{\,2} + z_*^{\,2}\right)}\right)}{\sqrt{1 - \frac{\left(xx_* + yy_* + zz_*\right)^2}{A^2B^2}}} \tag{28}$$

where

$$A = \sqrt{x_*^{\,2} + y_*^{\,2} + z_*^{\,2}}$$

$$B = \sqrt{x^2 + y^2 + z^2}$$

Equation (28) can be rewritten as

$$\frac{\partial\theta}{\partial x_*} = \frac{y_*\left(yx_* - y_*x\right) + z_*\left(zx_* - z_*x\right)}{\sqrt{A^2B^2 - \frac{A^2B^2\left(xx_* + yy_* + zz_*\right)^2}{A^2B^2}}} \frac{1}{\left(x_*^{\,2} + y_*^{\,2} + z_*^{\,2}\right)} \tag{29}$$

which simplifies to

$$\frac{\partial\theta}{\partial x_*} = \frac{y_*\left(yx_* - y_*x\right) + z_*\left(zx_* - z_*x\right)}{\sqrt{A^2B^2 - \left(xx_* + yy_* + zz_*\right)^2}} \frac{1}{\left(x_*^{\,2} + y_*^{\,2} + z_*^{\,2}\right)} \tag{30}$$

Since the starred quantities are just the unstarred quantities plus some arbitrary perturbation, they can be represented as

$$\begin{aligned} x_* &= x + \varepsilon_x \\ y_* &= y + \varepsilon_y \\ z_* &= z + \varepsilon_z \end{aligned} \tag{31}$$

and substituted back into equation (30). Expanding out the equation and eliminating the higher order terms, the equation becomes

$$\frac{\partial\theta}{\partial x} = \frac{y\left(y\varepsilon_x - x\varepsilon_y\right) + z\left(z\varepsilon_x - x\varepsilon_z\right)}{D} \tag{32}$$

where

$$D=\left(x^2+y^2+z^2+2\left(x\varepsilon_x+y\varepsilon_y+z\varepsilon_z\right)\right)\sqrt{\left(y\varepsilon_x-x\varepsilon_y\right)^2+\left(z\varepsilon_x-x\varepsilon_z\right)^2+\left(z\varepsilon_y-y\varepsilon_z\right)^2} \tag{33}$$

In the limit, as $\varepsilon_x,\varepsilon_y,\varepsilon_z\to 0$, the values for the starred quantities become closer to the unstarred quantities (i.e. $x_*\to x;\quad y_*\to y;\quad z_*\to z$). Additionally, assuming the values for the different epsilons ($\varepsilon_x,\varepsilon_y,\varepsilon_z$) are of the same magnitude, the epsilons can be factored out of equation (32) and cancelled. Those few epsilons which do not cancel will go to zero in the limit, and the final result of the derivation is

$$\frac{\partial\theta}{\partial x}=\frac{y\left(y-x\right)+z\left(z-x\right)}{\left(\sqrt{\left(x-y\right)^2+\left(x-z\right)^2+\left(y-z\right)^2}\right)\left(x^2+y^2+z^2\right)} \tag{34}$$

The partial derivatives in the Y and Z directions are determined in the same manner, and they result in

$$\frac{\partial\theta}{\partial y}=\frac{x\left(x-y\right)+z\left(z-y\right)}{\left(\sqrt{\left(x-y\right)^2+\left(x-z\right)^2+\left(y-z\right)^2}\right)\left(x^2+y^2+z^2\right)}$$

$$\frac{\partial\theta}{\partial z}=\frac{x\left(x-z\right)+y\left(y-z\right)}{\left(\sqrt{\left(x-y\right)^2+\left(x-z\right)^2+\left(y-z\right)^2}\right)\left(x^2+y^2+z^2\right)} \tag{35}$$

With the sensitivities of the angle to the uncertainties in the X, Y, and Z directions, it is possible to write an equation for the uncertainty in the CTA as

$$u_\theta=\sqrt{\left(\frac{\partial\theta}{\partial x_*}u_X\right)^2+\left(\frac{\partial\theta}{\partial y_*}u_Y\right)^2+\left(\frac{\partial\theta}{\partial z_*}u_Z\right)^2} \tag{36}$$

Two-dimensional uncertainty in angle

In order to compare the uncertainties in the CTA with the two-dimensional near-field error plots, an equation for the uncertainty in the angle in two dimensions is required. First, write the equation for the angle between the ideal vector to the beacon and the vector which has some uncertainty.

$$\theta = \cos^{-1}\left[\frac{\boldsymbol{b}^T\boldsymbol{b}_*}{|\boldsymbol{b}||\boldsymbol{b}_*|}\right]$$
$$\boldsymbol{b} = \begin{bmatrix} x \\ z \end{bmatrix} \tag{37}$$
$$\boldsymbol{b}_* = \begin{bmatrix} x_* \\ z_* \end{bmatrix}$$

Multiplying the equation for θ and taking the partial derivatives of θ with respect to x_* and z_* yields the equations

$$\frac{\partial\theta}{\partial x_*} = \frac{-z_*}{sign\left(xz_* - x_*z\right)\left(x_*^{\,2} + z_*^{\,2}\right)}$$
$$\tag{38}$$
$$\frac{\partial\theta}{\partial z_*} = \frac{x_*}{sign\left(xz_* - x_*z\right)\left(x_*^{\,2} + z_*^{\,2}\right)}$$

The total uncertainty in the angle θ is found using the equation

$$u_\theta = \sqrt{\left(\frac{\partial\theta}{\partial x_*}u_X\right)^2 + \left(\frac{\partial\theta}{\partial z_*}u_Z\right)^2} \tag{39}$$

As with the three dimensional uncertainty case, the equations for x_* and z_* from (31) can be substituted into (38) and the limits can be taken. Also, notice that the

partials of θ with respect to x and z get squared, so the sign() functions are irrelevant. Dropping the sign() functions and substituting equations (38) into equation (39) yields

$$u_\theta = \sqrt{\left(\frac{-z}{\left(x^2+z^2\right)}u_X\right)^2 + \left(\frac{x}{\left(x^2+z^2\right)}u_Z\right)^2} \tag{40}$$

where u_X and u_Z are the uncertainties in the X and Z directions found in Table 2.

Plotting the uncertainty in θ versus the combined uncertainties in the angle due to near-field errors results in

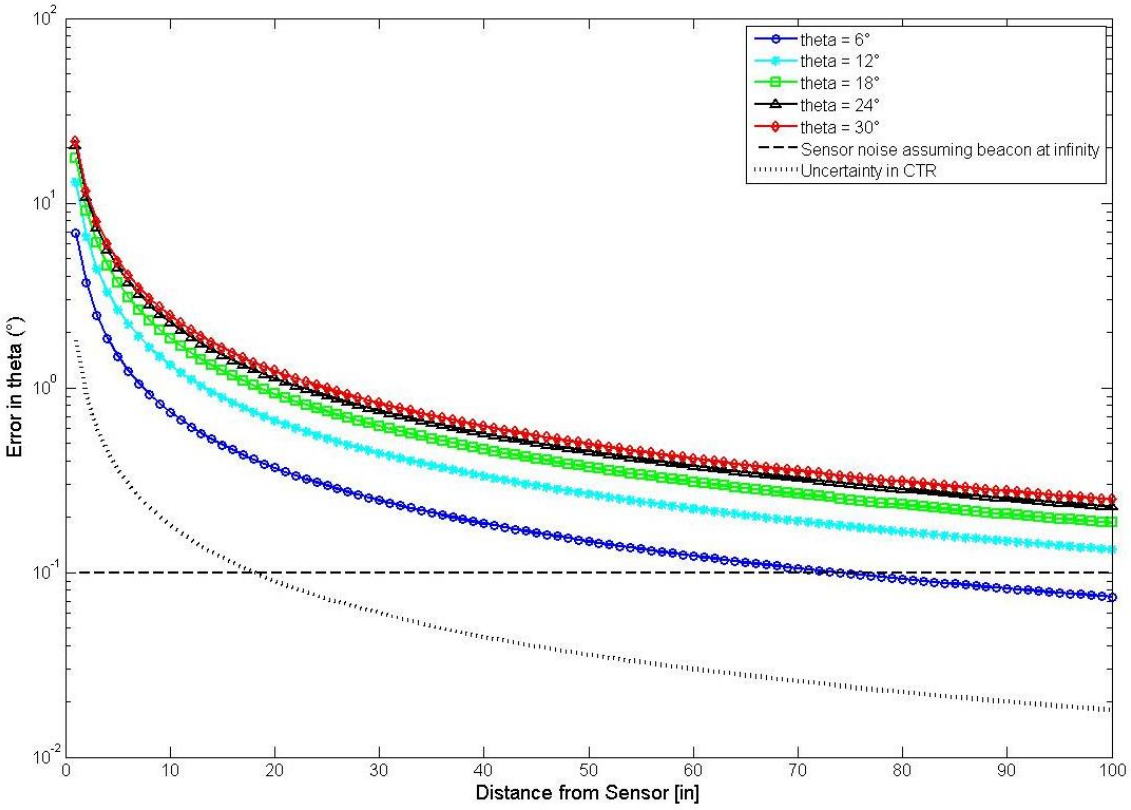

Figure 40 Uncertainty in θ due to CTA versus uncertainty in θ due to near-field errors.

As shown in Figure 40, the CTA should have the ability to resolve the near-field errors. The uncertainty in θ due to the near-field errors at 6° off boresight is over four times greater than the uncertainty in θ due to the CTA. That ratio increases to an order of magnitude difference by 18° off sensor boresight.

CHAPTER V

NORTHSTAR$_{TM}$ MODEL AND SIMULATED RESULTS

In order to calibrate the NorthStar$_{TM}$ sensor for use as a close-proximity sensor capable of generating the position and pose of another object, a mathematical model which closely simulates the sensor behavior is required. One reason for requiring an accurate mathematical model is the NorthStar$_{TM}$ sensor outputs X-Y coordinates in the Detector coordinate frame, but the desired output is a unit vector pointing from the sensor to the light source along with the corresponding covariance of the measurement. If the model can accurately predict the X-Y outputs of the NorthStar$_{TM}$ sensor given known inputs, then the measurements from the NorthStar$_{TM}$ sensor can be transformed into the desired unit vector along with the estimated covariance.

In order to generate such a model, assumptions about how the NorthStar$_{TM}$ sensor generated its output were made. Since the NorthStar$_{TM}$ sensor is proprietary, it is treated as a "black box" and its behavior assumed to be based on first principles. The generation of the model which attempts to capture the first-order functionality of the NorthStar$_{TM}$ sensor will be discussed later.

NorthStar$_{TM}$ Theory of Operation

An understanding of how the NorthStar$_{TM}$ sensor likely functions is important for developing a model which can accurately predict what the NorthStar$_{TM}$ sensor will output given any system inputs. To begin developing this understanding, make the simple assumption that the NorthStar$_{TM}$ sensor has no *a priori* knowledge of the location

of the light source in space. This assumption is reasonable because the NorthStar$_{TM}$ sensor does not know where it is or what its environment is like when it is powered on. Since the NorthStar$_{TM}$ sensor is intended for use in many different applications, specific information such as beacon location or room size cannot be preprogrammed and stored onboard the unit itself. The only information the NorthStar$_{TM}$ has available to it is IR light entering with some measured intensity in some region of its field of view (FOV).

When the NorthStar$_{TM}$ sensor is powered on, it will "see" the beacons in its field of view (up to twenty at a time) and report their X-Y location in Detector coordinates. Figure 41 depicts the NorthStar$_{TM}$ sensor sitting on its X-Y plane with its FOV given by the outer solid lines. The dotted line represents a line of sight vector to a light source which can be located at any point along the dotted line (in the figure it is shown in two possible locations). The NorthStar$_{TM}$ sensor may be able to locate the angle to the light source with respect to the sensor boresight, but there is no way to locate where along the vector the light is located. It cannot use the intensity of the light source to determine the distance since there is no way to distinguish between a closer source with a weak signal and a source farther away but with a stronger signal.

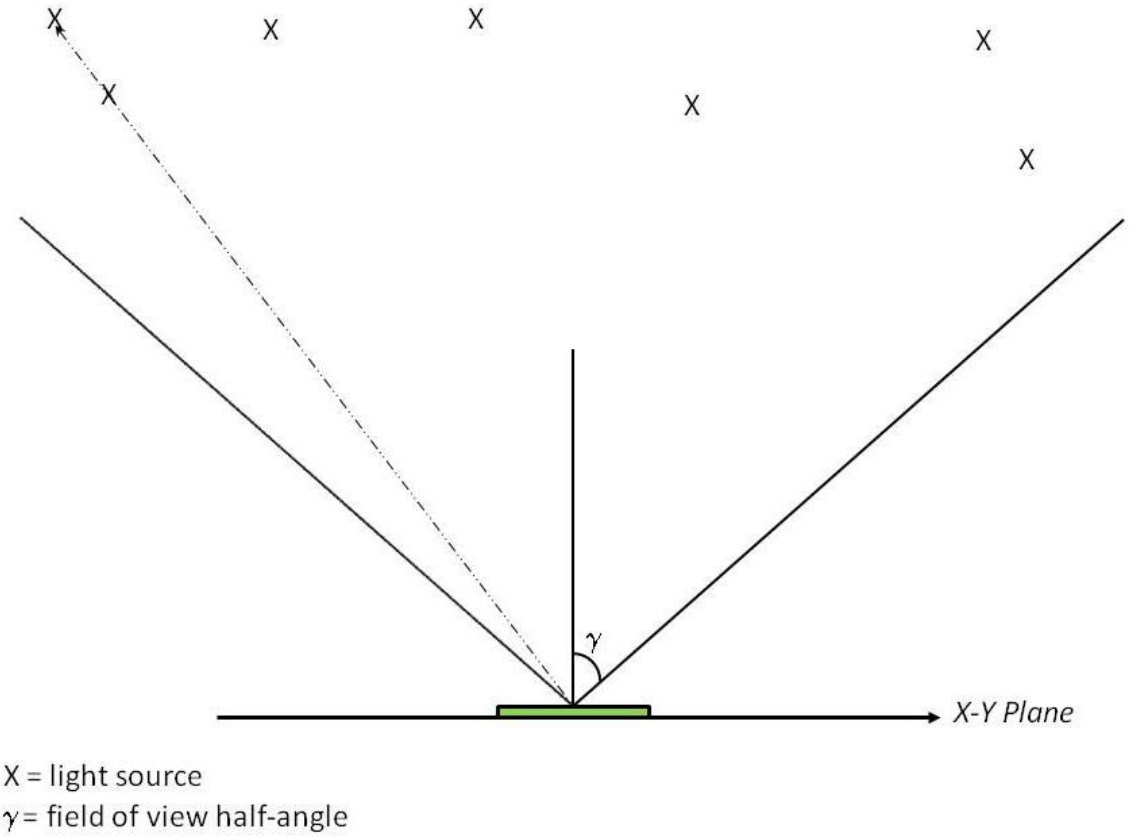

Figure 41 Representation of the NorthStar$_{TM}$ sensor with several light sources in its field of view.

It is clear that the light source along the vector originating at the NorthStar$_{TM}$ sensor origin will have different X or Y values in Detector coordinates depending on where along the vector it lies. How then does the NorthStar$_{TM}$ unit generate a beacon position?

It is reasonable to assume that since the NorthStar$_{TM}$ sensor cannot generate a vector with known length to a light source, but it is able to determine a direction to the light source, the sensor must be generating a unit vector from the sensor origin to the

light source which it locates on its own internal unit hemisphere. Now instead of the representation in Figure 41, we have the representation shown in Figure 42.

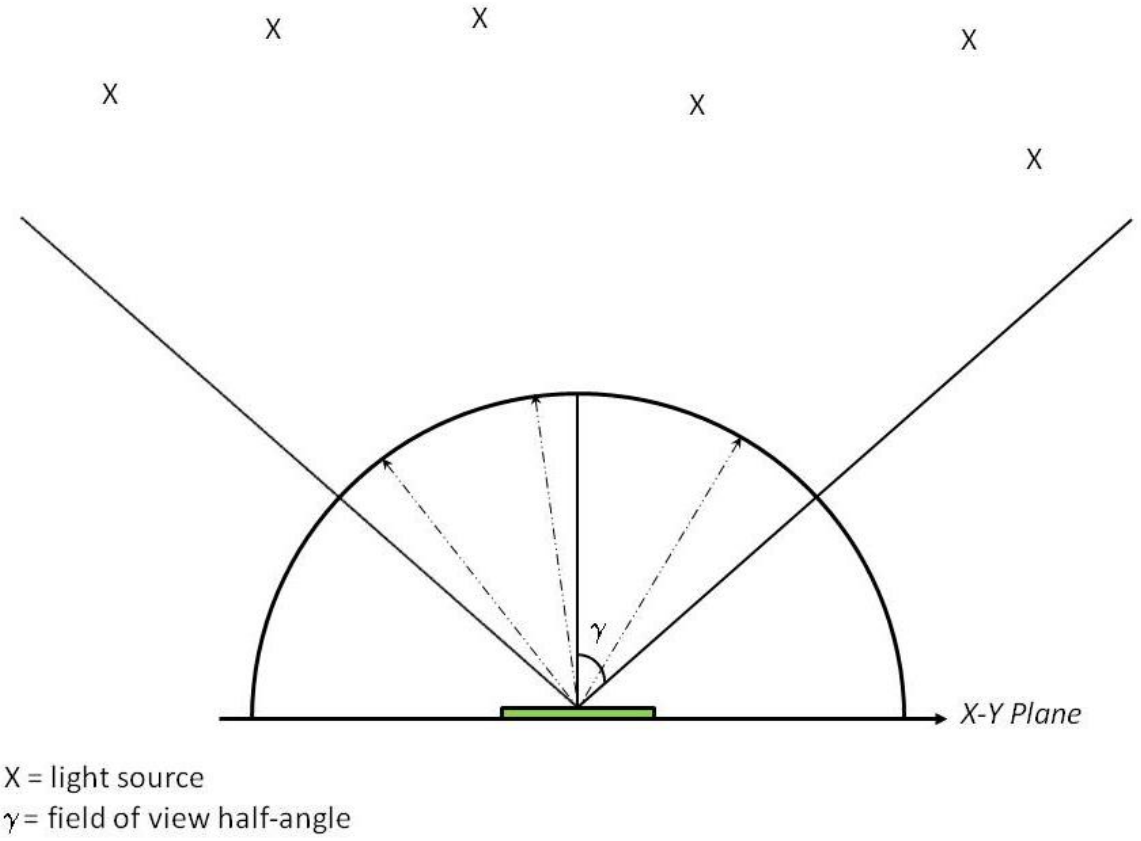

Figure 42 Representation of NorthStar$_{TM}$ sensor projecting light directions onto a unit hemisphere.

Locating the light source on a unit hemisphere is only a partial solution to the problem of generating an X-Y position in Detector coordinates. There is still no knowledge of where along that unit vector direction the light source is located, and therefore no knowledge of its position when projected onto the coordinate plane. At this point, in order to proceed, an assumption was made about the NorthStar$_{TM}$ sensor. The sensor is intended for use in one of two ways: either it can track IR light reflected off a

surface (such as a ceiling), or it can track IR lights directly in a beacon mode [11]. In either case, the detector is assumed to be indoors with a maximum recommended ceiling height of six meters (twenty feet) [14]. It is assumed, therefore, that the NorthStar$_{TM}$ sensor "thinks" that all of the light sources it detects are located on a plane (or ceiling) that is parallel to the Detector coordinate X-Y plane and is separated by a distance (or height) of H.

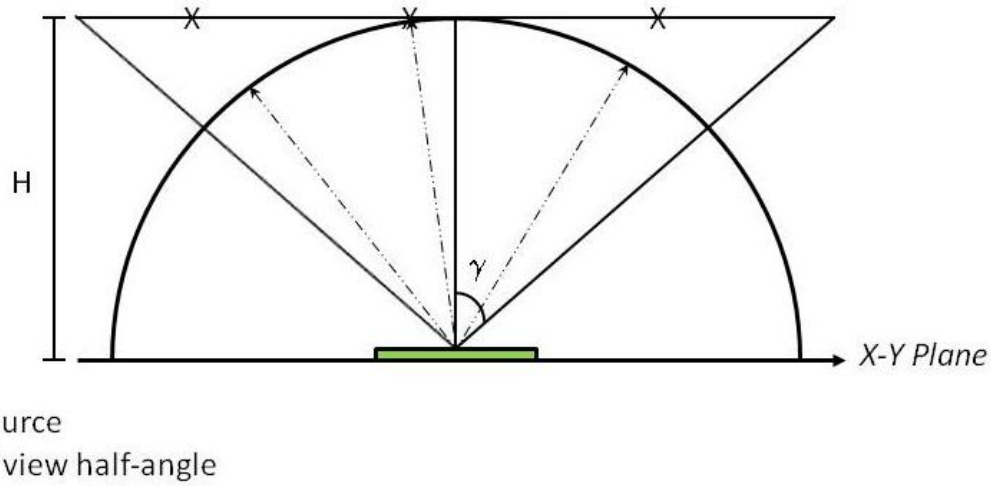

Figure 43 Representation of the proposed internal assumptions made by the NorthStar$_{TM}$ sensor.

Having the NorthStar$_{TM}$ sensor assume the light sources are all located on a plane leads to the representation of the NorthStar$_{TM}$ sensor functionality shown in Figure 43. The NorthStar$_{TM}$ sensor locates the direction of the light source on its unit hemisphere, then it projects the light onto a parallel plane separated by a distance H (representing the room height). The parameter H, therefore, is a scaling factor for the NorthStar$_{TM}$ measurements in much the same way as the focal length of a lens becomes a scaling factor in the collinearity equations used in problems dealing with star tracker cameras

[15]. Note that the collinearity equations are not necessarily valid in this case because the NorthStar$_{TM}$ sensor is not a pinhole camera but a CSS. However, collinearity-like equations will be developed to see what the range of validity is. The value for H is something that could be calibrated at the factory and loaded into the NorthStar$_{TM}$ sensor before it is ever shipped to the end user, with variations in the actual room height accounted for by the uncertainty bounds quoted in the product data sheet.

Qualitative experiments were run in which an IR LED was moved around in front of the NorthStar$_{TM}$ sensor and the change in the X and Y values generated by the sensor noted. Results from these qualitative experiments indicated that as the angle between the light source and the sensor boresight increases, the magnitude of the X and/or Y measurement increases. Defining the angle γ as the FOV half-angle such that the NorthStar$_{TM}$ FOV equals 2γ, it is proposed that the maximum value for X (32,768) is achieved when the light source is located on the X-axis of the Detector coordinate frame and makes an angle of γ with the NorthStar$_{TM}$ sensor boresight (see Figure 44). The minimum value of X and the minimum and maximum values of Y are defined similarly.

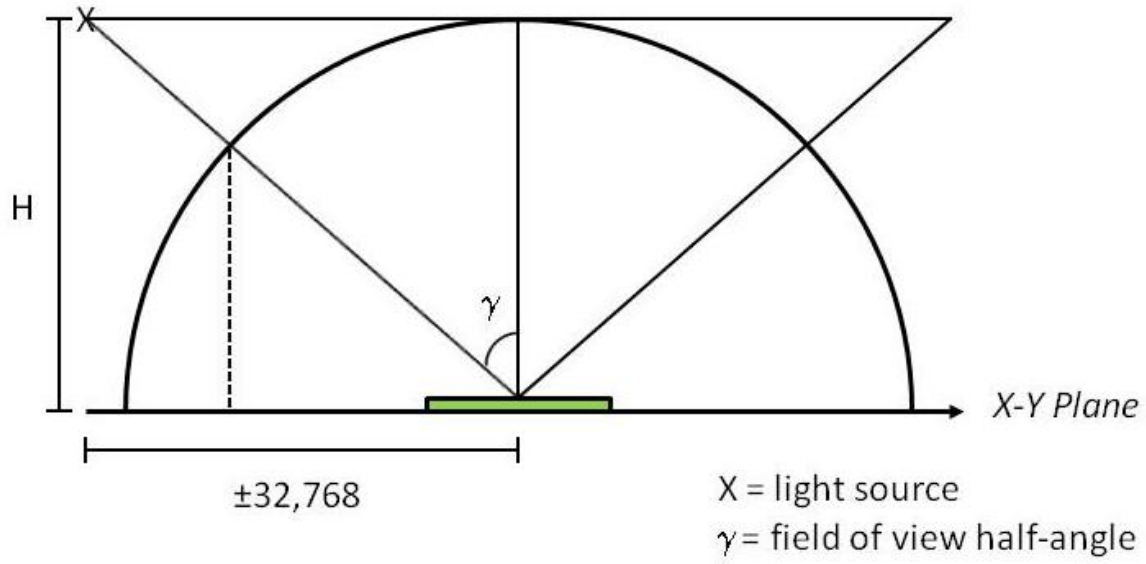

Figure 44 Representation of a light source on the edge of the FOV generating a minimum or maximum measurement value.

The NorthStar$_{TM}$ product data sheet [14] states that the detector has a square FOV. It is important, then, for the proposed method of operation described above to result in a square field of view. From Figure 44, it can be seen that at any scale height H, the FOV of the sensor is a square spanning [-60°, 60°] in the X direction and [-60°, 60°] in the Y direction. The method of operation proposed in this section thus passes its first sanity check, and may be used to derive a model which can be tested against the actual NorthStar$_{TM}$ sensor hardware.

To summarize, it is proposed that the NorthStar$_{TM}$ sensor detects incoming IR light modulated at pre-defined frequencies and determines the direction to the light source. The sensor then presumably projects the direction onto a plane at some height H above the Detector X-Y plane and then projects it down onto its own Detector X-Y plane to determine the position in its planar coordinate system.

Mathematical Model Geometry

Having developed a concept for how the NorthStar$_{TM}$ sensor generates its X and Y measurements, it is possible to begin developing a mathematical model to approximate this behavior. In order to locate the beacons with respect to the sensor's Detector coordinate system origin, attach a coordinate system (designated $\mathcal{O}$) to the NorthStar$_{TM}$ sensor which has an axis coincident with the Detector frame X-axis and one axis coincident with the Detector frame Y-axis, with the third axis completing the triad according to the right hand rule. X and Y measurements from the sensor now have meaning in the $\mathcal{O}$-frame. Note, however, that because the NorthStar$_{TM}$ sensor is a "black box," the origin of the Detector coordinate system is unknown. A scheme for empirically determining the Detector coordinate system origin of each individual NorthStar$_{TM}$ sensor might be devised, but that would require additional analyses of the uncertainty in the testing procedure and measurement equipment.

Instead, since the NorthStar$_{TM}$ sensor is not meant to be a stand-alone sensor but integrated into some system, it is assumed that the sensor is mounted to the NorthStar$_{TM}$ sensor board. The NorthStar$_{TM}$ sensor PCB also has a coordinate system (designated $\mathcal{N}$) affixed at an arbitrary location. However, since the origin of the $\mathcal{N}$-frame is arbitrarily chosen by the user, its location is known. Figure 45 shows a depiction of the NorthStar$_{TM}$ sensor (dubbed NorthStar$_{TM}$ Sensor Head or NSSH) without its protective cover mounted to the NorthStar$_{TM}$ sensor board (NS board) with a known coordinate

system origin ($\mathcal{N}$). Note that in the ideal case, the three axes of the $\mathcal{N}$-frame align with the three axes of the $\mathcal{O}$-frame but may be offset by some distance.

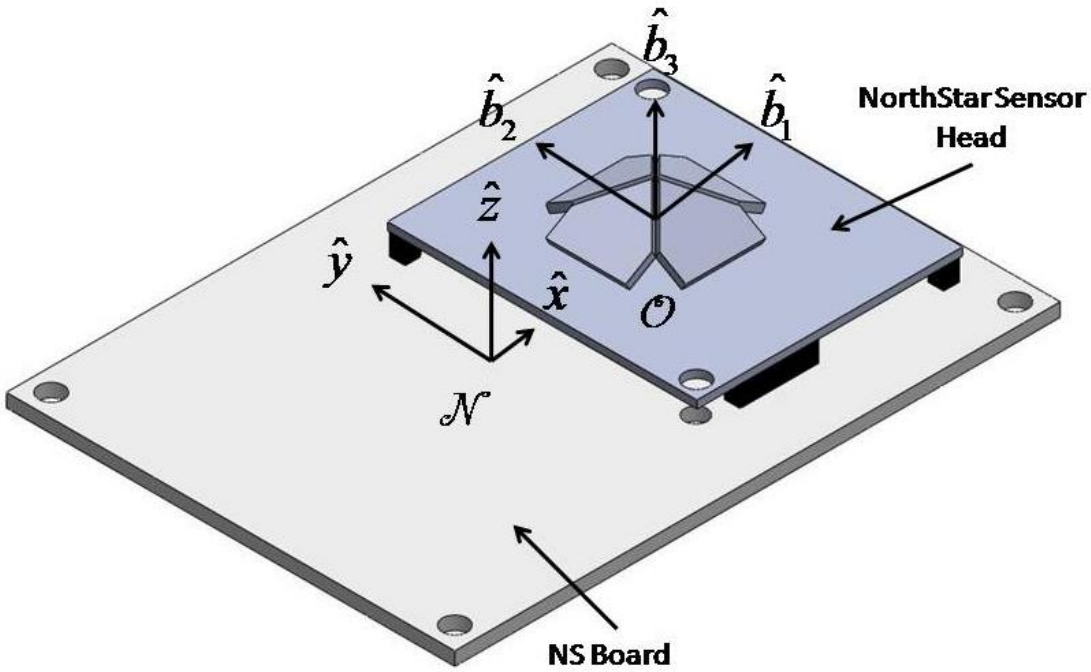

Figure 45 Depiction of the NorthStar$_{TM}$ sensor attached to the NS board with a known coordinate system origin.

The origin of the NSSH frame is not known precisely, but is assumed to be in the vicinity of the four PV cells in pyramid formation which measure the incoming light. A side view and a top view of the sensor system are provided in Figure 46 and Figure 47, respectively.

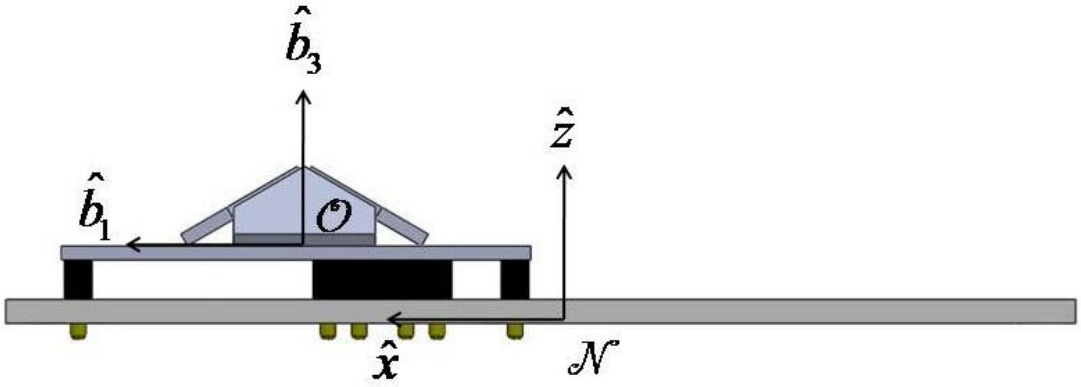

Figure 46 Side view of NSSH and NS board. Note that while the coordinate axes are offset, they are aligned in the same manner.

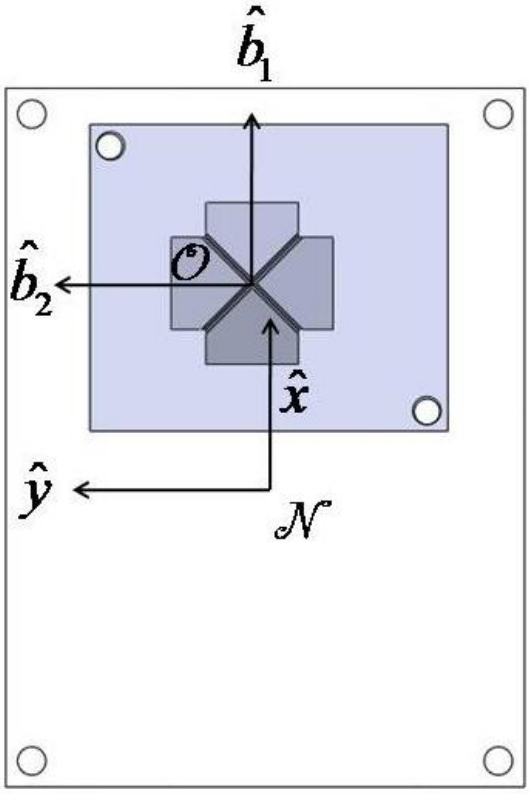

Figure 47 Top view of the NSSH and NS board. Again note the axes are aligned but offset.

As the machining tolerances and assembly imperfections guarantee that the two coordinate systems will not be perfectly aligned, assume there exists a direction cosine matrix (C) that will rotate the $\mathcal{N}$-frame into alignment with the $\mathcal{O}$-frame such that

$$\begin{Bmatrix} \hat{b}_1 \\ \hat{b}_2 \\ \hat{b}_3 \end{Bmatrix}_O = \begin{bmatrix} C_{11} & C_{12} & C_{13} \\ C_{21} & C_{22} & C_{23} \\ C_{31} & C_{32} & C_{33} \end{bmatrix} \begin{Bmatrix} \hat{x} \\ \hat{y} \\ \hat{z} \end{Bmatrix}_N \tag{41}$$

Due to the fact that the $\mathcal{N}$-frame was chosen to ideally align with the $\mathcal{O}$-frame, the off-diagonal terms in the direction cosine matrix (C) are expected to be small and therefore C will be close to the identity matrix. Equation (41), however, has not been specialized for small rotations and is therefore general enough to handle arbitrarily large misalignments.

Equation (41) can be used to discover how the two coordinate frames are misaligned, but now the offset between the two coordinate systems needs to be accounted for. Define a vector $\boldsymbol{d}$ which points from the $\mathcal{N}$-frame origin to the $\mathcal{O}$-frame origin, and is coordinatized in $\mathcal{N}$-frame components (see Figure 48) such that

$$\boldsymbol{d} = d_1\hat{x} + d_2\hat{y} + d_3\hat{z} \tag{42}$$

The vector $\boldsymbol{d}$ is necessarily unknown because the origin of the $\mathcal{O}$-frame is unknown. It can, however, be estimated as will be discussed later. Assuming the vector $\boldsymbol{d}$ and the matrix C can be obtained, the output of the NorthStar$_{TM}$ sensor in its Detector coordinate frame can be related directly through a rotation and translation to the $\mathcal{N}$-frame, a frame whose location is specified and therefore known to some arbitrary

tolerance. The only limits on the knowledge of the location of the $\mathcal{N}$-frame origin are machining precision and the precision of the measurement instruments.

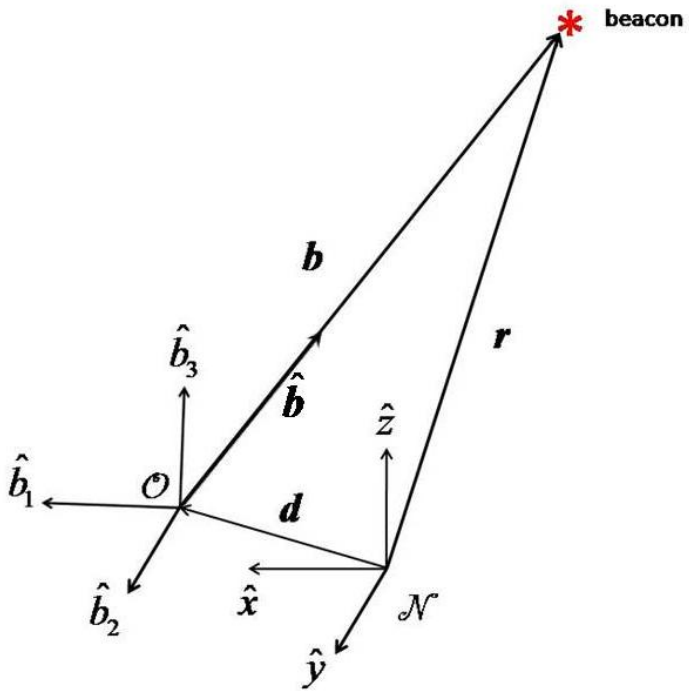

Figure 48 Depiction of the relationships between the two coordinate systems and a beacon.

Mathematical Model Development

Assume there is a beacon located at a known position somewhere in the NorthStar$_{TM}$ sensor's FOV. The beacon's location can be described in $\mathcal{N}$-frame coordinates as given by (43).

$$\boldsymbol{r} = r_1\hat{x} + r_2\hat{y} + r_3\hat{z} \tag{43}$$

From Figure 48 and equations (42) and (43), the vector from the NSSH to the beacon can be expressed in $\mathcal{N}$-frame coordinates as

$$\boldsymbol{b} = (r_1 - d_1)\hat{x} + (r_2 - d_2)\hat{y} + (r_3 - d_3)\hat{z} \tag{44}$$

Note that the vector $\boldsymbol{b}$ is not a unit vector. In developing the theory of how the NorthStar$_{TM}$ sensor generates X and Y measurements, it was assumed the sensor generated unit vectors pointing in the direction of the light source (in this case a beacon) in order to produce X and Y measurements. Equation (44), then, needs to be normalized, resulting in

$$\hat{\boldsymbol{b}} = \frac{\boldsymbol{b}}{|\boldsymbol{b}|} = \frac{(r_1 - d_1)\hat{x} + (r_2 - d_2)\hat{y} + (r_3 - d_3)\hat{z}}{\sqrt{(r_1 - d_1)^2 + (r_2 - d_2)^2 + (r_3 - d_3)^2}} \tag{45}$$

where the carat (^) indicates a unit vector. The unit vector $\hat{\boldsymbol{b}}$ can be rewritten simply as

$$\hat{\boldsymbol{b}} = \begin{bmatrix} b_1 \\ b_2 \\ b_3 \end{bmatrix}_N \tag{46}$$

$$\begin{bmatrix} b_1 \\ b_2 \\ b_3 \end{bmatrix}_N = \frac{1}{|\boldsymbol{b}|} \begin{bmatrix} r_1 - d_1 \\ r_2 - d_2 \\ r_3 - d_3 \end{bmatrix}_N \tag{47}$$

$$|\boldsymbol{b}| = \sqrt{(r_1 - d_1)^2 + (r_2 - d_2)^2 + (r_3 - d_3)^2} \tag{48}$$

The unit vector $\hat{\boldsymbol{b}}$ is a vector pointing from the $\mathcal{O}$-frame origin to the beacon, but it is referenced in $\mathcal{N}$-frame coordinates. In order to use $\hat{\boldsymbol{b}}$ to generate estimated X-Y measurements, it is required to re-coordinatize $\hat{\boldsymbol{b}}$ from the $\mathcal{N}$-frame to the $\mathcal{O}$-frame. This is done by utilizing the direction cosine matrix C from equation (41).

$$\begin{bmatrix} b_1 \\ b_2 \\ b_3 \end{bmatrix}_O = \begin{bmatrix} C_{11} & C_{12} & C_{13} \\ C_{21} & C_{22} & C_{23} \\ C_{31} & C_{32} & C_{33} \end{bmatrix} \begin{bmatrix} b_1 \\ b_2 \\ b_3 \end{bmatrix}_N \tag{49}$$

Equation (49) provides a relationship between the reference vector to a beacon and the unit vector pointing from the NorthStar$_{TM}$ sensor to the beacon. It is now required to develop a relationship between this unit vector coordinatized in the ©-frame and the X-Y measurements produced by the NorthStar$_{TM}$ sensor.

To begin, recall from the derivation of the proposed NorthStar$_{TM}$ sensor theory of operation that the parameter H is a scaling height for the NorthStar$_{TM}$ sensor measurements (the same H as in earlier chapters). Multiplying equation (49) by H results in

$$H\begin{bmatrix} b_1 \\ b_2 \\ b_3 \end{bmatrix}_O = H\begin{bmatrix} C_{11} & C_{12} & C_{13} \\ C_{21} & C_{22} & C_{23} \\ C_{31} & C_{32} & C_{33} \end{bmatrix}\begin{bmatrix} b_1 \\ b_2 \\ b_3 \end{bmatrix}_N \tag{50}$$

Dividing everything by b_3, equation (50) is rewritten as

$$\tilde{y}_x = \begin{bmatrix} 1 & 0 & 0 \end{bmatrix}\frac{H}{b_{3O}}\begin{bmatrix} b_1 \\ b_2 \\ b_3 \end{bmatrix}_O = \begin{bmatrix} 1 & 0 & 0 \end{bmatrix}\begin{bmatrix} C_{11} & C_{12} & C_{13} \\ C_{21} & C_{22} & C_{23} \\ C_{31} & C_{32} & C_{33} \end{bmatrix}\frac{H}{b_{3O}}\begin{bmatrix} b_1 \\ b_2 \\ b_3 \end{bmatrix}_N$$

$$\tilde{y}_y = \begin{bmatrix} 0 & 1 & 0 \end{bmatrix}\frac{H}{b_{3O}}\begin{bmatrix} b_1 \\ b_2 \\ b_3 \end{bmatrix}_O = \begin{bmatrix} 0 & 1 & 0 \end{bmatrix}\begin{bmatrix} C_{11} & C_{12} & C_{13} \\ C_{21} & C_{22} & C_{23} \\ C_{31} & C_{32} & C_{33} \end{bmatrix}\frac{H}{b_{3O}}\begin{bmatrix} b_1 \\ b_2 \\ b_3 \end{bmatrix}_N \tag{51}$$

$$\tilde{y}_z = \begin{bmatrix} 0 & 0 & 1 \end{bmatrix}\frac{H}{b_{3O}}\begin{bmatrix} b_1 \\ b_2 \\ b_3 \end{bmatrix}_O = \begin{bmatrix} 0 & 0 & 1 \end{bmatrix}\begin{bmatrix} C_{11} & C_{12} & C_{13} \\ C_{21} & C_{22} & C_{23} \\ C_{31} & C_{32} & C_{33} \end{bmatrix}\frac{H}{b_{3O}}\begin{bmatrix} b_1 \\ b_2 \\ b_3 \end{bmatrix}_N$$

where the tilde symbol (~) indicates a measured value. The terms $\tilde{y}_x$ and $\tilde{y}_y$ represent the X and Y outputs from the NorthStar$_{TM}$ sensor, while $\tilde{y}_z$ is a fictitious measurement. Equations (51) simplify to

$$\begin{aligned} \tilde{y}_x &= H\left[\frac{C_{11}b_{1N}+C_{12}b_{2N}+C_{13}b_{3N}}{C_{31}b_{1N}+C_{32}b_{2N}+C_{33}b_{3N}}\right] \\ \tilde{y}_y &= H\left[\frac{C_{21}b_{1N}+C_{22}b_{2N}+C_{23}b_{3N}}{C_{31}b_{1N}+C_{32}b_{2N}+C_{33}b_{3N}}\right] \\ \tilde{y}_z &= H \end{aligned} \tag{52}$$

Substituting equations (47) into equations (52) (and ignoring $\tilde{y}_z$, which is not an output of the NorthStar$_{TM}$ sensor) yields the expressions

$$\tilde{y}_x = H\left[\frac{\left(C_{11}\left(r_1-d_1\right)+C_{12}\left(r_2-d_2\right)+C_{13}\left(r_3-d_3\right)\right)\Big/|\boldsymbol{b}|}{\left(C_{31}\left(r_1-d_1\right)+C_{32}\left(r_2-d_2\right)+C_{33}\left(r_3-d_3\right)\right)\Big/|\boldsymbol{b}|}\right]$$

$$\tilde{y}_y = H\left[\frac{\left(C_{21}\left(r_1-d_1\right)+C_{22}\left(r_2-d_2\right)+C_{23}\left(r_3-d_3\right)\right)\Big/|\boldsymbol{b}|}{\left(C_{31}\left(r_1-d_1\right)+C_{32}\left(r_2-d_2\right)+C_{33}\left(r_3-d_3\right)\right)\Big/|\boldsymbol{b}|}\right]$$

which finally reduce to the equations relating the known reference vectors $\boldsymbol{r}$, the ©-frame origin offset $\boldsymbol{d}$, and the NorthStar$_{TM}$ sensor X and Y measurements $\tilde{y}_x$ and $\tilde{y}_y$.

$$\tilde{y}_x = H\left[\frac{C_{11}(r_1-d_1)+C_{12}(r_2-d_2)+C_{13}(r_3-d_3)}{C_{31}(r_1-d_1)+C_{32}(r_2-d_2)+C_{33}(r_3-d_3)}\right]$$
$$\tilde{y}_y = H\left[\frac{C_{21}(r_1-d_1)+C_{22}(r_2-d_2)+C_{23}(r_3-d_3)}{C_{31}(r_1-d_1)+C_{32}(r_2-d_2)+C_{33}(r_3-d_3)}\right] \quad (53)$$

While equations (53) provide a way to relate the measurements from the NorthStar$_{TM}$ sensor to the vectors $\boldsymbol{r}$ and $\boldsymbol{d}$, the direction cosine matrix is still unknown. It is required, then, to estimate the values for the elements of the direction cosine matrix. The direction cosine matrix is a proper orthogonal matrix which can be represented in many ways. A minimum representation of C will be a three-element parameterization, with examples of these being Euler's angles, Gibb's vector, the principal axis/principal angle, and the Modified Rodrigues Parameters (MRP) [16].

As the rotation from the $\mathcal{N}$-frame to the $\mathcal{O}$-frame is expected to be small, a parameterization that works well for small rotations is desirable. For this derivation, the MRP will be used to parameterize the direction cosine matrix because they do not have a singularity until the principal angle of rotation is equal to 2π. Defining the MRP as

$$\boldsymbol{p} \equiv \begin{bmatrix} p_1 \\ p_2 \\ p_3 \end{bmatrix}$$

the direction cosine matrix C can be written in compact form as

$$[C] = I_{3\times3} + \frac{8[\boldsymbol{p}\times]^2 - 4(1-\boldsymbol{p}^T\boldsymbol{p})[\boldsymbol{p}\times]}{(1+\boldsymbol{p}^T\boldsymbol{p})^2}$$

$$[\boldsymbol{p}\times] = \begin{bmatrix} 0 & -p_3 & p_2 \\ p_3 & 0 & -p_1 \\ -p_2 & p_1 & 0 \end{bmatrix} \tag{54}$$

as shown in [16], where I_{3x3} is a 3x3 identity matrix. Equations (54) can be expanded to find the value of each of the nine elements in the direction cosine matrix. The result of the expansion is given in reference [16] as

$$[C] = \frac{1}{(1+p^2)^2}\begin{bmatrix} 4(p_1^2 - p_2^2 - p_3^2) + (1-p^2)^2 & 8p_1p_2 + 4p_3(1-p^2) & \cdots \\ 8p_1p_2 - 4p_3(1-p^2) & 4(-p_1^2 + p_2^2 - p_3^2) + (1-p^2)^2 & \cdots \\ 8p_1p_3 + 4p_2(1-p^2) & 8p_2p_3 - 4p_1(1-p^2) & \cdots \end{bmatrix}$$

$$\begin{bmatrix} 8p_1p_3 - 4p_2(1-p^2) \\ 8p_2p_3 + 4p_1(1-p^2) \\ 4(-p_1^2 - p_2^2 + p_3^2) + (1-p^2)^2 \end{bmatrix} \tag{55}$$

$$p^2 = \boldsymbol{p}^T\boldsymbol{p}$$

By taking the correct elements from the direction cosine matrix in (55) and substituting them in equations (53), the measurements from the NorthStar$_{TM}$ sensor can be related to a known reference frame through seven unknown parameters: three MRP, three from the unknown vector ***d***, and one scaling height H. Equations (53) represent two independent equations, five less than the number of unknown parameters. However, taking many independent measurements (i.e. measurements of beacons in different locations) and stacking them effectively results in many more equations than unknown

parameters. The solution of a problem with more equations than unknowns can be obtained by using a least squares approach.

Gaussian Least Squares Differential Correction (GLSDC)

GLSDC is a widely used nonlinear least squares estimation technique for iteratively solving problems like the one described above in which there are more unknowns than equations. A GLSDC algorithm seeks to minimize the sum of the squares of the residual errors between the measured values and the estimated values, and the cost function is written as [15]

$$J = \tfrac{1}{2}\left(\Delta\mathbf{y}_c - H_c\Delta\boldsymbol{x}\right)^T W\left(\Delta\mathbf{y}_c - H_c\Delta\boldsymbol{x}\right) \tag{56}$$

where

$\boldsymbol{x}_c \equiv$ *current estimate*
$\Delta\boldsymbol{x} \equiv$ *unknown set of corrections to the current estimate*
$\Delta\boldsymbol{y}_c \equiv \tilde{\boldsymbol{y}} - \mathbf{f}(\boldsymbol{x}_c) =$ *residual between the measurement and current estimate*
$G \equiv \left.\dfrac{\partial\mathbf{f}}{\partial\boldsymbol{x}}\right|_{x_c} =$ *Jacobian matrix evaluated at the current estimate*
$W =$ *weighting matrix*

The matrix W determines how much each measurement weighs in the final cost. If each measurement weighs the same amount, W can be replaced with an identity matrix. The cost function J is minimized with respect to the unknown set of corrections to the current estimate. Taking the derivative of the cost function with respect to $\Delta\boldsymbol{x}$ and then rearranging the equation results in a version of the normal equations written as

$$\Delta\boldsymbol{x} = PG^TW\Delta\boldsymbol{y}_c \tag{57}$$

where

$$P \equiv \left(G^T W G\right)^{-1} \tag{58}$$

Equation (57) is calculated, the current estimate is updated using

$$\boldsymbol{x}_c = \boldsymbol{x}_c + \Delta \boldsymbol{x} \tag{59}$$

and the algorithm iterates until a stopping condition (either some tolerance or a maximum number of iterations) is reached.

NorthStar$_{TM}$ Mathematical Model Test

Emulate NorthStar$_{TM}$ sensor output

Before the NorthStar$_{TM}$ mathematical model can be tested, emulated NorthStar$_{TM}$ sensor outputs must be generated. First, a ten inch grid with one hundred LEDs spaced as they are on the beacon array was simulated in Matlab. The grid was moved from one inch separation from the simulated sensor out to one hundred inches, calculating the vectors ($\boldsymbol{r_i}$, see equation (43) and Figure 48) from the $\mathcal{N}$-frame origin to the beacon in $\mathcal{N}$-frame coordinates (resulting in 10,000 vectors).

In order to generate simulated voltages for the NorthStar$_{TM}$ sensor, the normal vectors to each of the four PV cells must be obtained (see Figure 49).

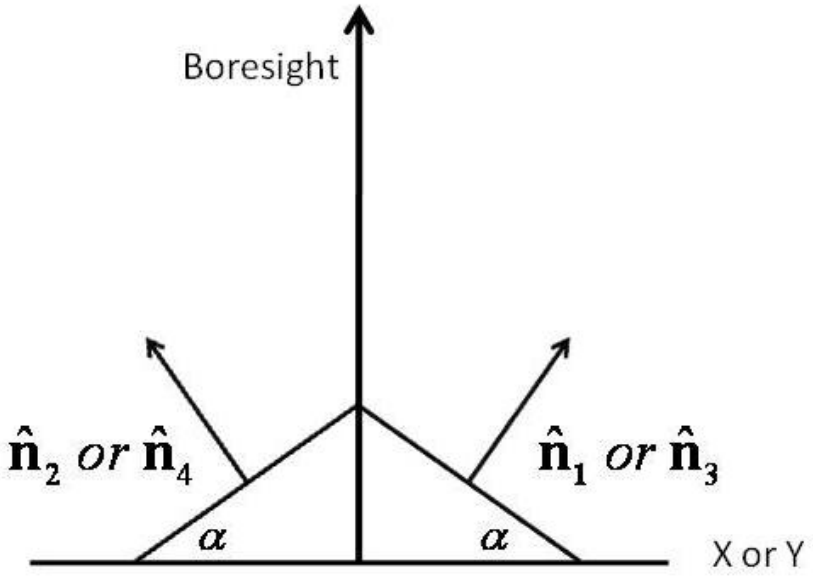

Figure 49 Normal vectors to each of the four PV cells.

Assuming the angle α is the same for all four panels (recall that α equals 30° for this thesis), the four normal vectors can be written in the ℴ-frame as

$$\begin{aligned}
\hat{\boldsymbol{n}}_1 &= \begin{bmatrix} \sin\alpha & 0 & \cos\alpha \end{bmatrix}^T \\
\hat{\boldsymbol{n}}_2 &= \begin{bmatrix} -\sin\alpha & 0 & \cos\alpha \end{bmatrix}^T \\
\hat{\boldsymbol{n}}_3 &= \begin{bmatrix} 0 & \sin\alpha & \cos\alpha \end{bmatrix}^T \\
\hat{\boldsymbol{n}}_4 &= \begin{bmatrix} 0 & -\sin\alpha & \cos\alpha \end{bmatrix}^T
\end{aligned} \tag{60}$$

The normal vectors need to be re-coordinatized in the ℕ-frame in order to perform the dot product between the normal vectors and the vectors to the beacons. Using equation (55) to compute the direction cosine matrix taking a vector from the ℕ-frame to the ℴ-frame, the normal vectors are re-coordinatized into the ℕ-frame by multiplying each normal vector by C^T.

Figure 50, as with Figure 10, shows the definition of the vectors from the PV cells to the beacon and from the ©-frame origin to the PV cells. The vectors $\boldsymbol{r_i}$ from the N-frame origin are moved to the ©-frame origin (i.e. made into the $\boldsymbol{b_{inf}}$ shown in Figure 50) using equation (44). The vectors $\boldsymbol{b_{inf}}$ are then transformed into the vectors $\boldsymbol{b_1}$ and $\boldsymbol{b_2}$ ($\boldsymbol{b_3}$ and $\boldsymbol{b_4}$ for the Y-direction) by subtracting the offset vectors.

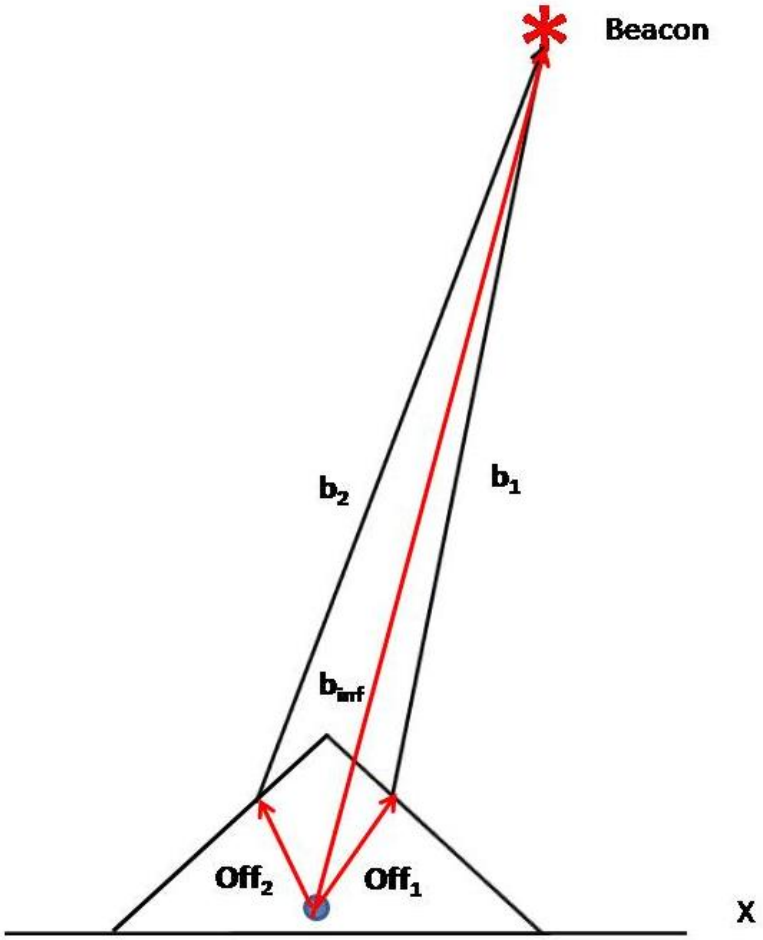

Figure 50 Illustration of the offset vectors in the X direction.

For this simulation, the offset vectors are arbitrarily chosen to be

$$\begin{aligned}
\boldsymbol{Off}_1 &= \begin{bmatrix} 0.175 & 0 & 0 \end{bmatrix}^T \\
\boldsymbol{Off}_2 &= \begin{bmatrix} -0.175 & 0 & 0 \end{bmatrix}^T \\
\boldsymbol{Off}_3 &= \begin{bmatrix} 0 & 0.175 & 0 \end{bmatrix}^T \\
\boldsymbol{Off}_4 &= \begin{bmatrix} 0 & -0.175 & 0 \end{bmatrix}^T
\end{aligned} \tag{61}$$

with units given in inches. Using these values, the voltages on each of the PV cells can be written as

$$\begin{aligned}
V_1 &= \left(C^T \hat{\boldsymbol{n}}_1 \right)^T \frac{\boldsymbol{b}_1}{|\boldsymbol{b}_1|} \\
V_2 &= \left(C^T \hat{\boldsymbol{n}}_2 \right)^T \frac{\boldsymbol{b}_2}{|\boldsymbol{b}_2|} \\
V_3 &= \left(C^T \hat{\boldsymbol{n}}_3 \right)^T \frac{\boldsymbol{b}_3}{|\boldsymbol{b}_3|} \\
V_4 &= \left(C^T \hat{\boldsymbol{n}}_4 \right)^T \frac{\boldsymbol{b}_4}{|\boldsymbol{b}_4|}
\end{aligned} \tag{62}$$

Calculating the intensities on each panel and the scaling factors (due to a non-uniform light source, assume 60° half-intensity angle) as described in Chapter II, the emulated NorthStar$_{TM}$ sensor measurements can be written as

$$\begin{aligned}
\tilde{X} &= \beta \left(\frac{c_1 I_1 V_1 - c_2 I_2 V_2}{c_1 I_1 V_1 + c_2 I_2 V_2} \right) \\
\tilde{Y} &= \beta \left(\frac{c_3 I_3 V_3 - c_4 I_4 V_4}{c_3 I_3 V_3 + c_4 I_4 V_4} \right)
\end{aligned} \tag{63}$$

where the tilde (~) represents a measured value and β is a proportionality constant (here β equals 32,768). Using equation (63), X and Y measurements were generated for all the $\boldsymbol{r}_i$ vectors. These measurements take into account all of the expected non-linear near-field effects. Figure 51 shows the simulated measurements from three inches out to thirty

inches. Notice that as the grid moves away from the sensor, it takes up less of the NorthStar$_{TM}$ sensor's FOV. By thirty inches separation distance, the beacon array takes up only ~20° of the FOV (using the single beacon array configuration). Additionally, the NorthStar$_{TM}$ sensor head is not located directly under the center beacon in the beacon array, so there is a noticeable offset in the grid pattern along the X direction.

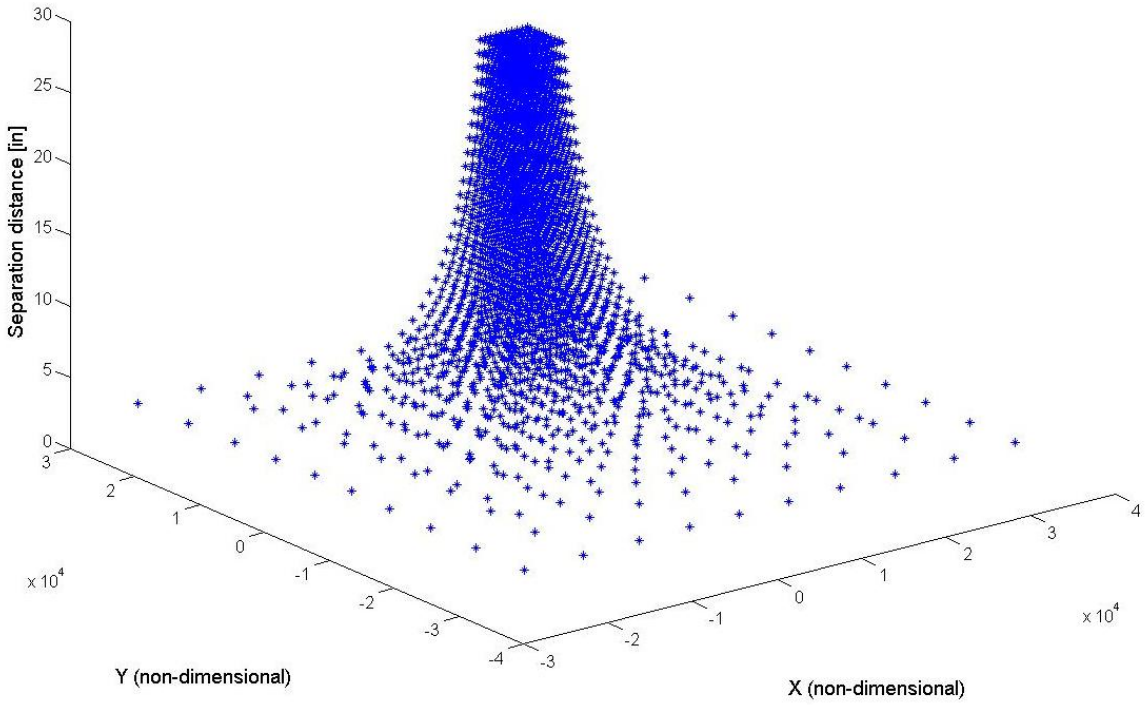

Figure 51 Simulated X and Y measurements from the NorthStar$_{TM}$ sensor spanning the range 3-30 inches.

Fitting the NorthStar$_{TM}$ mathematical model

After generating measurement data, they were fit using the NorthStar$_{TM}$ mathematical model and the GLSDC algorithm. The unknown parameters to be solved for are

$$\boldsymbol{x} = \begin{bmatrix} d_1 & d_2 & d_3 & p_1 & p_2 & p_3 & H \end{bmatrix}^T \tag{64}$$

and the measurement estimates are given as

$$\mathbf{f}(\boldsymbol{x}) = \begin{bmatrix} \hat{y}_x \\ \\ \hat{y}_y \end{bmatrix} = \begin{bmatrix} H\left[\dfrac{C_{11}(r_1 - d_1) + C_{12}(r_2 - d_2) + C_{13}(r_3 - d_3)}{C_{31}(r_1 - d_1) + C_{32}(r_2 - d_2) + C_{33}(r_3 - d_3)}\right] \\ \\ H\left[\dfrac{C_{21}(r_1 - d_1) + C_{22}(r_2 - d_2) + C_{23}(r_3 - d_3)}{C_{31}(r_1 - d_1) + C_{32}(r_2 - d_2) + C_{33}(r_3 - d_3)}\right] \end{bmatrix} \tag{65}$$

where the values for the *C* elements come from equation (55). The Jacobian matrix *G* is found by taking the partial derivatives of $\mathbf{f}(\boldsymbol{x})$ with respect to the each of the unknown parameters in the vector $\boldsymbol{x}$.

$$G = \left.\frac{\partial \mathbf{f}}{\partial \boldsymbol{x}}\right|_{\boldsymbol{x}_c} = \left[\begin{matrix} \dfrac{\partial \hat{y}_x}{\partial d_1} & \dfrac{\partial \hat{y}_x}{\partial d_2} & \dfrac{\partial \hat{y}_x}{\partial d_3} & \dfrac{\partial \hat{y}_x}{\partial p_1} & \dfrac{\partial \hat{y}_x}{\partial p_2} & \dfrac{\partial \hat{y}_x}{\partial p_3} & \dfrac{\partial \hat{y}_x}{\partial H} \\ \dfrac{\partial \hat{y}_y}{\partial d_1} & \dfrac{\partial \hat{y}_y}{\partial d_2} & \dfrac{\partial \hat{y}_y}{\partial d_3} & \dfrac{\partial \hat{y}_y}{\partial p_1} & \dfrac{\partial \hat{y}_y}{\partial p_2} & \dfrac{\partial \hat{y}_y}{\partial p_3} & \dfrac{\partial \hat{y}_y}{\partial H} \end{matrix}\right]_{\boldsymbol{x}_c} \tag{66}$$

For simplicity, the weighting matrix W is assumed to be an identity matrix.

From Figure 44 and Figure 48, it is apparent that for very small rotations, the unknown parameters d_3 and H are nearly parallel. When the parameters represent parallel dimensions, one of the parameters is unobservable and the Jacobian matrix becomes singular (or nearly singular for nearly parallel parameters). In order to make both parameters observable, the GLSDC can solve for the parameters using two different heights from the dataset. Many combinations of heights were run through the GLSDC algorithm to determine which combinations work the best. Four of the combinations are

shown in Table 3, with the true values arbitrarily chosen. The true value for the scale height, H, was determined using equation (5) knowing that at $\theta = 60°$, X_{inf} is 32,768.

As expected, solving for the parameters using two heights which are close to the sensor (three and five inches) yields a poor solution. This is due to the fact that the simple NorthStar$_{TM}$ mathematical model does not account for near-field errors which are significant at these close ranges. The solution when the beacons are far away (95 and 100 inches) is not significantly better than the solutions when the beacons are in the upper range of the CTA (i.e. the 20 and 25 inch case and 25 and 30 inch case). Interestingly, for the final three cases, the GLSDC algorithm solved for the parameter d_3 at a value far from the actual value. Representing the Z-direction offset between the $\mathcal{N}$-frame and the $\mathcal{O}$-frame, the solutions for d_3 given by the last three cases indicate the GLSDC algorithm thinks the NorthStar$_{TM}$ sensor is viewing the beacons from a virtual "eye" located three-quarters of an inch below the NorthStar$_{TM}$ sensor board. All of the other parameter solutions are within five percent of their true values, however. Plots of the simulated X/Y measurements and the X/Y estimates are shown in Figure 52-Figure 56. Notice that at three inches separation (Figure 52), the emulated data does not form a straight line grid due to near-field nonlinearities. Additionally, because of the near-field errors which are unaccounted for, the estimates are significantly different from the measurements.

Table 3 Comparison of NorthStar$_{TM}$ mathematical model fit using different height data.

Separation Distances [in]	Parameter	True value	Estimated Value	% Diff
3 and 5	d_1 [in]	0.6000	0.68314	13.9
	d_2 [in]	0.1000	0.05273	-47.3
	d_3 [in]	0.0620	0.45772	638.3
	p_1	0.0010	-0.00190	-289.7
	p_2	0.0020	-0.00292	-245.9
	p_3	0.0010	0.00112	12.3
	H	18919	15801	-16.5
20 and 25	d_1 [in]	0.6000	0.60732	1.2
	d_2 [in]	0.1000	0.09646	-3.5
	d_3 [in]	0.0620	-0.78588	-1367.6
	p_1	0.0010	0.00098	-2.1
	p_2	0.0020	0.00196	-2.0
	p_3	0.0010	0.00105	4.8
	H	18919	18824	-0.5
25 and 30	d_1 [in]	0.6000	0.60721	1.2
	d_2 [in]	0.1000	0.09648	-3.5
	d_3 [in]	0.0620	-0.79446	-1381.4
	p_1	0.0010	0.00098	-1.7
	p_2	0.0020	0.00197	-1.5
	p_3	0.0010	0.00104	4.0
	H	18919	18831	-0.5
95 and 100	d_1 [in]	0.6000	0.60372	0.6
	d_2 [in]	0.1000	0.09831	-1.7
	d_3 [in]	0.0620	-0.72859	-1275.1
	p_1	0.0010	0.00100	0.4
	p_2	0.0020	0.00201	0.4
	p_3	0.0010	0.00101	1.4
	H	18919	18807	-0.6

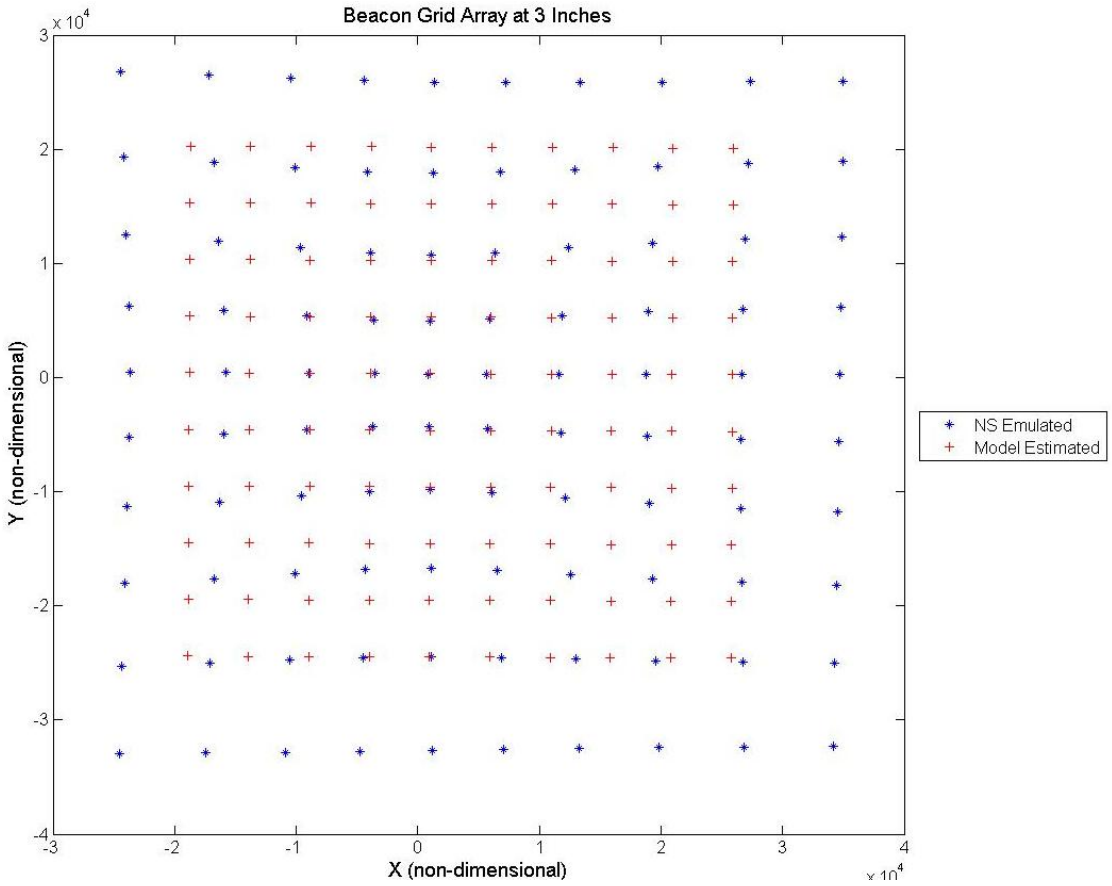

Figure 52 Plot of emulated NorthStar$_{TM}$ measurements and the NorthStar$_{TM}$ mathematical model estimates at three inches separation.

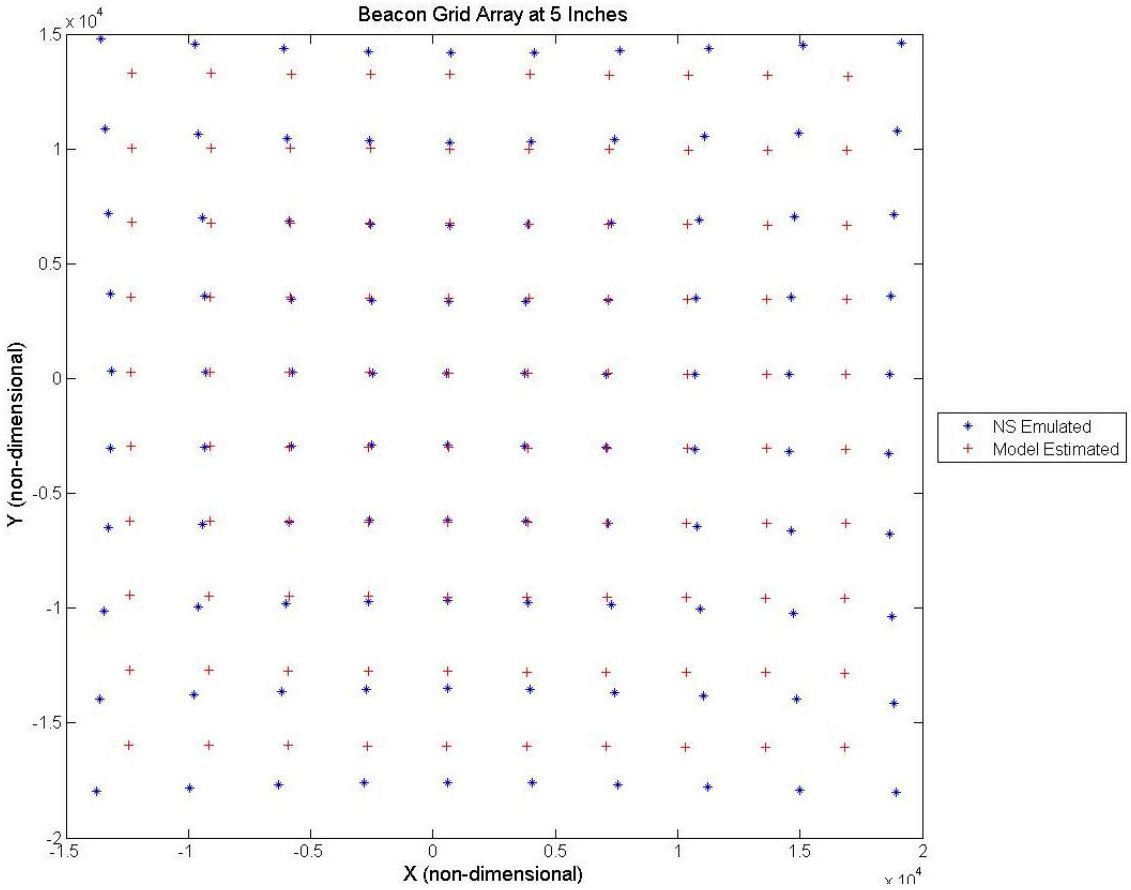

Figure 53 Plot of emulated NorthStar$_{TM}$ measurements and the NorthStar$_{TM}$ mathematical model estimates at five inches separation.

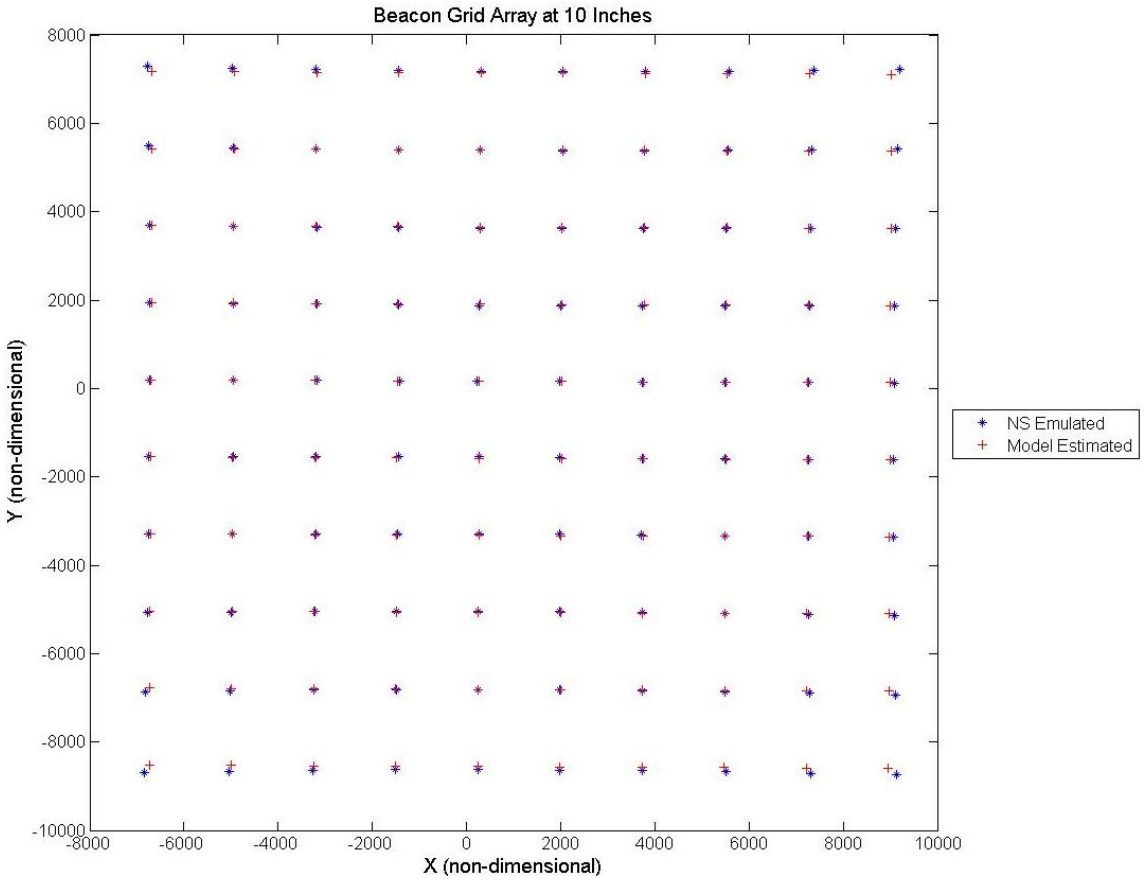

Figure 54 Plot of emulated NorthStar$_{TM}$ measurements and the NorthStar$_{TM}$ mathematical model estimates at ten inches separation.

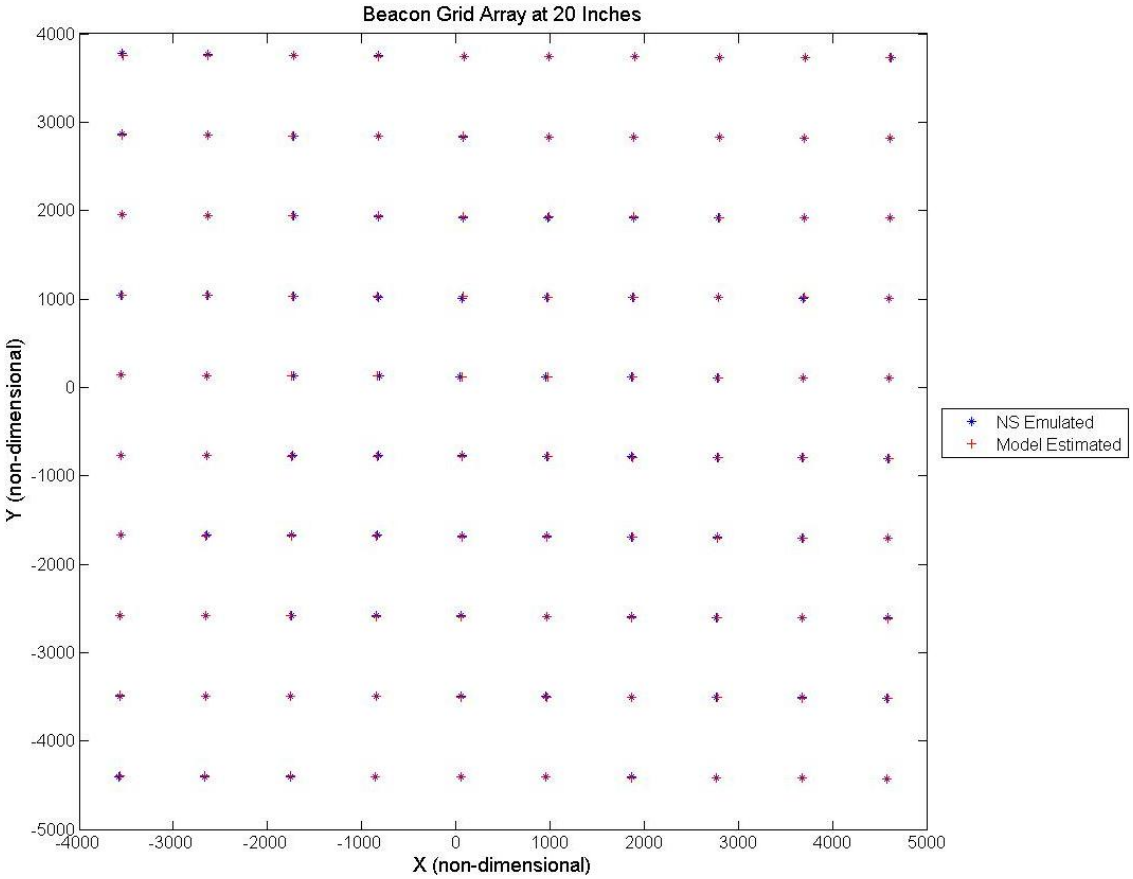

Figure 55 Plot of emulated NorthStar$_{TM}$ measurements and the NorthStar$_{TM}$ mathematical model estimates at twenty inches separation.

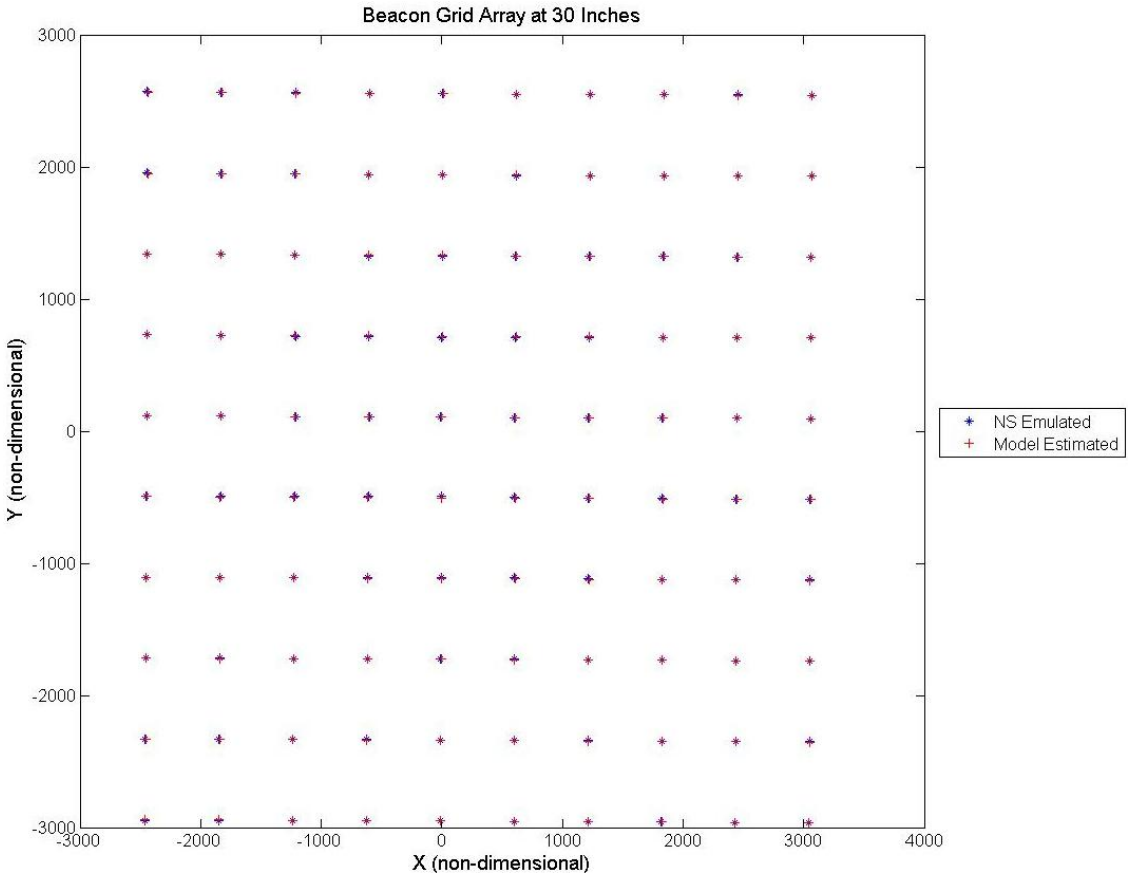

Figure 56 Plot of emulated NorthStar$_{TM}$ measurements and the NorthStar$_{TM}$ mathematical model estimates at thirty inches separation.

Notice that as the separation distance increases, the estimation more closely matches the emulated data. The near-field effects are less important the farther from the sensor the beacons are. To determine how the estimated X and Y values translate into errors in the angle ($\delta\theta$) of the vector from the NorthStar$_{TM}$ sensor head to the beacons, estimated vectors $\boldsymbol{b}_{est}$ were obtained by the transformation

$$\boldsymbol{b}_{est} = C^T \begin{bmatrix} X_{est} \\ Y_{est} \\ H_{est} \end{bmatrix} \tag{67}$$

The dot product between the true vectors to the beacons ($\boldsymbol{b_{inf}}$) and the estimated vectors ($\boldsymbol{b_{est}}$) was taken and the error in angle at each beacon at each separation distance was calculated. Additionally, using the three-dimensional equation for the uncertainty in the angle (equation (36)), the average uncertainty in the angle (θ) was computed at each separation distance. The standard deviation of the error in angle at each separation distance was calculated and is plotted with the average uncertainty in the angle (θ) due to the CTA in Figure 57.

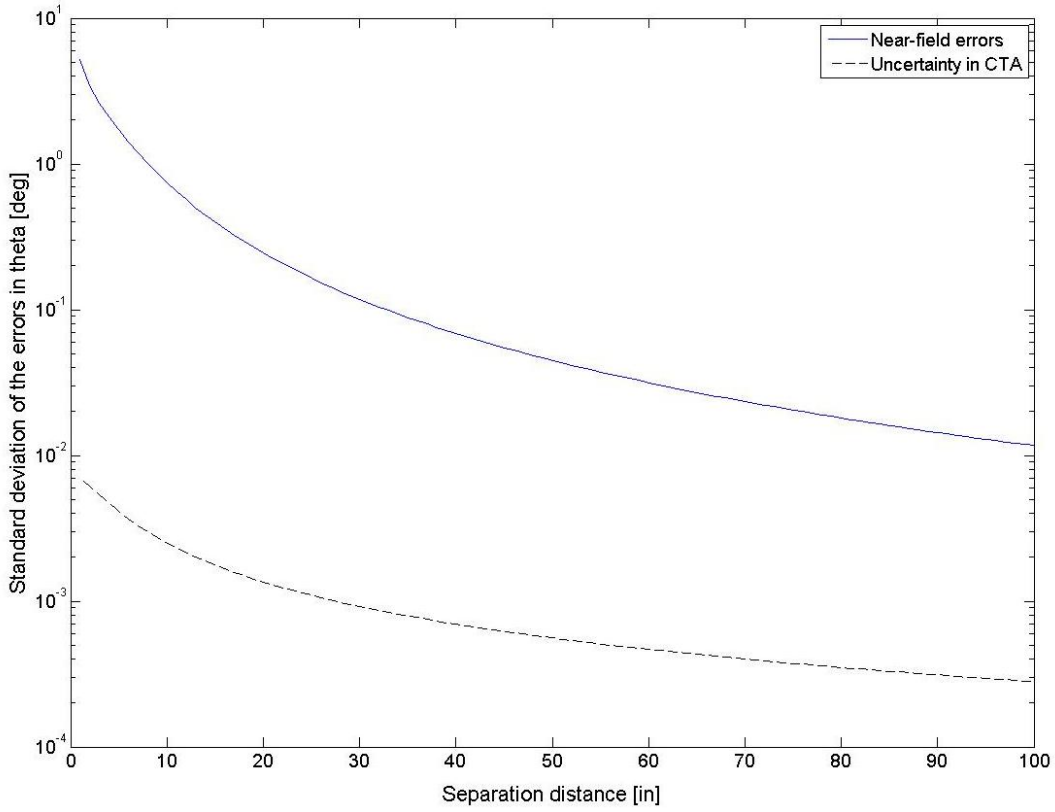

Figure 57 Standard deviation of the error in angle ($\delta\theta$) with respect to separation distance and uncertainty in the angle due to the CTA uncertainty.

The error in the angle at one inch has one standard deviation of just over five degrees, with the error falling off to approximately one-tenth of a degree standard deviation at thirty inches and on the order of one-hundredth of a degree standard deviation at one hundred inches. Additionally, the uncertainty in the CTA creates an error in the angle which is more than an order of magnitude smaller than the errors in the angle due to the near-field effects.

CHAPTER VI

CONCLUSIONS AND RECOMMENDATIONS

This thesis developed analytical models for proximity, intensity, and non-uniform light near-field errors arising from the geometry of the cosine-type pyramidal coarse sun sensor and determined expected error magnitudes due to these effects. While the magnitudes of these effects become significant as the sensor approaches the beacon(s), knowing what the effects are would allow engineers to account for these effects during a close-proximity relative navigation or docking maneuver. The analyses presented in this thesis do not find any show stoppers for utilizing a coarse sun sensor as the cornerstone of a 6-dof solution.

In order to characterize these near-field effects, an experimental test bed termed the Characterization Test Apparatus (CTA) was proposed, its design presented, and the design stage uncertainty analysis of the CTA performed. A candidate coarse sun sensor, the NorthStar$_{TM}$ sensor, was chosen based on availability, cost, and physical parameters (low-mass, low-power, small physical envelope). After developing a simple mathematical model for the NorthStar$_{TM}$ sensor, the model was used along with a GLSDC algorithm to estimate parameters which allowed the best fit between the mathematical model and the simulated NorthStar$_{TM}$ sensor output (accounting for all near-field effects). Calibrating the mathematical model using separation distances greater than twenty inches yielded the best results. Comparing the errors in the angle ($\delta\theta$) of the vector from the NorthStar$_{TM}$ sensor to the beacon due to the uncertainty in the

CTA to the errors in the angle due to the near-field effects, it appears the proposed CTA will provide sufficient resolution to characterize the errors due to the combined near-field effects.

NorthStar$_{TM}$ Sensor Data Collection Recommendations

Based on the results in Table 3, and due to the limitations on maximum separation distance in the CTA, it is recommended that the NorthStar$_{TM}$ model parameters be calibrated using separation distances in the vicinity of twenty to thirty inches. Differences in the parameter results for trial runs at those distances were not significantly different. By calibrating the model parameters at separation distances of twenty to thirty inches, the errors due to near-field effects at those distances will be calibrated into the model parameters as biases (i.e. the error curves will shift towards zero). However, near-field errors at thirty inches are significantly smaller than the near-field errors as the sensor approaches the beacons. Collecting experimental measurements and using them in place of the simulated measurements, a plot similar to Figure 57 should be obtained. The offset between the experimental data and the predicted curve can be determined, and the experimental data can be shifted by that offset in order to compare the experimental results with the near-field error analysis.

When developing a data collection scheme, thought has to be given not only to data allowing the resolution of near-field effects, but also collecting data useful for characterizing other effects not addressed in this thesis. Mention has been made about the expected noise levels of a coarse sun sensor, but how the noise levels change based on beacon intensity, beacon modulation frequency, and beacon position needs to be

explored. Additionally, qualitative experiments performed with the NorthStar$_{TM}$ sensor (not reported) indicate that there is a relationship between the NorthStar$_{TM}$ sensor measurement output and the frequency with which the beacon is modulated. The NorthStar$_{TM}$ sensor also has four different light sensitivity settings, so information on how the noise levels and measurement outputs vary based on light sensitivity settings need to be determined.

Keeping in mind all these questions with using the NorthStar$_{TM}$ sensor as part of a 6-dof solution which need to be addressed, the following data collection scheme is suggested for both the single beacon array configuration and the quad beacon array configuration:

1. Beginning at a two inch separation distance between the sensor and the beacon array, scan the grid at one inch increments all the way to the maximum separation distance (approximately thirty inches).
2. The CTA is capable of modulating the beacons at two separate power levels. At each separation distance, take multiple measurements (100-200) of each beacon location at various frequencies for each intensity level so the mean values and noise levels can be determined.
3. At each separation distance, repeat step two with each of the four different sensitivity settings.
4. Keep the ambient lighting conditions the same between experiments.
5. All desired data at each separation distance should be collected before increasing the separation distance. Doing so will reduce the number of times the CTA must

be handled, and it will ensure the physical geometry of the various experiments are as similar as possible.

Future Work

All of the components of the CTA are in house or being machined. The CTA must be assembled and an absolute uncertainty analysis performed on the actual hardware. Following the absolute uncertainty analysis, experimental data using a data collection scheme based off the suggestions presented herein must be obtained. Using the experimental data, the NorthStar$_{TM}$ sensor model can be calibrated and near-field effects resolved.

With a calibrated sensor model and bounds on the uncertainties in the errors in angle ($\delta\theta$), a real-time 6-dof solution (using a GLSDC or other algorithm) can be programmed onto the NorthStar$_{TM}$ sensor board microprocessor and a demonstration of the sensor can be performed.

Additionally, a higher fidelity mathematical model can be derived based on the simple model presented herein which includes additional terms which capture the near-field nonlinear effects on the sensor measurements. Work also needs to be performed to determine a suitable weighting matrix.

REFERENCES

[1] Sadin, S. R., and Davis, R. W., "The SmallSat Revolution….Back to the Future?," *Acta Astronautica*, Vol. 34, 1994, pp. 109-122.

[2] Rendleman, J. D., "Why SmallSats?," *AIAA Space 2009 Conference & Exposition*, AIAA 2009-6416, Pasadena, CA, 14-17 September 2009.

[3] Woffinden, D. C., and Geller, D. K., "Navigating the Road to Autonomous Orbital Rendezvous," *Journal of Spacecraft and Rockets*, Vol. 44, No. 4, July-August 2007, pp. 898-909.

[4] Mokuno, M., Kawano, I., and Suzuki, T., "In-Orbit Demonstration of Rendezvous Laser Radar for Unmanned Autonomous Rendezvous and Docking," *IEEE Transactions on Aerospace and Electronic Systems*, Vol. 40, No. 2, April 2004, pp. 617-626.

[5] Swartwout, M., Kitts, C., Twiggs, R., Kenny, T., Smith, B. R., Lu, R., Stattenfield, K., and Pranajaya, F., "Mission Results for Saphire, A Student-Built Satellite," *Acta Astronautica*, Vol. 62, 2008, pp. 521-538.

[6] Kornfeld, R. P., Bunker, G. C. C., Essmiller, J. C., Hadaegh, F. Y., Liebe, C. C., Padgett, C. W., Wong, E. C., "New Millenium ST6 Autonmous Rendezvous Experiment (ARX)," *IEEE Aerospace Conference*, 1114, Big Sky, MT, 8-15 March 2003.

[7] Mitchell, J. D., Cryan, S. P., Strack, D., Brewster, L. L., Williamson, M. J., Howard, R. T., Johnston, A. S., "Automated Rendezvous and Docking Sensor

Testing at the Flight Robotics Laboratory," *IEEE Aerospace Conference*, 1055, Big Sky, MT, 3-10 March 2007.

[8] Holt, G., Stewart, S., Mauldin, J., Campbell, T., Eckhoff, P., Elmasri, H., Evans, B., Garg, M., Greenbaum, J., Linford, M., Poole, M., Lightsey, E. G., Raja, L. L., and Ebinuma, T., "Relative Navigation, Microdischarge Plasma Thruster, and Distributed Communications," *AIAA/USU Conference on Small Satellites*, SSC03-XI-04, Logan, UT, 11-14 August 2003.

[9] Wertz, J. R. (ed.), *Spacecraft Attitude Determination and Control*, Astrophysics and Space Science Library, D. Reidel, Netherlands, 1978, pp. 155-166.

[10] Vishay Semiconductors, "VSML3710: High Power Infrared Emitting Diode, 940 nm RoHS Compliant, Released for Lead (Pb)-free Solder Process," *Vishay*, 81300, Rev. 1.2, 25 Jan 2007.

[11] Evolution Robotics, Inc., "NorthStar$_{TM}$ Detector Kit User's Guide," *Evolution Robotics*, B-M-0059, Rev. 1.0, URL: http://www.evolution.com/products/, [retrieved September 2009].

[12] Doebbler, J., Davis, J. J., Valasek, J., and Junkins, J. L., "Characterization and Implementation of a Vision-Based 6-DOF Localization System," *AIAA Guidance, Navigation, and Control Conference*, AIAA 2008-7321, Honolulu, HI, 18-21 August 2008.

[13] Freescale Semiconductor, "Digital Signal Controllers 56F8013," *Freescale Semiconductor*, URL:

http://www.freescale.com/files/dsp/doc/fact_sheet/56F8013DSCFS.pdf, [retrieved June 2010].

[14] Evolution Robotics, "NorthStar$_{TM}$ Localization Detector Product Data Specification," *Evolution Robotics*, 02-014-0045, Rev. 01, URL: http://www.evolution.com/products/, [retrieved September 2009].

[15] Crassidis, J. L., and Junkins, J. L., *Optimal Estimation of Dynamic Systems*, Applied Mathematics and Nonlinear Science Series, Chapman & Hall/CRC, Boca Raton, 2004, pp. 24-29, 194.

[16] Schaub, H., and Junkins, J. L., *Analytical Mechanics of Space Systems*, AIAA Education Series, AIAA, Virginia, 2003, pp. 107-111.

APPENDIX

LOCATION OF AVERAGE VOLTAGE ON PHOTOVOLTAIC CELLS

In order to justify treating the PV cells as points instead of plates in the near-field analyses presented in this thesis, it is required to determine the magnitude of the error incorporated into the results due to this assumption. The analyses all assume that there is a point (l_{eff}) on each PV cell from which a vector ($\boldsymbol{r}_{\boldsymbol{eff}}$) can be drawn to the light source which, when dotted with the unit normal vector, will generate the same voltage as an actual PV cell (which is a plate) would generate. If the point (l_{eff}) does not move as the beacon approaches the PV cell, then assuming treating the PV cells as points rather than plates is a good assumption. However, if the point (l_{eff}) moves significantly as the beacon approaches the PV cell, then the PV cells need to be modeled as plates and the uncertainty in the position of (l_{eff}) must be accounted for.

Assume a PV cell of length L oriented as shown in Figure 58. A beacon is located at a position (x,y). The goal of this analysis is to find the point l_{eff} such that the effective output signal matches the output of the PV cell when modeled by a plate.

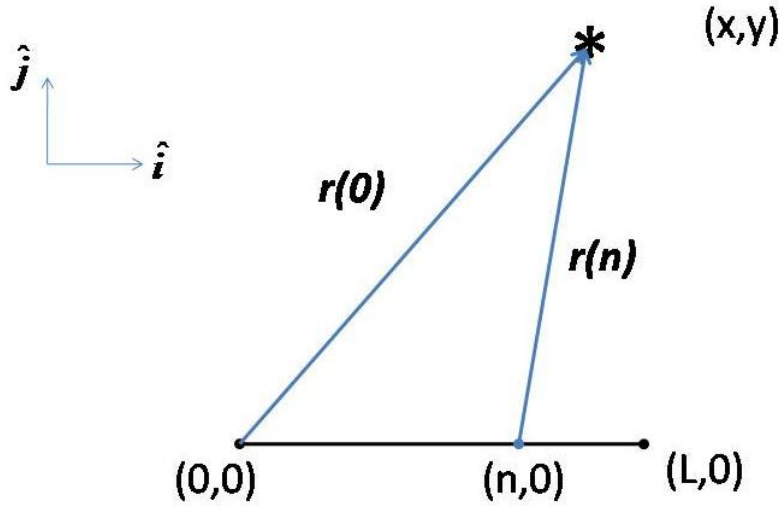

Figure 58 PV cell to beacon geometry.

The effective signal output can be modeled by

$$X_{eff} = I_{eff} V_{eff} \tag{68}$$

where

$$I_{eff} = \frac{1}{L}\int_0^L I(n)\,dn$$

$$V_{eff} = \hat{\boldsymbol{r}}_{\boldsymbol{eff}} \bullet \hat{\boldsymbol{j}} \tag{69}$$

$$\hat{\boldsymbol{r}}_{\boldsymbol{eff}} = \frac{1}{\sqrt{\left(x - l_{eff}\right)^2 + y^2}} \begin{bmatrix} x - l_{eff} \\ y \end{bmatrix}$$

The output signal assuming the PV cell is a plate is the integral of the intensity times the voltage at each point *n* along the plate divided by the length of the plate (*L*).

$$X = \frac{1}{L}\int_0^L I(n)V(n)\,dn$$

$$V(n) = \hat{\boldsymbol{r}}(n)\bullet\hat{\boldsymbol{j}} \tag{70}$$

$$\hat{\boldsymbol{r}}(n) = \frac{1}{\sqrt{(x-n)^2 + y^2}}\begin{bmatrix} x-n \\ y \end{bmatrix}$$

Since $\hat{\boldsymbol{j}} = \begin{bmatrix} 0 & 1 \end{bmatrix}^T$, equations (68) and (69) can be solved, resulting in the equation

$$X_{eff} = \frac{1}{yL}\left(\tan^{-1}\left(\frac{x}{y}\right) + \tan^{-1}\left(\frac{L-x}{y}\right)\right)\frac{y}{\sqrt{(x-l_{eff})^2 + y^2}} \tag{71}$$

and equations (70) can be solved to yield

$$X = \frac{1}{yL}\left(\frac{L-x}{\left((L-x)^2 + y^2\right)^{1/2}} + \frac{x}{\left(x^2 + y^2\right)^{1/2}}\right) \tag{72}$$

Equating (71) and (72) and solving for l_{eff} results in a quadratic with two separate solutions.

$$l_{eff} = \frac{2x \pm \sqrt{(-2x)^2 - 4(1)(B)}}{2}$$

$$B = x^2 + y^2 - A^2 \tag{73}$$

$$A = \frac{y\left(\tan^{-1}\left(\frac{x}{y}\right) + \tan^{-1}\left(\frac{L-x}{y}\right)\right)}{\left(\frac{L-x}{\left((L-x)^2 + y^2\right)^{1/2}} + \frac{x}{\left(x^2 + y^2\right)^{1/2}}\right)}$$

Utilizing equations (73), a simulation was constructed to determine the values of l_{eff} as a beacon approaches the PV cell. Since the intensity changes according to an inverse square law, the location of l_{eff} will be most affected by beacons which are at a greater angle with respect to the PV cell boresight (because the difference in the magnitudes of the vectors from one end of the cell to the other increases as angle increases). A beacon was placed 60° off of the PV cell boresight and moved toward the PV cell, and both solutions to l_{eff} were calculated.

The length of the PV cell is unknown, so instead of substituting the cell length L in directly, a ratio between the length of the PV cell and the diameter of the sensor was used. The sensor diameter was the same as assumed in the other analyses in Chapter II.

$$L^* = \frac{L}{Sensor\ Diameter} \tag{74}$$

After calculating both l_{eff} solutions, the results were divided by L^* and plotted against the beacon distance from the PV cell (in numbers of sensor diameters). Since l_{eff} must be contained on the plate, dividing the l_{eff} by L^* should never yield an answer greater than one. The correct solution to (73) can be determined by inspection of the plots. The result of the simulation for differing values of L^* are shown in Figure 59. Note that only the correct solution to (73) is shown.

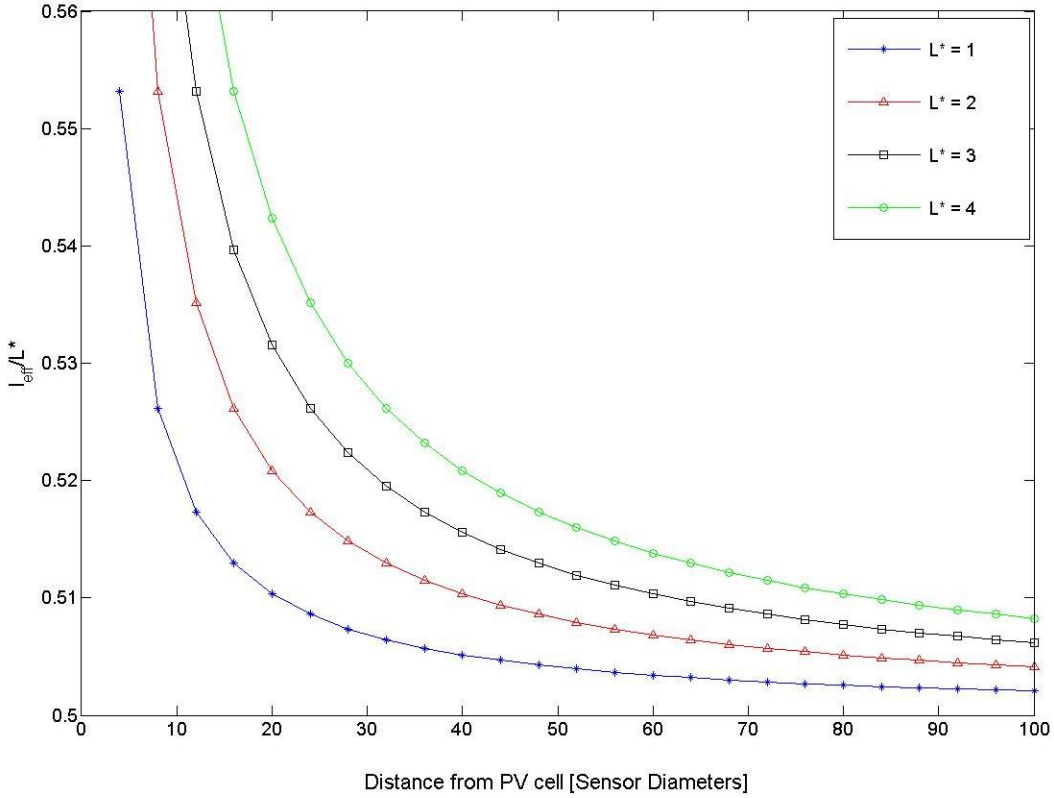

Figure 59 Position of l_{eff} along the PV cell with respect to beacon distance from PV cell.

Notice l_{eff} is located approximately in the middle of the PV cell, and that its location remains fairly constant. As the beacon approaches the PV cell, the location of l_{eff} changes slightly, but it has only changed by approximately five percent when the beacon is at four sensor diameters (for the $L^* = 1$ case). The NorthStar$_{TM}$ sensor, for comparison, has an L^* ratio of approximately one. This analysis indicates that for an analysis which is attempting to obtain an order of magnitude estimate of the near-field effects (as is the case for this thesis), representing the PV cells as points located at the middle of the PV cells is a good approximation.

VITA

Name:	Devin Aldin Stancliffe
Address:	701 HR Bright Building MS 3141 College Station, TX 77843
Email Address:	dastancliffe@gmail.com
Education:	B.S., Zoology – Human Biology Emphasis, Brigham Young University, 2003
	B.S., Aerospace Engineering, Texas A&M University, 2008
	M.S., Aerospace Engineering, Texas A&M Univertisy, 2010